

**Fluorescence Correlation Spectroscopy of autofluorescent
proteins and its applications in live cell membranes**

**Dissertation
zur Erlangung des Grades
des Doktors der Naturwissenschaften
der Naturwissenschaftlich-Technischen Fakultät III
Chemie, Pharmazie, Bio- und Werkstoffwissenschaften
der Universität des Saarlandes**

**von
Seena Koyadan Veetil**

**Saarbrücken
2009**

Date of PhD colloquium: 29.05.2009

Dekan: Prof. Dr.-Ing. S. Diebels

Chairman: Prof. Dr. Gerhard Wenz

Reviewers: Prof. jr. Dr. Gregor Jung
Prof. Dr. Ingolf Bernhardt

Scientific coworker: Dr. Markus Martin

*Dedicated to
My father and mother*

Summary

Fluorescence correlation spectroscopy (FCS) is used for investigating the kinetic processes and molecular interactions by means of the statistical analysis of fluorescence fluctuations. These fluorescence fluctuations which arise from the small confocal volume are due to diffusion, rotation, intersystem crossing, conformational changes or other random effects of the fluorescent molecules under study. Therefore the fluorescent intensity from these fluctuations contains photophysical information on the nature of molecules. The aim of the work described in this thesis is to study the applications of FCS. The thesis is divided into 6 chapters. The theory, experimental setup and applications of FCS are outlined in chapter 1. A method of determining the photostability of autofluorescent proteins by Stern-Volmer plot like analysis is described in chapter 2. Photostability of green (GFP) and yellow fluorescent proteins (YFP) with fluorinated chromophores are analysed by intensity dependent FCS measurements. Such a photostability analysis is continued in chapter 3 with F64L containing GFP mutants. In addition, this chapter also explains a thermal relaxation rate constant of EGFP which is accompanied by the transition between the bright state and the dark state. By wavelength dependent FCS measurements, the protonated state of the Thr203 and Glu222 containing GFP mutants are demonstrated in chapter 4. Chapter 5 describes the effect of membrane potential on the lateral diffusion of the $K^+(Na^+)/H^+$ exchanger on the membrane of live red blood cell (RBC). Characterization of PLGA (polylactic-co-glycolic acid) nanoparticles tagged with oligonucleotides which are potential drug carriers in pharmaceutical applications are studied in chapter 6.

Zusammenfassung

Die Fluoreszenz-Korrelations-Spektroskopie (FCS) wird benutzt zur Untersuchung kinetischer Prozesse und molekularer Interaktionen auf der Basis einer statistischen Analyse von Fluoreszenz-Fluktuationen. Diese Fluoreszenz-Fluktuationen, die aus einem kleinen konfokalen Volumen stammen, rühren von Diffusion, Rotation, Intersystem-Übergängen, Konformationsänderungen oder anderen zufälligen Effekten der untersuchten Fluoreszenzmoleküle her. Aus diesem Grund enthält die Fluoreszenz-Intensität dieser Fluktuationen photophysikalische Informationen über die Natur der Moleküle. Es ist das Ziel der in dieser Thesis beschriebenen Arbeit die Anwendungen von FCS zu untersuchen. Die Thesis ist unterteilt in 6 Kapitel. Die Theorie, experimenteller Aufbau und Anwendungen von FCS werden in Kapitel 1 vorgestellt. Eine Methode der Bestimmung der Photostabilität autofluoreszierender Proteine mit Hilfe einer Stern-Volmer-Plot-artigen Analyse ist in Kapitel 2 beschrieben. Die Photostabilität von grün und gelb fluoreszierenden Proteinen (GFP und YFP) mit fluorierten Chromophoren wird mit Intensitäts-abhängigen FCS-Messungen untersucht. Eine derartige Photostabilitäts-Analyse wird in Kapitel 3 mit F64L enthaltenden GFP-Mutanten fortgeführt. Dieses Kapitel erklärt außerdem eine Ratenkonstante der thermalen Relaxation von EGFP; diese Relaxation wird begleitet vom Übergang zwischen Hell- und Dunkelzustand. Der protonierte Zustand der Thr203 und Glu222-enthaltenden GFP-Mutanten wird in Kapitel 4 durch wellenlängen-abhängige FCS-Messungen demonstriert. Kapitel 5 beschreibt den Effekt des Membranpotentials auf die laterale Diffusion des $K^+(Na^+)/H^+$ -Austauschers auf der Membran von lebenden roten Blutzellen. Die Charakterisierung von mit Oligonukleotiden getaggten PLGA-Nanopartikeln (polylactic-co-glycolic acid), die potentielle Drug-Carrier in pharmazeutischen Anwendungen darstellen, wird in Kapitel 6 untersucht.

Acknowledgements

I am very thankful to my doctor-father Prof. Dr. Gregor Jung for the opportunity to work under his supervision in a challenging research field. I sincerely thank him for the constant support, encouragement, fruitful discussions, teaching lessons and constructive criticisms.

I would like to thank for the discussions and the collaborative work with Prof. Dr. Ingolf Bernhardt. I am grateful to him for reading some chapters of my thesis and giving valuable comments. I acknowledge the collaborative work with Dr. Marc Schneider.

I am highly grateful to Aravind Pasula and Dr. Noha Nafee for preparing samples during the collaborative work.

My thanks go to the coworkers Alex, Babette, Silke, Benjamin, Stephan, Nicole and Dagmar for always having time for creating an enjoyable and stimulating atmosphere.

I express my sincere thanks to Prof. Rolf Hempelmann and his coworkers for their support.

My MSc mentor Prof. Dr. V. K. Sasidharan (late) acknowledged here with great fondness and sincerity.

I am very much indebted to my parents Gangadharan and Pathmavathi, my brother and husband for their love, tolerance, support and guidance.

Finally, I would like to thank the great 'Shakthi' for all the successful and happiest moments in my life.

Seena Koyadan Veetil

Table of Contents

Summary	iii
Zusammenfassung	iv
Acknowledgments	v
Table of Contents	vi
Chapter 1: General Introduction	1
1.1 Historical account	2
1.2 FCS theory	4
1.2.1 Solutions for autocorrelation function	6
1.2.1.1 Autocorrelation function for single species	6
1.2.1.2 Autocorrelation function for multiple species	8
1.2.1.3 Autocorrelation function for triplet contribution	8
1.2.1.3.1 Jablonski diagram	9
1.2.1.4 Multiple component diffusion	11
1.2.2 Fitting of FCS data	12
1.3 Experimental considerations	13
1.3.1 Materials and methods	13
1.3.1.1 FCS set up	13
1.3.1.2 Samples	15
1.3.1.3 Fluorescence excitation and emission spectra	16
1.3.1.4 Time-Correlated Single-Photon Counting (TCSPC)	16
1.3.2 Practical Considerations	16
1.3.3 Confocal volume	18
1.4 Diffusion	19
1.5 Fluorescent probes	22
1.5.1 Fluorescent dyes	22
1.5.2 Green fluorescent proteins	23
1.5.2.1 Enhanced green fluorescent protein	24
1.5.2.2 Enhanced yellow fluorescent protein	25
1.5.2.3 Folding of GFP	25
1.5.3 Photobleaching	26
1.5.4 Blinking of GFP molecules	27
1.6 Experimental studies with FCS	29
1.6.1 FCS and binding assay	29
1.6.2 FCS in cells	30
1.6.3 Aggregation measurements	31
1.6.4 Conformational fluctuations of DNA molecule	32
1.6.5 Pharmaceutical applications	33
1.7 Variations of FCS	34

Chapter 2: Photostability of green and yellow fluorescent proteins with fluorinated chromophores, investigated by fluorescence correlation spectroscopy 35

2.1 Background.....	36
2.2 Materials and Methods.....	37
2.2.1 Analysis of FCS data	37
2.2.2 Analysis of the photostability	38
2.3 Results and Discussion	40
2.3.1 Spectral characteristics.....	40
2.3.2 Photostability determination	43
2.3.3 Comparison to previously determined values.....	46
2.4 Conclusion	47

Chapter 3: Comparative analysis of F64L containing GFP mutants and its influence on photostability by fluorescence correlation spectroscopy..... 48

3.1 Introduction.....	49
3.1.2 Changes in Venus	49
3.2 Analysis of FCS data	51
3.3 Results.....	53
3.3.1 Thermal relaxation rate constant.....	56
3.4 Discussion	59
3.5 Conclusion	62

Chapter 4: Wavelength dependent FCS measurements of Tyr203 and Gln222 containing GFP mutants..... 63

4.1 Introduction.....	64
4.1.2 Characteristics of the amino acid at position Thr203 and Glu222.....	65
4.3 Experimental setup and analysis method.....	66
4.4 Results and discussion	67

Chapter 5: Effect of membrane potential on the diffusion time of $K^+(Na^+)/H^+$ exchanger in red blood cell membrane using fluorescence correlation spectroscopy..... 77

5.1 Introduction.....	78
5.1.1 Red blood cell membrane transport and the $K^+(Na^+)/H^+$ exchanger	78
5.1.2 The red blood cell membrane potential profile.....	80
5.2 Experimental considerations.....	81
5.2.1 Data analysis	82
5.2.2 Preparation of red blood cells for FCS measurements.....	83

5.3 Results and discussion	84
5.3.1 Autocorrelation curve for the experiment.....	85
5.3.2 Diffusion of the K ⁺ (Na ⁺)/H ⁺ exchanger labeled with BODIPY FL amiloride	86
5.3.4 Diffusion of β-BODIPY (R) FL-C12-HPC labeled lipids	89
Chapter 6: Characterization of nanoparticles tagged with oligonucleotides using fluorescence correlation spectroscopy.....	91
6.1 Introduction.....	92
6.2 Materials and methods	93
6.2.1 Preparation and purification of nanoparticles	93
6.2.2 Preparation of Fluoresceinamin (FA) labeled PLGA nanoparticles	93
6.2.3 Formation of nanoplexes.....	94
6.2.4 Fluorescence correlation spectroscopy with nanoparticles	94
6.3 Results and Discussion	94
Chapter 7: Appendices	99
References.....	101
List of figures.....	118
List of tables.....	120
Curriculum vitae	121

Chapter 1
General Introduction

1.1 Historical account

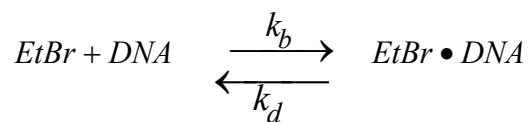
In the beginning of 20th century, the concept of fluctuation spectroscopy had been introduced. Svedberg and Inouye (1911) reported the studies on fluctuations of small gold colloidal particles in a fixed volume of the microscope using light scattering. In order to avoid the cancellation of the number of fluctuations in a dynamic system containing large number of molecules and to get the significant parameters, they introduced a small slit in the detection path thereby limiting the size of the observation volume (Svedberg and Inouye, 1911). Using the theoretical models (von Smoluchowski, 1914), the experimental data obtained were analysed. In this analysis, Smoluchowski used the concentration autocorrelation function:

$$G_c(\tau) \equiv \langle C(t)C(t+\tau) \rangle = \langle \delta C(t)\delta C(t+\tau) \rangle + \langle C \rangle^2 \quad (1.1)$$

Where, the angular bracket denotes the time average, $\delta C(t)$ is the deviation in particle number from the average particle number at a time t and τ is the time lag.

Different techniques have been developed using the concepts of number fluctuations. For example, quasi-elastic light scattering or photon correlation spectroscopy exploits the light scattering intensity from the particles of interest (Schaefer, 1973; Berne and Pecora, 1975) and the electrical conductance of a solution that reflects the number and charges of particles contained in the solution (Feher and Weissman, 1973). Fluctuation analysis of electrical currents from the membranes known as voltage clamp (Hodgkin and Katz, 1949) has been extensively used in the field of neurophysiology and it is later developed as patch clamp technique (Neher and Sakmann, 1976).

In the early nineteen seventies fluorescence correlation spectroscopy (FCS) was introduced (Magde et al., 1972) for monitoring the binding reaction between ethidium bromide and double stranded DNA. Ethidium bromide's (EtBr) fluorescence quantum yield increases by a factor of 20 upon binding with DNA bases.



Magde uses the above equilibrium for monitoring the fluorescence fluctuations of the dye. Two sources of fluorescence fluctuations are associated with this experiment, one is the diffusion of molecules in and out of the sampling volume and the other is chemical fluctuations associated with the binding and debinding of EtBr. The FCS autocorrelation function is a convolution of diffusion and relaxation terms. The relaxation rate R that is characteristic of the binding and debinding is linearly dependent on the EtBr concentration:

$$R = k_b([EtBr] + [DNA]) + k_d \approx k_b[EtBr] + k_d \quad (1.2)$$

Measuring this dependence gave $k_b = 1.5 \times 10^7 M^{-1} s^{-1}$ and $k_d = 27 s^{-1}$. This experiment of Magde *et al* successfully revealed ubiquitous fluctuations around equilibrium in a reactive system with sufficient precision to identify and measure chemical reaction kinetics as well as diffusion and to demonstrate the coupling between them. The foundations of FCS were given by series of works in 1970s. (Magde et al., 1972; Magde et al., 1974; Elson and Magde, 1974; Ehrenberg and Rigler, 1974). However, the early experiments suffered from the poor signal-to-noise ratios (SNR) due to the high background intensities caused by the Raman scattering of water and Rayleigh scattering of laser light. The situation was changed dramatically by the integration of confocal detection optics thereby decreasing the observation volume to subfemtoliter volume elements that significantly reduced the background emission (Qian and Elson, 1991; Rigler et al., 1993). In combination with confocal epi-illumination, highly sensitive avalanche photodiodes (APD) for fluorescence detection, improved correlators, high-quality objectives and very selective bandpass filters to separate the fluorescence from the background greatly increased the sensitivity of FCS and made it possible to improve

signal-to-noise ratios (SNR) in FCS measurements by several orders of magnitude (Eigen and Rigler, 1994; Rigler, 1995; Rigler and Widengren 1992; Rigler et al., 1993).

1.2 FCS theory

Fluorescence correlation spectroscopy is a technique which is used for investigating the kinetic processes and molecular interactions by statistical analysis of fluorescence fluctuations. These fluorescence fluctuations arise from the small confocal volume are due to diffusion, rotation, intersystem crossing, conformational changes or other random effects of the fluorophores. Therefore, the fluorescent intensity from these fluctuations contains sufficient information on the nature of molecules. For obtaining information about the molecular processes, these fluctuations can be analysed in terms of fluorescence intensity autocorrelation function (ACF) (Elson and Magde, 1974; Thompson, 1991).

The fluorescence intensity autocorrelation function $G(\tau)$ can be expressed by using the fluorescent light intensity fluctuations $\delta F(t)$ is as follows:

$$G(\tau) = \frac{\langle F(t) \cdot F(t + \tau) \rangle}{\langle F(t) \rangle^2} \quad (1.3)$$

The brackets $\langle \rangle$ indicate the time average over the fluorescence signal, t is the time at which the fluorescent intensity is recorded and τ is the correlation time. The above product is integrated and normalized (Eigen and Rigler, 1994; Schwille et al., 1999b)

$$\begin{aligned} G(\tau) &= \frac{\langle [\langle F(t) \rangle + \delta F(t)] \cdot [\langle F(t) \rangle + \delta F(t + \tau)] \rangle}{\langle F(t) \rangle^2} \\ &= \frac{\langle F(t) \rangle^2 + \langle \delta F(t) \cdot \delta F(t + \tau) \rangle}{\langle F(t)^2 \rangle} \end{aligned}$$

$$= 1 + \frac{\langle \delta F(t) \cdot \delta F(t + \tau) \rangle}{\langle F(t) \rangle^2} \quad (1.4)$$

where $\delta F(t) = F(t) - \langle F(t) \rangle$, because $\delta F(t)$ gives the corresponding fluorescent fluctuations in the fluorescent signal $F(t)$ around its mean value $\langle F(t) \rangle$. Also $\langle \delta F(t) \cdot \langle F(t) \rangle \rangle = \langle \langle F(t) \rangle \cdot \delta F(t) \rangle = 0$, since $\langle \delta F(t) \rangle = 0$.

1.2.1 Solutions for autocorrelation function

Models are required for extracting the information encoded in the shape of autocorrelation function. In order to obtain quantities such as diffusion coefficient, concentration, reaction rate constant, one has to fit the measured autocorrelation function by theoretical correlation function that is based on a model. This model should contain these quantities as free parameters. Theories of autocorrelation have been reviewed in detail (Eigen and Rigler, 1994; Maiti et al., 1997; Aragon and Pecora, 1976; Thompson, 1991). The functional form of autocorrelation depends on a factor called point spread function (PSF). PSF describes the spatial intensity profile seen by the detector and it depends on the microscope optics and the excitation light source. Three different PSFs have been widely used; (1) two-dimensional Gaussian PSF, (2) three-dimensional Gaussian PSF and (3) Gaussian-Lorentzian PSF. Two-dimensional Gaussian PSF describes the radially symmetric Gaussian intensity profile and the intensity distribution is in a plane perpendicular to the optical axis. Basically it is used to describe the process on surfaces like membranes. Three-dimensional Gaussian PSF also has an intensity profile in the radial direction and it gives the intensity distribution in the third dimension along the optical axis. This approximates the contribution of light from out-of-focal planes in a confocal detection arrangement. Gaussian-Lorentzian PSF is used to describe two-photon FCS. Lorentzian function gives the intensity profile along the optical axis in the absence of a confocal pinhole in front of the detector. A focused laser beam also exhibits such an intensity profile.

1.2.1.1 Autocorrelation function for single species

In the case of a single diffusing species, in the absence of chemical kinetics, fluorescent fluctuations in the open observation volume are caused by the diffusion of molecules in this volume. Autocorrelation function $G(\tau)$ for single fluorescent species with diffusion coefficient D and molar concentration c with Gaussian profile is (Rigler et al., 1993):

$$G(\tau) = 1 + \frac{1}{c \cdot V_{eff}} \frac{1}{\left(1 + \frac{4D\tau}{\omega_0^2}\right)} \frac{1}{\sqrt{1 + \frac{4D\tau}{z_0^2}}} \quad (1.5)$$

where V_{eff} is the effective observation volume that depends on the geometry of the focus for excitation and emission. ω_0 and z_0 are the half-widths of the focus in x-y plane and in the z direction, respectively. These three parameters can be measured independently by calibration with a solution of fluorophore having known concentration and diffusion coefficient. Putting average particle number $N = c \cdot V_{eff}$, the effective diffusion time $\tau_{diff} = \omega_0^2 / 4D$ and the structure factor $k = z_0 / \omega_0$, the above equation acquires the form:

$$G(\tau) = 1 + \frac{1}{N} \frac{1}{\left(1 + \frac{\tau}{\tau_{diff}}\right)} \frac{1}{\sqrt{1 + \frac{\tau}{k^2 \tau_{diff}}}} \quad (1.6)$$

The diffusion coefficient D is related to the size of the fluorescent molecules via the Stokes-Einstein equation:

$$D = \frac{kT}{6\pi\eta R} \quad (1.7)$$

In this equation k is the Boltzmann constant, T is the absolute temperature, η is the solvent viscosity and R is the hydrodynamic radius of a compact sphere in a viscous medium. The molecular mass M of a globular molecule can be estimated from FCS experiments:

$$D \propto \frac{kT}{6\pi\eta} \frac{1}{\sqrt[3]{M}} \quad (1.8)$$

The relation between R and M of the particles is: $M = 4\pi R^3 N_A \rho / 3$, where N_A and ρ are Avogadro's number and mean density of the molecule.

The FCS autocorrelation function $G(\tau)$ is inversely proportional to the number of fluorescent particles in the focal volume and their concentration. In the limit $\tau \rightarrow 0$, the autocorrelation function becomes $G(\tau \rightarrow 0) = 1/N = 1/c \cdot V_{eff}$. At low concentrations these deviations are due to the background which is caused by incomplete suppression of the excitation light, detector dark counts and background fluorescence. When the number of molecules in the observation volume increases, the relative effect of a single molecule on the total fluorescence signal decreases also the normalized autocorrelation amplitude decreases. Therefore the number of fluorescent molecules is kept small in the observation volume ($N \sim 1-10$) such that a correlation with significant amplitude is detected in a volume in the order of femtoliter and fluorophore concentration is in the nanomolar range.

For autocorrelation function for two-dimensional diffusion in the x-y plane, we have:

$$G(\tau) = 1 + \frac{1}{N} \frac{1}{\left(1 + \frac{\tau}{\tau_{diff}}\right)} \quad (1.9)$$

1.2.1.2 Autocorrelation function for multiple species

For a mixture of noninteracting fluorescent species undergoing only diffusion in the observation volume with different diffusion coefficients, the fluorescence intensity autocorrelation function is the sum of the contributions of the individual species. The general form of $G(\tau)$ for a mixture of m of different fluorescent species with diffusion time $\tau_{diff,i}$ is given by:

$$G(\tau) = 1 + \frac{1}{N} \sum_{i=1}^m \rho_i g_i(\tau) \quad (1.10)$$

where $g_i(\tau) = \frac{1}{\left(1 + \frac{\tau}{\tau_{diff,i}}\right)} \frac{1}{\sqrt{1 + \frac{\tau}{k^2 \tau_{diff,i}}}}$ and $\rho_i = \frac{\phi_i^2 c_i}{\sum_{i=1}^m \phi_i^2 c_i}$

In the above expressions, ρ_i is the relative amplitude of the molecules with distinct diffusion coefficients, c_i is their concentration and ϕ_i is the quantum yield of species i . (Meseth et al., 1999)

1.2.1.3 Autocorrelation function for triplet contribution

Because of the quantum nature of light and photophysics of fluorescent molecules, the excited fluorophore will not always emit a constant light flux. The point that has to be considered is a transition of the excited molecule in the triplet state. This will interrupt the stream of photons for approximately the triplet lifetime of fluorophore and add another contribution to the autocorrelation function (Widengren et al., 1994; Widengren et al., 1995; Widengren et al., 1999; Haupts et al., 1998; Rigler et al., 1993). For conventional dyes and autofluorescent proteins like GFP, additional fluctuations in fluorescence are seen with increasing excitation intensities as the molecule enter and leave their triplet states.

1.2.1.3.1 Jablonski diagram

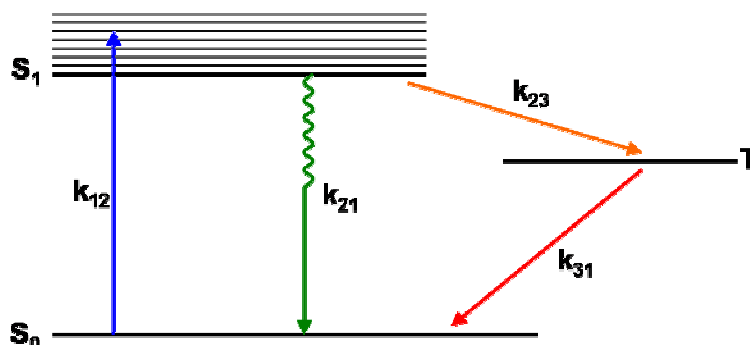
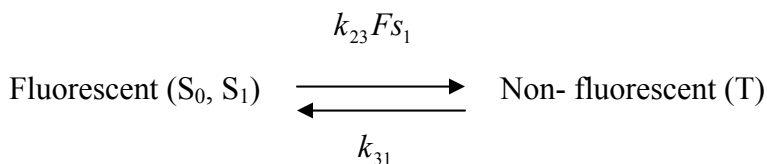


Figure 1.1: Simplified Jablonski diagram for the electronic state model of Rhodamine 6G with rate constants.

The electronic states (for eg., Rh6G) involved in the process of fluorescence can be modeled as shown in figure 1.1. S_0 denotes the ground singlet state, S_1 is the excited singlet state, and T is the lowest triplet state. k_{12} and k_{21} are the rate constants for excitation and deexcitation and k_{23} and k_{31} are the rate constants for intersystem crossing and deexcitation of the triplet state, respectively.

To achieve single-molecule detection, the fluorescent dyes should have high turnover between the excited singlet state S_1 and the ground singlet state S_0 . The rate constant k_{12} of $S_0 \rightarrow S_1$ transition is controlled by the excitation light intensity I , so k_{12} can be written as $k_{12} = \sigma \cdot I$ where σ is the photon absorption cross section. The rate constant k_{21} of the relaxation $S_1 \rightarrow S_0$, that is associated with the fluorescence emission is the inverse of the excited state's lifetime and becomes limiting to the overall turnover rate at high pumping intensities. If strong intensity is applied, the excited state S_1 will be highly populated and transition to the lowest triplet state T is possible before the relaxation into the ground state S_0 . Singlet-triplet and triplet-singlet transitions are non-radiative and slower than the singlet-singlet transition. The more detailed outline about this system is given elsewhere (Widengren et al., 1995).

In FCS, if we treat the dye is fluctuating between a bright state (singlet states) and a dark state (triplet state); we can write a simple chemical reaction (Krichevsky and Bonnet, 2002):



where FS_1 is the fraction of molecules present in the excited state S_1 and is used to normalize the rate constant k_{23} . The sense of using this normalization is that transition into the triplet state is possible only from S_1 and not from S_0 . The description of triplet state kinetics is similar to the description of the isomerization transition between fluorescent and non-fluorescent states only if the non-fluorescing state is thermally reconverted to the fluorescing state (Widengren and Schwille, 2000).

Considering the rate constants for the above system, the expression for autocorrelation function will become:

$$G(\tau) = 1 + \frac{1}{N} \cdot \frac{1}{\left(1 + \frac{\tau}{\tau_{diff}}\right)} \cdot \frac{1}{\sqrt{1 + \frac{\tau}{k^2 \tau_{diff}}}} \cdot \left(1 + \frac{F}{1-F} \cdot \exp\left(-\frac{\tau}{\tau_c}\right)\right) \quad (1.11)$$

where F is the fraction of molecules in the triplet state and τ_c is the chemical relaxation time and is written as:

$$\frac{1}{\tau_c} = k_{23}FS_1 + k_{31} \quad (1.12)$$

The decay of the singlet state by fluorescence or internal conversion is much faster than either of the processes of intersystem crossing or triplet state decay;

$$k_{12}, k_{21} \gg k_{23}, k_{31}$$

We can estimate FS_1 from the equilibrium of the reaction $S_0 \leftrightarrow S_1$ as follows:

$$FS_1 = \frac{k_{12}}{k_{12} + k_{21}}$$

$$\text{Then, } \frac{1}{\tau_c} = \frac{k_{23}k_{12}}{k_{12} + k_{21}} + k_{31} = \frac{k_{23}\sigma I}{\sigma I + k_{21}} + k_{31}$$

At low laser intensity, this mode of relaxation is determined by triplet to ground singlet transition with the rate constant k_{31} and at high intensity, the excited-singlet-to-triplet transition becomes significant and the relaxation rate is $k_{23}+k_{31}$. The triplet transition rates k_{23} and k_{31} are in the order of microseconds and depends on the nature of dyes and solvents. The rate of triplet state population also depends on the excitation intensity by considering FS_1 . Moreover, the triplet dynamics shows a strong dependence on the concentration of molecular oxygen and several heavy metals or halogen ions in the buffer solution, which are known as prominent triplet quenchers. Kinetics of triplet state formation in organic dyes (Widengren et al., 1995 and 1997) and GFPs (Haupts et al., 1998; Widengren et al., 1999) has been characterized by FCS.

1.2.1.4 Multiple component diffusion

One of the main interests of FCS experiment is to explore the molecular interaction between biomolecules. Specifically, these interactions are chemical reactions between different species due to the transition between one state to another state, for example from a free ligand to a bound complex. However, the probability of observing a bimolecular complex dissociation during its passage time through the observation volume is essentially zero. Autocorrelation function for multiple, noninteracting species is sufficient to address binding equilibrium between biomolecules with FCS measurement (Müller et al., 2003).

Consider two species with τ_{d1} and τ_{d2} be the diffusion time of species 1 and species 2, respectively. Then the autocorrelation function for multicomponent three dimensional diffusion can be written as:

$$G(\tau) = 1 + \frac{1}{N} \left[\frac{f_i}{1 + \frac{\tau}{\tau_{d1}} \sqrt{1 + \frac{\tau}{k^2 \tau_{d1}}}} + \frac{1 - f_i}{1 + \frac{\tau}{\tau_{d2}} \sqrt{1 + \frac{\tau}{k^2 \tau_{d2}}}} \right] \quad (1.13)$$

where f_i is the fraction of the diffusing component.

In the case of interaction between ligands and target molecule, the degree of binding can be determined directly from the correlation function using the above equation (Rigler, 1995). Differences in the molecular weight of the two species give rise to different diffusion coefficients. The autocorrelation function of such mixture contains a fast decaying fraction, which originates from the species with larger diffusion coefficient, and a slow decaying fraction with a smaller diffusion coefficient. However, to distinguish two components from the autocorrelation function, their diffusion times must differ by at least a factor of 1.6 for comparable quantum yields and high fluorescence signal (Meseth et al., 1999).

1.2.2 Fitting of FCS data

Using suitable correlation functions, analysis of FCS data were done by fitting the raw data obtained after the measurements. In this work, all FCS data were analysed by means of commercial software (Origin Pro 7.5, Origin Lab, MA, USA) with Levenberg-Marquardt iterations.

The quality of the fit is inspected by the criteria; reduced Chi-square χ^2 and visual inspection of the residuals between experimental and fitted curves. Another feature that can be implemented for the quality of fit is the residual, which is the difference between the fitted function and the experimental data. A more appropriate fit for Fluorescein autocorrelation curve is shown in the figure 1.2. The residual points are located near or in the grid line which passes through zero.

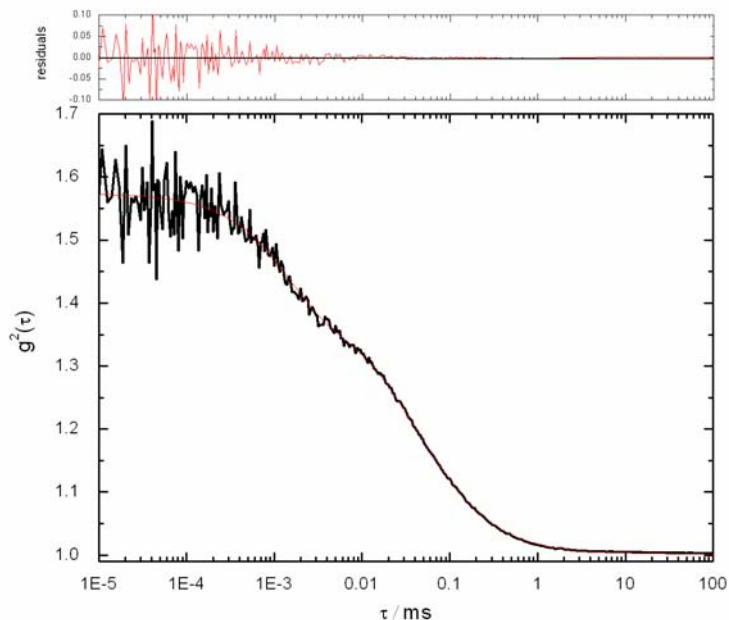


Figure 1.2: Autocorrelation curve for Fluorescein at $\lambda_{\text{exc}} = 488$ nm fitted with the equation 1.11. An appropriate fit is shown in red color. The residuals are also shown in the upper box which tells about the accuracy of the fitting.

Studies have been done for evaluating the resolution of FCS measurements (Meseth et al., 1999), detailed analysis of standard deviation (Wohland et al., 2001) and the accuracy of determining the diffusion coefficient by FCS (Enderlein et al., 2005).

1.3 Experimental considerations

1.3.1 Materials and methods

1.3.1.1 FCS set up

In this section, I will present the experimental implementation of FCS which is used for all the measurements mentioned in this thesis. A schematic diagram of the FCS setup is shown in the figure 1.3.

The FCS experiments were performed with a home-built confocal setup using an inverted microscope (Axiovert 200, Zeiss). At the beginning, an Ar-ion laser, operating at

$\lambda_{\text{exc}} = 488 \text{ nm}$ (Innova I-304 C, Coherent), was coupled into an optical fibre and outcoupled by a 40x objective lens resulting in a parallel laser beam with a diameter of 0.8 mm. In the course of the described experiments, the above mentioned laser was replaced by a frequency-doubled diode laser (Picarro, Soliton), also operating at $\lambda_{\text{exc}} = 488 \text{ nm}$ with a diameter of 0.7 mm. The laser beams were directed to the microscope body without the use of further lenses, and from there deflected by a dichroic mirror (495 DRLP, Omega for all the measurements except R18 labelled membrane where 555 DRLP, Omega was used). The laser was focussed to a diffraction limited spot by a water immersion objective lens (63x NA 1.2 WI, Zeiss). Fluorescence was collected by the same objective and was focussed by the tube lens to a pinhole with a diameter of 50 μm . After additional filtering with a bandpass filter (HQ 525/50, AHF Analysentechnik, for GFPs and Bodipy labelled RBC membrane; HQ 583/120, AHF Analysentechnik, for YFPs; and HQ 590/70, AHF Analysentechnik, for R18 labelled membrane), fluorescence was split by semitransparent mirror and detected by two avalanche photodiode modules (SPCM-14-AQR, PerkinElmer Optoelectronics). TTL-signals, each corresponding to a detected photon, were cross-correlated by a hardware correlator (FLEX 02 D, www.correlator.com) finally yielding the autocorrelation function with nanosecond time resolution. Imaging of RBC was done by using a piezoscanner (Piezosystem Jena GmbH, Germany) attached to the microscope body; images were obtained by a time correlated single photon counting system (TimeHarp 200, PicoQuant GmbH, Germany) and the images were viewed by PicoQuant SCX View software (PicoQuant GmbH, Germany). Silane coated glass coverslips for the measurements in solution containing autofluorescent proteins and dyes were used. For better adhesion of RBC, the glass coverslips have been pre-treated with polylysine.

The power of the laser beam entering the microscope was set to 50-1000 μW for frequency-doubled diode laser and 50-3000 μW for Ar-ion laser for the measurements with autofluorescent proteins. For RBC membrane measurements, the power was set to 10-15 μW .

1.3.1.2 Samples

EGFP was obtained from Clontech and SEYFP was a kind gift of Prof. Harms, Würzburg University, Germany. The GFP mutants were concentrated to a final concentration of ~ 1 mg/ml. Small quantities were serially diluted in a buffer at pH 10 (HPCE-grade, Fluka) to micromolarity for fluorescence spectra and to the nanomolar range for the FCS experiments. A drop of such a solution was put on top of a silanized cover slide with specified thickness of 0.17 mm. The high pH was chosen to avoid complications due to external protonation as described before (Jung et al., 2001).

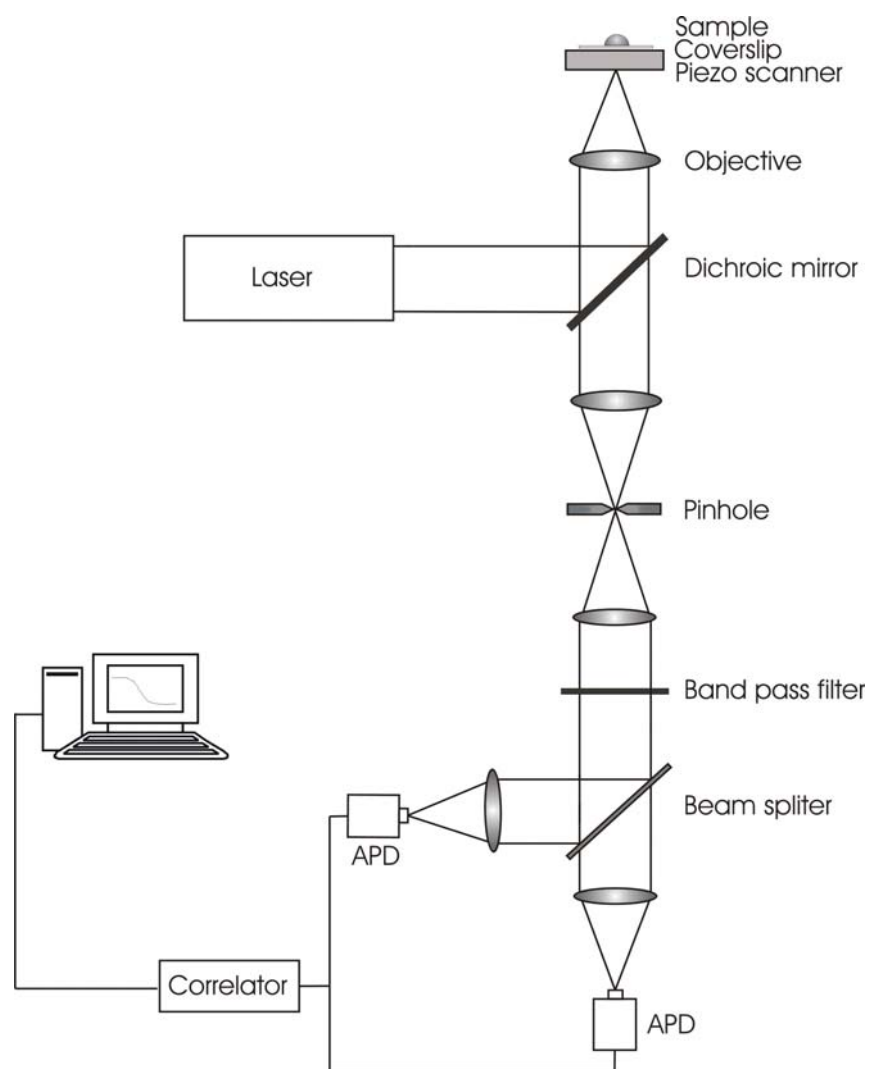


Figure 1.3: A schematic diagram of FCS setup.

1.3.1.3 Fluorescence excitation and emission spectra

Fluorescence excitation emission spectra were taken with a commercial fluorescence spectrometer (Jobin Yvon-SPEX Instrument S.A, Inc.) at pH 10. The optical resolution of the spectra was 1 nm. Excitation spectra were corrected by the use of a highly concentrated Rhodamine B solution as reference quantum counter (Yguerabide, 1968).

1.3.1.4 Time-Correlated Single-Photon Counting (TCSPC)

Fluorescence lifetime measurements were performed by using a custom-built setup. The set up consists of a pulsed laser with a pulse width of 60–120 ps at wavelength of excitation 470 nm. The diode laser driver unit (PDL 808 MC SEPIA, Pico-Quant, Germany) is connected to the single-photon avalanche detector (PDM 100ct SPAD, Micro Photon Devices, Italy) and a photon counting device (PicoQuant Microtime, Germany). The overall instrumental response function was between 200 and 300 ps. The lifetime data were analysed by commercial software (SymPhoTime, PicoQuant, Germany).

1.3.2 Practical Considerations

The following practical considerations of FCS set up are described in detail by Krichevsky and Bonnet (2002). The essential requirement of an FCS measurement is the fluorescence of the compound under study. A huge variety of dyes are commercially available for fluorescence experiments but not all dyes would perform well in an FCS experiment. The characteristics of the dyes for the FCS experiments are high extinction coefficient, high fluorescence quantum yield, low singlet-to-triplet state quantum yield and low photobleaching. Derivatives of rhodamine like tetramethyl rhodamine (TMR) and carboxyrhodamine (Rh6G) are well suited for these requirements. However, the photodynamics of a dye might change upon binding to the compound of interest.

The main requirement of the laser source is the stability of its intensity. Laser intensity fluctuations can not separate from the fluorescence fluctuations caused by the

sample of interest. A Gaussian laser beam leads to a small focus which is limited only by diffraction.

Most FCS experiments require high numerical aperture (NA) objectives. Oil-immersion objectives are having the highest NA but their optical quality is reliable only when the focal plane is right at the surface of the glass. Due to optical aberrations as well as sub-optimal fluorescence, these objectives are not suitable for focusing laser deeper inside the aqueous samples. This problem is solved by water-immersion objectives.

Pinholes are available in many different sizes, typically the pinhole diameter should be about 30-50 μm , depending on the objective. Optimization of the pinhole size was discussed in the literature (Rigler et al 1993). The best signal to background values is obtained with pinholes of the size of the image of the laser beam waist in the plane of the pinhole.

In FCS, it is very essential to use detectors with high quantum efficiency. APDs have higher quantum efficiency in the visible region than photomultipliers and their sensitivity extends to the near infrared. Sensitivity of APD drops off drastically in the blue part of the spectrum where photomultipliers perform better than APDs. Photomultipliers and APDs have a problem of afterpulsing, which can be efficiently dealt with splitting the light between two detectors.

Nowadays, data acquisition boards are all based on the multiple-tau correlator design, which is able to calculate the autocorrelation function for evenly logarithmic sampling frequencies. These data acquisition schemes provide access only to the autocorrelation function but not to the complete time sequence of photon counts. Electronic cards that provide a time-stamp for every photon event represent a different data acquisition strategy and are commercially available (Eid et al., 2000).

1.3.3 Confocal volume

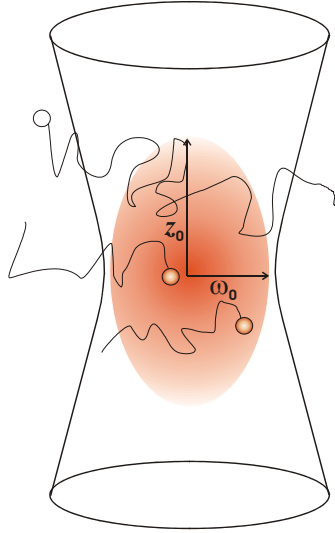


Figure 1.4: A schematic view of the observation volume (shaded area) in which the fluorescent molecules undergo random movement. ω_0 and z_0 are the distances from the centre in the radial and axial directions.

The spatial resolution of a confocal fluorescence microscope is usually described by the confocal volume, which is the excitation volume within the sample that is detected by the confocal optics. It depends on the intensity profile $I(\vec{r})$ and the collection efficiency function $CEF(\vec{r})$ that describes the effect of a pinhole in the detected light intensity. The observation volume $W(\vec{r})$ is given by:

$$W(\vec{r}) = I(\vec{r})CEF(\vec{r}) \quad (1.14)$$

where \vec{r} is the spatial coordinate.

The detected light in a confocal setup is spatially filtered by a pinhole positioned in the image plane of the microscope. The pinhole transmits only the light from the focal plane and this spatial filtering can be described by the collection efficiency function (Koppel et al., 1976). The collection efficiency function can be expressed as:

$$CEF(r, z) = \frac{1}{A} \int T(r)PSF(r, r', z)d\vec{r} \quad (1.15)$$

where A is the normalization factor, $T(r)$ is the transmission function of the pinhole and PSF is the point spread function of the microscope.

The intensity profile $I(\vec{r})$ is contributed by the laser beam which is focused to the diffraction limited spot and this makes relatively small observation volume. The intensity profile of this laser beam with output power P has a Gaussian-Lorentzian intensity profile and is given by (Rigler et al., 1993):

$$I(r, z) = \frac{2P}{\pi w^2(z)} e^{-2r^2/w^2(z)} \quad (1.16)$$

where r is the radial coordinate of the point source in the sample space and $w(z)$ is the radius of focused laser beam.

After several approximations, the observation volume can be approximated as a Gaussian intensity distribution along the three coordinate axis.

$$W(r, z) = \frac{2P}{\pi w_0^2} e^{-2r^2/w_0^2} e^{-2z^2/z_0^2} \quad (1.17)$$

z_0 is the distance from the focus along the optical axis where the intensity dropped to $1/e^2$ of its value in the focus as shown in the figure 1.4.

1.4 Diffusion

FCS measurements with GFP show a variety of relaxation process. Most of these kinetic effects in the FCS curves are due to the photodynamic process or proton transfer that results from the variation of excitation intensity or ambient pH and buffer conditions (Widengren et al., 1999). In order to discuss the different time scales in FCS curve, we can choose the FCS curve of GFP. In this dynamic process, three different time domains can be observed. These are rotational diffusion in the nanosecond time-range, photodynamic process involving triplet state formation as well as additional excitation intensity dependent process in the microsecond time-range, and translational diffusion

and photodegradation in the millisecond time-range. In the first data points of the correlation curves, a negative process can be observed, which is consistent with photon anti-bunching. These processes are depicted in the figure 1.5. For freely diffusing molecules, rotational and translational scales are determined by the radius of the molecule and the viscosity of the buffer. The rotational diffusion time can be computed with the diffusion of its own scale, while the translational diffusion time is linear with radius of the molecule.

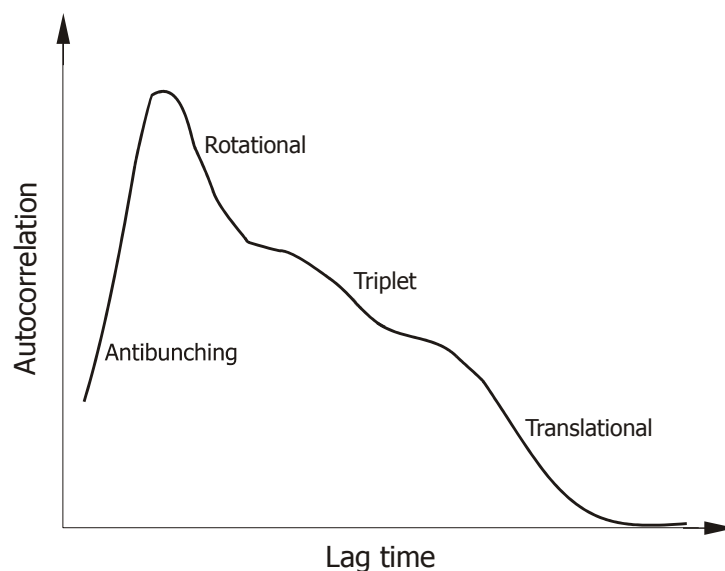


Figure 1.5: A schematic autocorrelation curve with various time scales of different processes are shown.

The excitation of a dye molecule depends on the angle between its excitation dipole moment and the polarization vector of exciting light. Due to this, freely rotating dye molecule's excitation rate and emission are fluctuating and these fluctuations contribute to the FCS correlation function - a term with the characteristic time scale of rotational diffusion (Ehrenberg and Rigler, 1974; Aragon and Pecora, 1975). The time scale of rotational diffusion is small and is comparable to the anti-bunching time, dead time of the detector and the triplet relaxation time. Because of this similarity, detection of rotational diffusion time is difficult. Even though in several studies, rotational diffusion has been detected either due to the bulkiness of molecules or aggregates.

Rotational diffusion time for acetylcholine receptor tagged with Rhodamine 6G - coupled α -bungarotoxin was detected as 16 μ s (Rauer et al., 1996). Rotational diffusion of GFP has also been reported with a rotational time of \sim 20 ns which is consistent with its molecular size (Widengren et al., 1999). The rotational diffusion relaxation has a well defined time scale in autocorrelation function and thus can contribute to the analysis of molecular size.

Measurement of translational diffusion is the simplest FCS measurement. Here the molecule of interest can be labeled with a fluorescent dye and its motion in the sample volume results the correlation function of equation 1.6 and 1.9 with the characteristic translational diffusion time. Translational diffusion of biomolecules has equally assessed by FCS and FRAP. The advantages of FCS over FRAP are that 1) in FCS the photobleaching is minimized and 2) it requires only a small amount of fluorophore for the measurement (Weiss and Nilsson, 2004).

Studying the triplet relaxation time is more complicated than the other two types of diffusion as it involves additional fluctuations and unknown excited states of the molecule. A more detailed picture of triplet relaxation is described in section 1.2.1.3.

Another interesting phenomenon can be easily reproduced by FCS is the anomalous subdiffusion of proteins such as receptor molecules in the cell membranes. In this case, the mean square displacement of molecules in their random walk is not linear, but rather proportional to the time at fractional exponents (Bouchaud et al., 1990). For normal (Brownian) diffusion, the mean square displacement is proportional to time ($\langle \Delta r^2 \rangle = 4D\tau$) where as in anomalous subdiffusion, the mean square displacement is not linear but is given by $\langle \Delta r^2 \rangle = \Gamma \tau^\alpha$, where Γ is the transport coefficient and the value of temporal exponent α lies between zero and one (Schwille et al., 1999b). The deviation from the normal Brownian diffusion of single molecules can be due to the heterogeneity of molecular environments, local confinements or nonspecific interactions with other membrane-bound particles. Not only the membrane bound proteins exhibit anomalous diffusion, but also lipids or lipid like molecules show considerable deviation from the normal homogeneous diffusion when they are observed on natural cell membranes (Schwille et al., 1999b). Other than membrane diffusion, several probes show anomalous

diffusion owing to nonspecific interactions with the cellular environment. Diffusion of GFP in the nucleus can also be described as anomalous, even though normal diffusion is observed in the cytosol (Wachsmuth et al., 2000).

A slow transport phenomenon, which is also called active transport, can also be studied by FCS. FCS allows to distinguish active transport from diffusion on time scales of micro - to milliseconds, and which requires subnanomolar concentrations of fluorescent molecules.

1.5 Fluorescent probes

As discussed in section 1.2.1.3.1, fluorescence is a form of luminescence in which fluorophores emit light that occurs within nanoseconds after the absorption of light of shorter wavelength. The criteria that makes the fluorescence more powerful than other luminescence is the Stokes shift, which is the difference between the excitation and emission wavelengths. Efficiency of a fluorophore and the wavelength of absorption and emission are determined by their outermost orbitals. When a fluorescent molecule in its ground state absorbs light energy in the form of photons, alterations in the electronic, vibrational and rotational states of the molecules can occur. The absorbed energy can move an electron from the highest occupied molecular orbital (HOMO) into the lowest unoccupied molecular orbital (LUMO). This transition to the excited state occurs in femtoseconds.

Many organic molecules have autofluorescence and some are useful for specific labeling of components in biological systems. Such compounds are aromatic molecules with π bonds that can easily distribute outer orbital electrons over a wide area. These compounds need only low excitation energy.

1.5.1 Fluorescent dyes

In the beginning of FCS development, the FCS measurements were done by using fluorophores that are already known from fluorescence spectroscopy and microscopy techniques. High quantum efficiency, large absorption cross section and photostability

are the key requirements of fluorophores for single-molecule techniques. Fluorescein is considered as a good fluorophore but it already photobleaches at low excitation intensities. Nowadays, it is mostly substituted by Alexa 488 dye from Molecular probes. Alexa dye family exhibits a large selection of different colors with absorption maxima ranging from 350 nm to 750 nm, covering more than the visible spectrum. Other suitable dyes for single-molecule applications are Rhodamine dyes (Rhodamine Green, TMR, Rhodamine B, Rhodamine 6G) and cyanines (Cy2, Cy3, Cy5).

1.5.2 Green fluorescent proteins

The green fluorescent protein (GFP) from the jellyfish *Aequorea victoria* is the most studied and exploited proteins in biochemistry and cell biology. Martin Chalfie, Osamu Shimomura and Roger Y. Tsien were awarded the 2008 Nobel Prize in Chemistry for the the discovery and development of the GFP.

The chromophore of this protein is completely encoded in the amino acid sequence and can fluoresce only after correct folding of the beta barrel and in the presence of molecular oxygen (Cody et al., 1993; Reid and Flynn, 1997). The function of the barrel which is having a diameter 24 Å and height 42 Å (Yang et al., 1996) is to protect the chromophore from quenching by molecular oxygen. This chromophore consists of amino acid residues Ser-Tyr-Gly at positions 65-67 which undergoes post translational modifications to become p-hydroxybenzylideneimidazolinone (Cody et al., 1993; Prasher et al., 1992) making the protein fluorescent. Mechanism of chromophore formation is shown in the figure 1.6. Wild-type (wt) GFP has a dual excitation peak at 395 nm and 475 nm, and emits green light at 508 nm with a quantum field of 0.72-0.85 (Morise et al., 1974; Patterson et al., 1997; Ward et al., 1982). The peak at 395 nm arises from the GFP molecule containing neutral chromophores, whereas deprotonated and anionic chromophores contribute to the peak at 475 nm (Cubitt et al., 1995; Heim et al., 1994). The existence of both chromophores leads to some disadvantages for cell biological applications. However, mutagenesis of GFP yielded several classes of proteins with improved properties.

Tsien (1998) classified GFPs into seven classes depending on their chromophore photophysics. Among these proteins, enhanced green fluorescent protein (EGFP) and enhanced yellow fluorescent protein (EYFP) are widely used in biological applications.

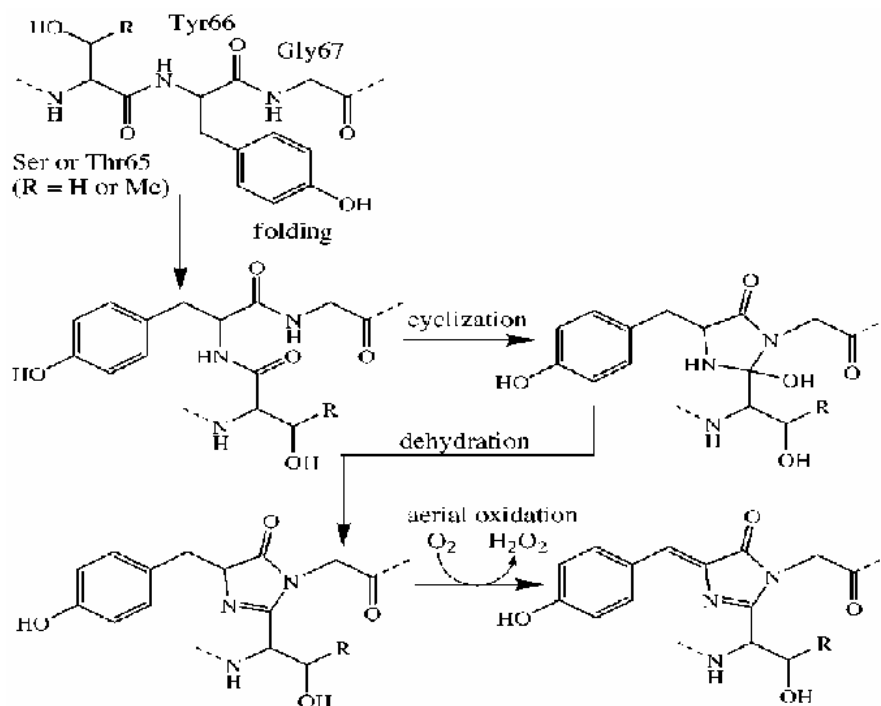


Figure 1.6: Proposed biosynthetic mechanism for the formation of GFP (Heim et al., 1994; Cubitt et al., 1995), in which cyclization precedes oxidation (Figure adapted from Tsien, 1998).

1.5.2.1 Enhanced green fluorescent protein

EGFP is the most widely used mutant among *Aequorea victoria* green fluorescent proteins (avGFPs). The two amino acid substitutions F64L and S65T are responsible for the quick formation of chromophore, single excitation peak at 489 nm and improved protein folding efficiency that makes the chromophore 35-times brighter than the wt-GFP when excited at 488 nm (Heim et al., 1995; Cormack et al., 1996; Yang et al., 1996). EGFP is very stable and is fluorescent in monomeric and dimeric form.

1.5.2.2 Enhanced yellow fluorescent protein

EYFP protein contains substitutions such as S65G, V68L, S72A and T203Y and it contains 12 Tyrosine residues, Tyr66 being an integral part of the chromophore. Additional Tyr at position 203 lies close to the chromophore and is having a π - π stacking between the chromophore (Wachter et al., 1998). It is the most red shifted commercially available *av*GFP and this red shifting is due to the additional polarizability of π -stacked Tyr203.

1.5.2.3 Folding of GFP

Folding of GFP in to the 11-strand β -barrel is essential in the formation of chromophore and its fluorescence. The β -barrel protects the chromophore residues 65-67 and is responsible for the stability of GFP (Ward and Bokman, 1982). GFP exhibits reversible denaturation; the fluorescence is fully diminished in the denatured GFP (Bokman and Ward, 1981) but it is regained up on the reformation of β -barrel. A ribbon diagram of wt-GFP structure is shown in the figure 1.7.

GFP is fluorescent in the soluble form and the incorrect folding results the aggregation as insoluble inclusion bodies (Kane and Hartley, 1988). The misfolding may cause insufficient maturation, therefore mutants have been designed which are favorable at higher temperature. These folding mutants can be divided in to four groups: 1) those that are buried and in close proximity to the chromophore (e.g., S65A, G, T or L, F64L and S72A which promotes chromophore formation), 2) buried residues that are located far from the chromophore (e.g., V163A which favors productive folding intermediates at higher temperature), 3) surface mutations close to the chromophore and 4) surface mutations far from the chromophore (Cubitt et al., 1999) (e.g., F99S/M153T/V163A may aid in decreasing the surface hydrophobicity (Fukuda et al., 2000)).

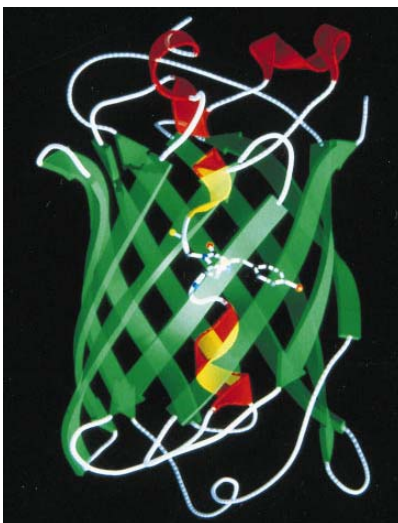


Figure 1.7: Ribbon diagram of the wt-GFP structure. The α -helices are shown in red, the β -strands are shown in green, and the chromophore is shown as a ball-and-stick model (Adapted from Brejc et al., 1997).

Folding rates of wt-GFP and GFP mutants are different in bacteria and mammalian cells (Sacchetti et al., 2001) and this difference is due to the influence of chaperones (Sakikawa et al., 1999; Weber-Ban et al., 1999). The most widely studied folding mutant is Cycle 3 (F99S/M153T/V163A) (Crameri et al., 1996). There are only a few differences between the Cycle 3 mutant and wt-GFP (Fukuda et al., 2000). The increased thermosensitivity of GFP in bacteria and yeast is the result of improved folding due to V163A and S175G mutations (Siemering et al., 1996). The mutations V163A and F64L, yield more soluble protein and improved levels of fluorescence in mammalian cells grown at 37°C (Palm et al., 1997). The folding of β -sheets is not clearly understood. Because the fluorescence occurs only after the formation of chromophore and that only occurs after the formation of 11-strand β -barrel.

1.5.3 Photobleaching

Photobleaching is the process in which fluorophore in their excited state have a certain probability to undergo irreversible destruction. This irreversible process occurs when an excited state chromophore reacts with free radical to form a nonfluorescent product and

there are several additional pathways involving in this process. This phenomenon is of great importance in FCS and single molecule spectroscopy, where one tries to maximize the fluorescence emission of individual particles.

The photobleaching of a dye solution can be noted by the quantum yield of photobleaching ϕ_{bl} . For a two-quantum excitation of molecules in a solution, it is given by (Nikogosyan, 1987):

$$\phi_{bl} = \frac{\text{number of photobleached molecules}}{\text{total number of absorbed photons}}$$

Here the total number of absorbed photons also includes those photons absorbed in the first excited state leading to higher excited electronic states, which open up to new photobleaching channels (Nikogosyan, 1987; Khoroshilova et al., 1990)

Photobleaching is independent of excitation intensity at low illumination. This depicts that, for each dye there is a characteristic number of photons emitted before the dye undergoes photobleaching. At high illumination intensities, this process is more complicated with photobleaching kinetics with a number of excited states (Eggeling et al., 1998). Eggeling et al characterized the photobleaching kinetics by means of FCS.

GFPs are resistant to photobleaching thus allowing prolonged visualizations under low-intensity imaging conditions in confocal microscopy. In cellular applications, GFPs bleach irreversibly without detectably damaging intracellular structures at high intensity illuminations (Patterson et al., 1997). This is because the cylindrical β -barrel protects the chromophore from its cellular environment and the cell from reactive intermediates generated by photobleaching (White and Stelzer, 1999).

1.5.4 Blinking of GFP molecules

High stability, efficient fluorescence in the green spectral range with quantum yields around 0.8 and the potential to express in fusion proteins and organelles makes the GFP more popular in *in vivo* studies by fluorescence microscopy and spectroscopy (Tsien,

1998). However, GFP is hardly bright enough for *in vivo* localization studies in single-molecule level (Kubitscheck et al., 2000), explained by several FCS studies (Haupts et al., 1998; Widengren et al., 1999; Schwille et al., 2000; Jung et al., 2001).

A strong light dependent blinking behavior of yellow shifted mutants T203Y and T203F were first studied by Dickson et al., (1997). In this work, GFP mutants were immobilized in aerated aqueous polymer gels and excited by 488 nm light which undergo repeated cycles of fluorescent emission - known as blinking - on a timescale of several seconds. The GFP molecules reach a long lasting dark state but on irradiation with 405 nm light, the molecules can be switched back to the original form.

When subjected to FCS studies, these mutants showed a flickering phenomenon having a time scale of 10 μ s to 100 μ s (Schwille et al., 2000). This reversible excitation driven transitions from the anionic bright state to the nonfluorescent dark state has a quantum efficiency of $\sim 10^{-3}$. The transition rate τ_e^{-1} depends linearly on the intensity of excitation whereas the fraction of molecules residing in the dark state is independent of excitation intensity implies an equilibrium between the two molecular states having different spectroscopic properties. This flickering only depends on the illumination intensity, not on the different functional form of proteins or on the molecular environment and can make unwanted artifacts in cellular applications.

Another flickering phenomenon from mutants EGFP (F64L/S65T) and GFP-S65T by FCS showed pH dependent conformational fluctuations (Haupts et al., 1998). Fluorescence excitation of a bulk solution of EGFP decreases to zero at low pH (pKa 5-5.8) accompanied with a decrease of the absorption at 488 nm and an increase at 400 nm. These changes are induced by the protonation of the hydroxyl group of Tyr-66, from the chromophore. The fluctuations in the protonation state of the chromophore are time resolved by implementing FCS. The autocorrelation function of fluorescence emission shows contributions from two chemical relaxation processes as well as diffusional concentration fluctuations.

1.6 Experimental studies with FCS

1.6.1 FCS and binding assay

FCS can be used to monitor bimolecular interactions in which a small compound (a ligand) binds to a bigger molecule (the ligand's receptor). When a small fluorescent molecule binds to a large nonfluorescent molecule, a decrease in diffusion time observed through the sampling volume. In this experiment, two kind of diffusion can be seen in the correlation curve, one from the fast diffusion of a small compound and the other from the slow diffusion of the complex. According to equation 1.13, it is also possible to calculate the concentration of bound and unbound fractions as well as the total number of compounds.

Several different studies in ligands and proteins have been performed using this method of analysis. Determining the binding constants of fluorescent ligands with solubilized form of 5-hydroxytryptamine receptor (Wohland et al., 1999), strength of binding between the subunits of ATP synthase enzyme (Hasler et al., 1999), interaction between human estrogen receptor α and the fragment of its coactivator protein SRC-1 in the presence of ligands such as estradiol (Margeat et al., 2001) and several other experiments on binding of ligands to their receptors or to their proteins (Borsch et al., 1998; Meyer-Almes et al., 1998; Pack et al., 1999; Schuler et al., 1999; Schurer et al., 2001) have been successfully reported in the earlier FCS experiments. Statistical analysis of ligand binding studies have been performed in several studies (Chen et al., 2000; Van Craenenbroeck and Engelborghs, 2000).

An elegant procedure that makes a difference from the above FCS experiments is the study of interaction of peptides such as melittin and mangainin with lipid vesicles labeled with rhodamine (Pramanik et al., 2000).

Binding measurements in which the change in the diffusion time depends on the difference in the size of the interacting molecules. For more reliable FCS data, the ratio of diffusion coefficients of the labeled molecules and the bound complex should be

smaller than a certain factor which is generally in the range of 1.6-10 (Meseth et al., 1999). This depends on the fluorescence yield and the relative fractions of compounds.

1.6.2 FCS in cells

FCS is one of the major tools used for intracellular applications. It is because, FCS do not require any external perturbation to obtain kinetic information and it provides excellent spatial information. The subfemtoliter observation volume allows the investigator to probe specific organelles and other local regions within a living cell.

For an *in vivo* FCS experiment it is very necessary to choose the right fluorescent probes. It should only label the protein of interest and do not take part in any interactions with the cellular environment. Nowadays GFP is widely used as a marker protein for imaging and functional studies of proteins in living cells. Characterization studies of EGFP in HeLa cells showed a slowing down of diffusion coefficient which is due to the viscosity of the cellular environment (Chen et al., 2002). This experiment concludes that EGFP is a good fluorescent probe for *in vivo* measurements as it does not stick to the cellular components in the nucleus and cytoplasm. Using FCS, application of GFP fusion proteins in *in vivo* were done by choosing the protein of interest as epidermal growth factor receptor (EGFR) (Brock et al., 1998). FCS is used to measure the intracellular concentration of a GFP-labeled chemotactic signaling protein with a flagellar motor activity in *Escherichia coli* (Cluzel et al., 2000).

Living cells generate a very high autofluorescence and this makes challenging for the single fluorescent molecule detection. The autofluorescence from the mammalian cells comes from NAD, flavins and lipofuscin (Aubin, 1979; Benson et al., 1979). Autofluorescence intensity depends on the different cellular compartments of the cell. Normally, the autofluorescence intensity is weak and homogeneous inside the nucleus where as strong and inhomogeneous inside the cytoplasm.

FCS has been widely used in the characterization of membrane receptors in living cells. A prospect of these experiments is the development of novel drug screening protocols. Diffusional FCS has been used to study the binding of proinsulin C-peptide to

specific G-protein-coupled receptors in human cell membranes (Rigler et al., 1999), diffusional heterogeneity of ligand-labeled insulin receptors (Zhong et al., 2001), epidermal growth factor receptors (Pramanik and Rigler, 2001) and galanin receptor diversity on insulinoma cells (Pramanik et al., 2001). Imaging FCS has also been used for characterizing cell surface receptor distributions (Srivastava and Petersen, 1998; Wiseman and Petersen, 1999) and counting dendritic spines in brain tissue slices (Wiseman et al., 2002).

The use of FCS to probe the intranuclear dynamics is challenging, even though many successful stories have been reported in recent years. FCS measurements in living cells were done to probe intracellular diffusion and concentration of messenger RNA in their nucleus (Politz et al., 1998). Spatial variations of the diffusion behavior of the green fluorescent protein mutant EGFP (F64L/S65T) and of the EGFP- β -galactosidase fusion protein in living cells is also studied by fluorescence correlation spectroscopy (Wachsmuth et al., 2000).

Very recently, several challenging FCS studies were done in cells. Diffusion of bacteriophage through model biofilms (Briandet et al., 2008) and anomalous diffusion of fluorescently tagged gold beads in the cytoplasm (Guigas et al., 2007) are some of them.

1.6.3 Aggregation measurements

The sensitivity of FCS is suitable for studying molecular aggregation. Due to their different intensity and diffusion coefficient, aggregates are easily identifiable. When fluorescently labeled molecule aggregate to form a cluster, these clusters emit a fluorescent burst that is larger than the unbound molecule. Aggregates stay inside the excitation volume longer time due to their increased mass. If an aggregate moves through the observation volume, then its properties dominate in the detected fluorescence signal and a single movement is sufficient to produce disturbance in the correlation curve.

Molecular aggregation and receptor clustering have been found to be an important signaling mechanism for both synaptic plasticity and pathology. FCS can be used for the diagnosis of Alzheimer's disease in which the principle of seeded polymerization in

combination with FCS allowed to detect fluorescently labeled amyloid β -peptide aggregation in the human cerebrospinal fluid samples (Pitschke et al., 1998). Temporal decay of autocorrelation function on changes in molecular size has been used for studying the mechanism of prion-protein multimerization (Post et al., 1998), clustering of ionotropic 5HT3 receptor in plasma membranes (Pick et al., 2003) and L-type Ca^{2+} aggregation (Harms et al., 2001).

1.6.4 Conformational fluctuations of DNA molecule

Nucleic acids (DNA and RNA) are the molecules of choice in many FCS experiments. The polymeric structures with diverse base composition make them appropriate to study bimolecular folding. The development of DNA bioconjugation chemistry allows to attach fluorophores and quenchers at specific locations. Molecular beacons are single stranded DNA whose sequence imposes a spontaneous folding into a hairpin loop which allows to detect specific oligonucleotides in solution (Tyagi and Kramer, 1996). A fluorophore and a quencher are covalently attached at the two ends of the DNA molecule. When the hairloop is closed, the fluorophore and the quencher are in close proximity and the fluorescence is quenched while when the loop opens up, fluorophore and quencher are pulled apart and the fluorescence of the dye is restored. Thus molecular beacons serve as a probe for conformational studies and their excellent fluorescence signal makes the detection of the fluctuation very sensitive.

Molecular beacons spontaneously fluctuate between its open state and closed state in solution and these fluctuations can be detected by FCS (Bonnet et al., 1998). FCS is applied to study the fluctuations of TMR emission in the vicinity of DNA (Edman et al., 1996). Pulsed excitation fluorescence decay of TMR shows two characteristic lifetimes and the intercalation of TMR with the neighboring DNA bases could explain the shorter lifetime of the dye.

1.6.5 Pharmaceutical applications

Like most of the fluorescence techniques, FCS also entered in the highly promising field of drug discovery. FCS has been used for drug characterization and high-throughput screening in pharmaceutical drug discovery (Sterrer and Henco, 1997). More recently, it is used to measure the diffusion coefficient of drugs within the living cells (Brock et al., 1998; Politz et al., 1998; Schwille et al., 1999a). Interaction between Rhodamine labeled oligonucleotide and cationically charged peptide, protamine, to form proticles were studied by FCS. The results proved the usage of FCS in the characterization and development of drug delivery systems (Delie et al., 2001). Due to the high sensitivity of FCS, ligand- receptor interactions at low expression levels in cells are also possible.

FCS has been used for the study of several G-protein-coupled receptors (GPCRs). The binding behavior of Alexa labeled musimol derivative, a GABA agonist, to the GABA_A ionotropic receptor was analysed at rat hippocampal neurons by FCS (Meissner and Haberlein, 2003). FCS was used to study the pharmacology of A1-adenosine receptor (A1-AR), which has significant pathophysiological importance in disorders such as heart arrhythmias, asthma and stroke (Briddon et al., 2004). Recently, FCS experiment in cultured human cerebral cortical neurons shows that, in Alzheimer's disease, the amyloid beta-peptide (Abeta) destroys cells by effecting cell membranes via receptor or target molecule (Hossain et al., 2007). Kinetics of insulin's binding to its receptor was also explained by FCS (Zhong et al., 2001).

Recent advances in FCS, such as total internal reflection-FCS (Leutenegger et al., 2006; Ohsugi et al., 2006; Thompson et al., 1981) and combination of two-colour cross-correlation FCS and molecular brightness analysis, will provide further improvement in making it as a powerful technique for quantifying the diffusion of receptors and ligand-receptor complexes in living cell membranes.

1.7 Variations of FCS

FCS is a versatile technique which offers many possibilities in single molecule studies. Improvements have been done for new possibilities for the FCS measurements. In this section I will sketch some techniques that are related to FCS or alternatives to the standard confocal setup.

The implementation of two-color FCS (Schwille et al., 1997) opens the door to many experiments such as binding studies. In this method, the fluorescence is simultaneously detected at two wavelengths from the two different-color fluorescent species and each of the detectors detects the fluorescence of either of the species. The cross correlation function is sensitive only to the motion of the molecules of both components.

Two-photon confocal microscopy (Denk et al., 1990) is another important technique which is suited for in vivo experiments. The high optical resolution is achieved by the use of molecular excitation by the simultaneous absorption of two photons. The main advantage of two-photon microscopy is that there is no need of a pinhole to cut out the background fluorescence and it uses near infrared photons which allows visualization of deeper structures in cells or tissues.

Standard FCS is relatively sensitive to immobile or slowly moving particle because of the inadequate statistics. This can be examined by scanning the sample through the laser beam for obtaining the correlation in space domain (Petersen et al., 1993; Srivastava and Petersen, 1998; Wiseman and Petersen, 1999) and this is termed image correlation spectroscopy.

Time-gated FCS (Lamb et al., 2000) uses the fact that different fluorophores have different excitation state lifetime distributions and can change upon binding to other molecules. By using pulsed laser excitation and laser-synchronized gating in the detection channel and there by suppressing the photons emitted within a certain time interval after excitation.

Chapter 2

Photostability of green and yellow fluorescent proteins with fluorinated chromophores, investigated by fluorescence correlation spectroscopy

The content of this chapter have been published in
Biophysical Chemistry 136 (2008) 38-43 (S. Veetil, N. Budisa and G. Jung)

2.1 Background

In the past dozen years, Autofluorescent Proteins (AFPs) became indispensable tools in life sciences (Sullivan and Kay., 1999). The importance emerged from their fluorescence which forms spontaneously from the amino acid chain without the need of cofactors or modifying enzymes (Chalfie et al., 1994). With the finding of coral chromoproteins with fancy photophysical properties, applications tremendously blew up and, hence, cover nowadays all areas of fluorescence based technology (Verkhusha and Lukyanov, 2004). In microscopy, their usage ranges from multicolour labelling of cell compartments via quantifying physiological parameters by FRET-approaches to tracing and counting of tagged proteins by single molecule detection schemes (Xie et al., 2006). However, especially those applications which require high excitation intensities suffer from the limited fluorescence survival time of these proteins. Photodestruction of the chromophore is assumed to be the main reason for fluorescence interruption, although it was shown that fluorescence was recovered by the decay of exceptionally long-living dark states (Jung et al., 1998). Photobleaching therefore subsumes these processes, and the molecular quality “photostability” characterizes the different AFPs to withstand them. Deciphering the molecular basis for the underlying chemical transformations might assist to overcome those limitations. Comparative investigations of different AFPs, which were successfully applied to unravel pathways of internal conversion and excited-state proton transfer, ought to support the finding of molecular mechanisms of photobleaching (Jung et al., 2005). The strategy here relies on the modification of the chromophore by fluorination thereby circumventing the limited variety of natural chromophore structures with similar electronic transition energies.

In the present study, global replacement of tyrosine by 2-fluorotyrosine, i.e. (2-F) Tyr and 3-fluorotyrosine, i.e. (3-F) Tyr in EGFP and EYFP mutants, were produced in Tyr-auxotrophic *E. coli* strains (Bae et al., 2004; Pal et al., 2005). Due to the different electronic properties of C-F bond compared to the C-H bond, the replacement of hydrogen with fluorine in AFP chromophores is expected to be accompanied by differences in their optical properties (Budisa et al., 2004). Measuring the photostability of fluorophores which are principally appropriate for single molecule research imposes practical problems. Imaging techniques are based on the analysis of detected fluorescence photons but require good statistics to average out orientational heterogeneities (Harms et al., 2001). Furthermore, if immobilized molecules are analyzed, the influence of the support has to be considered. Experiments in the fluid phase, notably Fluorescence Correlation Spectroscopy (FCS), were used to determine the

photostability of fluorescent dyes (Eggeling et al., 2005; Widengren et al., 2007; Widengren et al., 2006). In FCS, photodestruction appears as a reduction of the residence time in the detection volume. Despite the easy performance of FCS, the analysis of photostability is hampered by the excitation profile of a heavily focused laser beam which is inhomogeneous and perpendicular along the direction of propagation. With no photobleaching occurring, an intensity dependent increase of the diffusional time can be discerned under these excitation conditions (Gregor et al., 2005). This experimental observation is ascribed to fluorescence saturation in the central part of the detection focus and a concomitantly stronger contribution of out-of-focus parts to the correlation curve. Furthermore, a practical, analytical solution for the combination of diffusion and photobleaching is not available yet.

In the present work, the mentioned shortcomings of FCS are circumvented by a careful experimental design, consideration of saturation effects and a comparative analysis of the photostability.

2.2 Materials and Methods

A detail description of sample and experimental set up are outlined in 1.3.1 (chapter 1)

2.2.1 Analysis of FCS data

Intensity dependent FCS data were analysed according to equation 2.1 by means of commercial software (Origin Pro 7.5, Origin Lab, MA, USA).

All depicted autocorrelation curves were normalized with respect to the number of molecules in the detection volume N (figure 2.1).

$$g^2(\tau) = 1 + \frac{1}{N} \left(\frac{1}{1 + \left(\frac{\tau}{\tau_d} \right)} \right) [1 + C \cdot \exp(-k\tau)] \quad (2.1)$$

In this so-called two-dimensional model, which is valid for the pinhole diameter used here (Rigler et al., 1993), only the diffusion perpendicular to the propagating laser is made responsible for fluorescence fluctuations and photobleaching appears as a reduction of the apparent diffusional time τ_d . The contrast C in equation 2.1 is the amplitude for the fast

decaying part of the autocorrelation curves with k as the rate constant for the fluorescence fluctuations. Its decay constant reflects the time scale upon which typical on-off transitions take place. C is of importance in discussing photostability as it can be related to the fraction of molecules in a dark state $[D]$, according to equation 2.2 (Jung et al., 2006).

$$\frac{[D]}{1-[D]} = C \rightarrow [D] = \frac{C}{1+C} \quad (2.2)$$

The larger the $[D]$, less the time the molecules can spend in a chromophore state where they can be excited and possibly undergo photodestruction. The bright fraction $[B]$ is related to $[D]$, $[B] = 1 - [D]$.

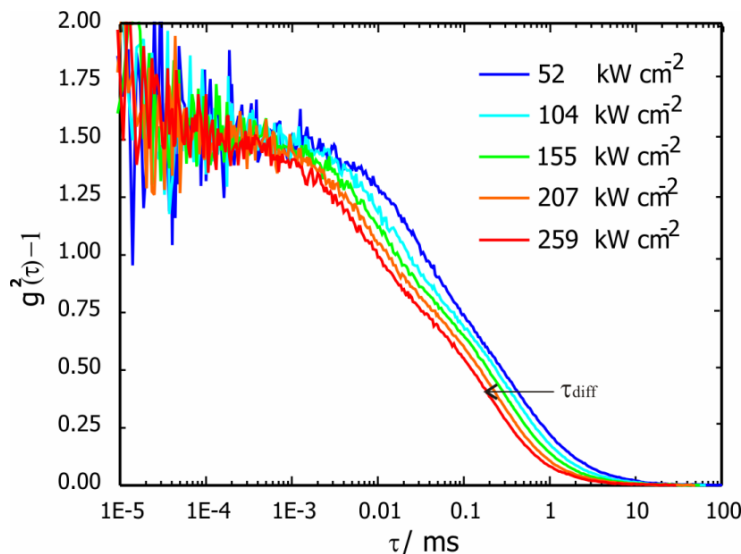


Figure 2.1: Intensity dependent fluorescence correlation curves for EYFP at pH 10 ($\lambda_{exc} = 488$ nm). Different excitation intensities are shown in the graph with corresponding colors. A strong reduction in apparent diffusion time upon increasing excitation intensity is observed. For better comparability, all FCS data are normalised.

2.2.2 Analysis of the photostability

A reduction of τ_d is a hallmark of ongoing photobleaching while molecules diffuse through the detection volume (figure 2.4). Several attempts were made to allow for this experimental observation (Eggeling et al., 2005; Widengren et al., 2007); formal splitting of the entity of fluorescent molecules into two fractions, one part corresponding to surviving molecules and the other part to bleached molecules, became most widespread, although recent results

indicate some arbitrariness in this model (Satsoura et al., 2007). The model which we apply here is based on the idea that interruption of a molecule's fluorescence emission can be due to photobleaching or leaving the detection volume. Both processes are treated as competing pathways following ordinary chemical kinetics with k_{bl}^{eff} as the effective (intensity dependent) rate constant for photobleaching and $1/\tau_0$ as "intrinsic rate constant" for diffusion. The measured intensity dependent τ_d is therefore composed of both contributions in equation 2.3.

$$\frac{1}{\tau_d} = \frac{1}{\tau_0} + k_{bl}^{eff} \quad (2.3)$$

In the simplest approach, k_{bl}^{eff} is proportional to the number of excitation cycles, k_{12} (equation 2.4).

$$k_{bl}^{eff} = \phi_{bl} \cdot k_{12} = \phi_{bl} \cdot \sigma \cdot \left(\frac{I}{h\nu} \right) = \sigma_{bl} \cdot \left(\frac{I}{h\nu} \right) \quad (2.4)$$

The proportionality constant is the quantum yield of photobleaching Φ_{bl} . k_{12} is composed of the excitation intensity I , the photon energy $h\nu$ and the absorption cross section σ . The bleaching cross section σ_{bl} is the product of Φ_{bl} and σ .

The situation is comparable to fluorescence quenching, where the nonradiative decay of an excited state is promoted by collisions with the quencher. Experimentally, this can be detected by a reduction of the fluorescence lifetime. It is therefore straightforward to analyse the (fluorescence) survival time in a similar manner in which the "photon concentration", $c_{photons}$ is treated as the quencher concentration in fluorescence quenching. The unusual expression "photon concentration" is the number of photons per area and time. It is equal to the intensity I divided by the photon energy $h\nu$ and is therefore related to k_{12} . The analysis is performed in a Stern-Volmer-like plot (equation 2.5, see figure 2.5).

$$\frac{\tau_0}{\tau_d(I)} = 1 + \frac{\sigma_{bl} \cdot \tau_0}{h\nu} \cdot I = 1 + \sigma_{bl} \cdot \tau_0 \cdot c_{photons} \quad (2.5)$$

The intrinsic diffusional time τ_0 can be computed phenomenologically by extracting the amplitude of the decaying exponential function of $\tau_d(I)$ (figure 2.4). From the slope of $\tau_0/\tau_d(I)$

versus the intensity I (figure 2.5), the bleaching cross section σ_{bl} divided by the photon energy $h\nu$, is obtained by the subsequent division with τ_0 (figure 2.6). τ_0 is used here for the sake of clearness and to stress the similarity of the analytical approach to fluorescence quenching.

2.3 Results and Discussion

2.3.1 Spectral characteristics

Spectra were recorded at pH 10, where the FCS experiments were performed. Excitation and emission maxima of (2-F) Tyr proteins were blue shifted compared to both the parent proteins and the (3-F) Tyr-EYFP (figure 2.2 and 2.3).

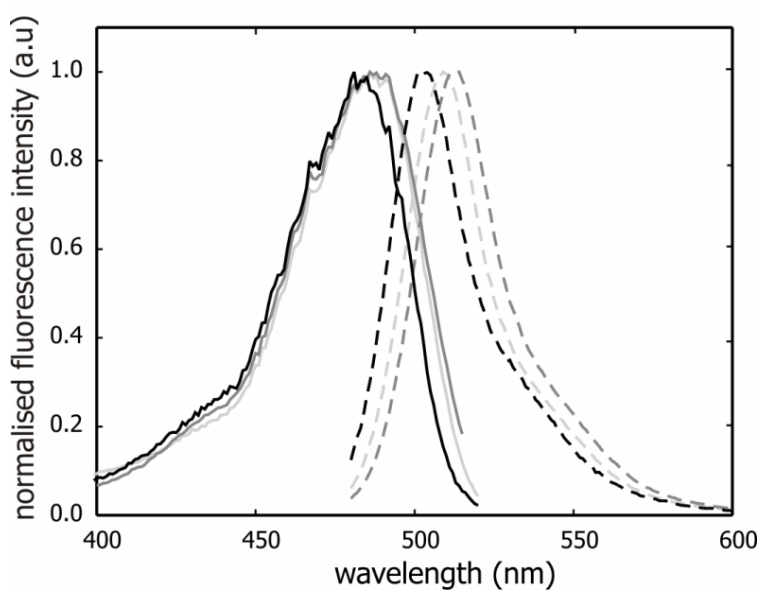


Figure 2.2: Normalised fluorescence excitation (full line) and emission (broken line) spectra of GFP variants at pH 10. EGFP is printed in light grey and (3-F) Tyr-EGFP and (2-F) Tyr-EGFP are printed in grey and black respectively.

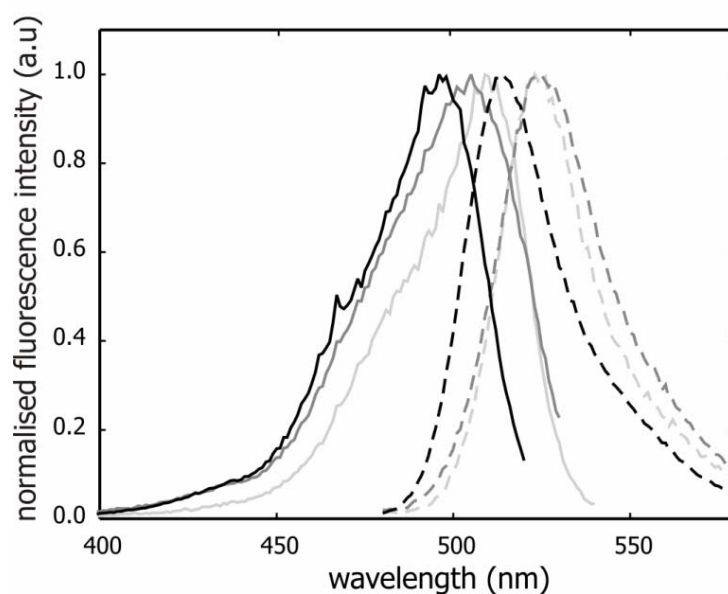


Figure 2.3: Normalised fluorescence excitation (full line) and emission (broken line) spectra of YFP variants at pH 10. EYFP is printed in light grey and (3-F) Tyr-EYFP and (2-F) Tyr-EYFP are printed in grey and black respectively.

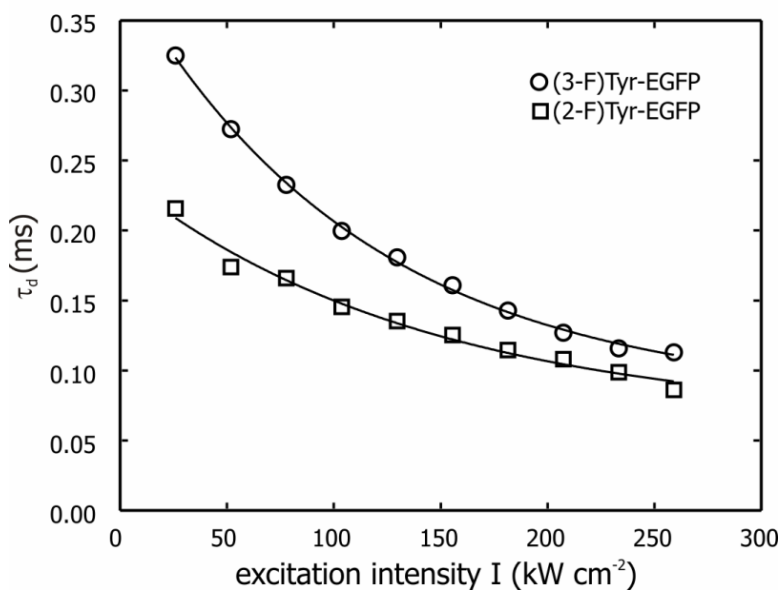


Figure 2.4: Intensity dependent τ_d of (3-F) Tyr-EGFP (\circ) and (2-F) Tyr-EGFP (\square), ($\lambda_{exc} = 488 \text{ nm}$) with phenomenological fitting for the determination of $\tau_{d,0}$. A strong decay of τ_d with increasing excitation intensity indicates photobleaching, but seems to level off at high intensities.

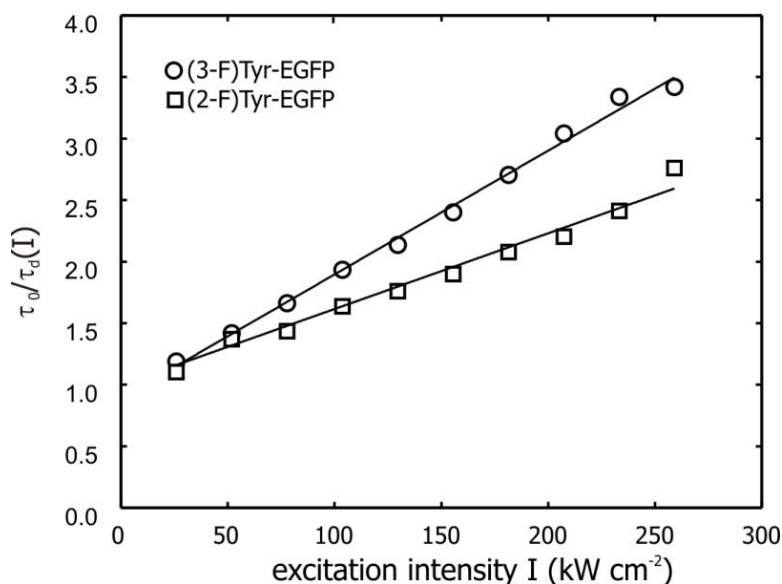


Figure 2.5: Linear plot of $\tau_0 / \tau_d(I)$ vs. Intensity I of (3-F) Tyr-EGFP (○) and (2-F) Tyr-EGFP (□). Photobleaching kinetics can be analysed in a ‘Stern-Volmer’ like plot. The slope of the fitting line is proportional to the rate constant of photobleaching.

Table 2.1: Spectral data for EGFP, EYFP and their variants.

Protein	Tsien, 1998	Pal et al, 2005 (pH 7)		This work (pH 10)		
	$\epsilon_M(\lambda_{max})$	$\epsilon_M(\lambda_{max})$	λ_{exc}	λ_{em}	λ_{exc}	λ_{em}
EGFP	55000-57000	34340	488	510	486	509
(2-F) Tyr-EGFP		22190	482	504	481	501
(3-F) Tyr-EGFP		30200	485	514	486	512
EYFP	83400	48770	514	527	509	523
(2-F) Tyr-EYFP		55460	504	520	496	514
(3-F) Tyr-EYFP		48790	518	533	505	524

Molar extinction coefficient (ϵ_M) is expressed in $M^{-1}cm^{-1}$. Fluorescence excitation (λ_{exc}) and emission (λ_{em}) values are in nanometers.

Agreement between our data and previously published values were found for all EGFPs (Table 2.1). Differences in the fluorescence emission maxima and excitation maxima were noticed for the red-shifted EYFPs. These differences might results from a partial deprotonation of Tyr203, (2-F) Tyr203 and (3-F) Tyr203 at the pH-value of our study, which is above the pK_A of these amino acids (Brooks et al., 1998). Such altered π - π interactions

might result in a weakened red-shift of the spectra at pH 10 compared to the values at pH 7. Changes might also be due to the presence of multiple protonation sites which is recently described (Bizzarri et al., 2007). Relevant for our work, however, is that the relative excitation cross section $\sigma_{\text{exc}}^{\text{rel}}$ at $\lambda = 488$ nm, related to the excitation maximum, is nearly constant for all GFPs. $\sigma_{\text{exc}}^{\text{rel}}$ are lower for the YFPs due to their red shifted excitation maxima. The reason why we use the dimensionless $\sigma_{\text{exc}}^{\text{rel}}$ instead of σ (in units of $\text{\AA}^2 = 10^{-16} \text{ cm}^2$) is that no reliable values for σ of single fluorescent proteins exist. All published extinction coefficients (see table 2.1) suffer from the fact that incomplete chromophore formation results in spectroscopically silent absorbance in the visible range whereas the protein absorption at $\lambda = 280$ nm, which is used as reference, is not affected. Despite this uncertainty, most published data match with excitation cross sections which are larger for YFP than for GFP by about 50% (Blab et al., 2001).

2.3.2 Photostability determination

Several photobleaching pathways of highly fluorescent molecules are discussed, among which one-electron photooxidation and photooxygenation are most prominent (Song et al., 1995). In the case of the autofluorescent proteins, the situation is more complex as the chromophore is shielded by the protein barrel. Recent results, however, indicate that oxygen can easily access the chromophore (Jimenez-Banzo et al., 2008). The existence of long-living dark states and an electron transfer reactions leading to photoconversion further complicate the photochemistry of this protein class (Jung et al., 2005; van Thor et al., 2002). Chemical modifications for studying these mechanisms became possible by implementing unnatural amino acids which resulted in chromophore fluorination (Bae et al., 2004; Pal et al., 2005). Previously, fluorotyrosines were used to unravel reactions which involve radicals (Seyedsayamdost et al., 2006). The kinetics of electron transfer processes were altered due to the change of the redox potentials upon fluorination with respect to the natural counterpart. (3-F) Tyr, which also finds application here, roughly reduced the kinetics of the investigated electron transfer reaction by a factor of 3. Although experimental data on the redox potentials of the chromophore and its fluorinated derivatives are not available to our knowledge, at least a qualitative change of the photostability is expected upon chromophore fluorination when electron transfer reactions substantially contribute to the photobleaching of AFP.

In the investigated intensity range, all FCS curves could be fitted by equation 2.1. Even at moderate intensities, the contrast C is constant and independent of further intensity increase. Such behaviour indicates light-driven cis-trans isomerization (Schwille et al., 2000). This is also true for the fluorinated proteins in this study; however, the absolute values of C and accordingly $[B]$ differ (equation 2.2). The photostability of the different fluorescent proteins to our disposal were determined as described in section 2.2.2. All curves, as depicted in figure 2.5, exhibited a linear dependence on the applied intensity. This finding suggests that photobleaching manifests as a one-photon process. The bleaching cross section σ_{bl} is determined according to equation 2.5 by dividing the slope in figure 2.5 by τ_0 and multiplying the photon energy, $h\nu$.

Unexpectedly, the experimentally accessible bleaching cross section σ_{bl} of 5 out of 6 investigated fluorescent proteins lie in the same range (figure 2.6). Only (2-F)Tyr-EYFP exhibits a faster bleaching. However, corrections have to be performed before conclusions about the relative photostability can be drawn. The bleaching cross section σ_{bl} depends on the relative absorption cross section σ_{rel} as it matters whether the fluorophores are excited close to their maximum like the GFPs or in the blue wing of the absorption band like in the YFPs. The grey area in figure 2.6, shifted to higher values, accommodate for this. Not all proteins of one mutant are in a bright state but undergo isomerization into dark states. As in a previous study, we refer σ_{bl} to the bright fraction B which can be calculated by the contrast C (Jung et al., 2006) (figure 2.7). The more often the molecules reside in a dark state, the less likely it undergoes photodestruction. To account for this we divide $\sigma_{bl}/(h\nu \cdot \sigma_{exc}^{rel})$ by the bright fraction B (figure 2.8).

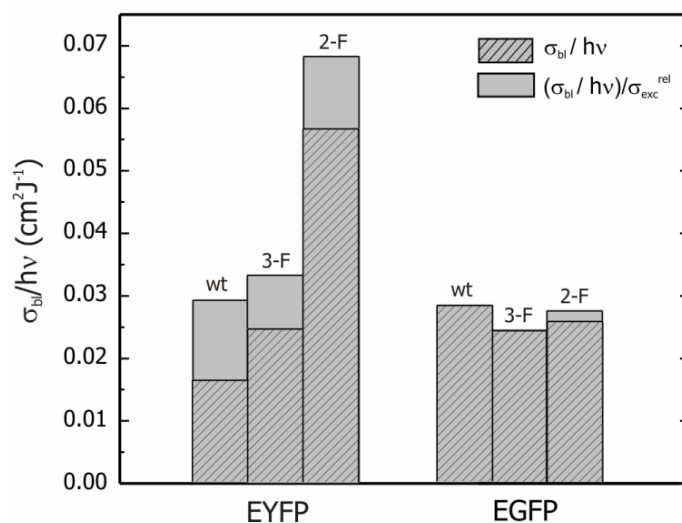


Figure 2.6: Photostability profile of investigated GFP and YFP variants. The bleaching cross section σ_{bl} (divided by the photon energy $h\nu$) are obtained from the linear fitting of figure 2.5 and division with $\tau_{d,0}$. $\sigma_{bl}/h\nu$ after correction with the relative excitation cross section σ_{exc}^{rel} is also shown in the graph.

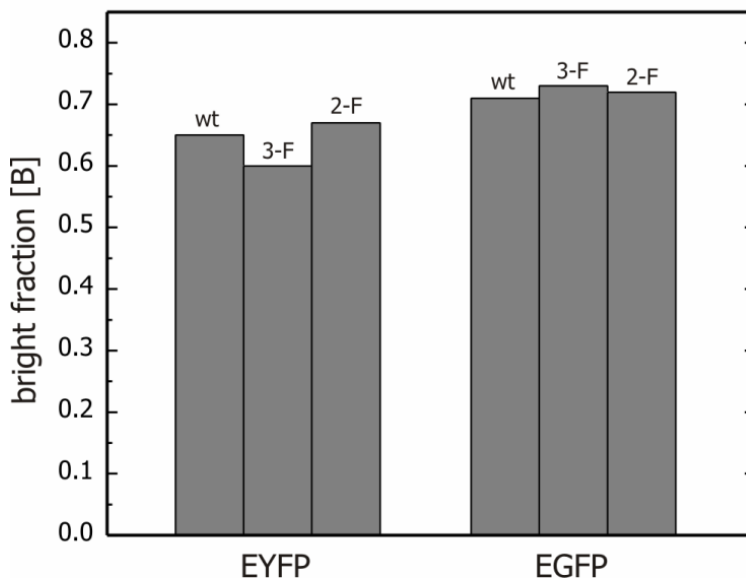


Figure 2.7: The bright fraction [B] of all the investigated mutants. It is calculated from the dark fraction [D]. The contrast C is a measure of the dark state population [D] under photostationary conditions.

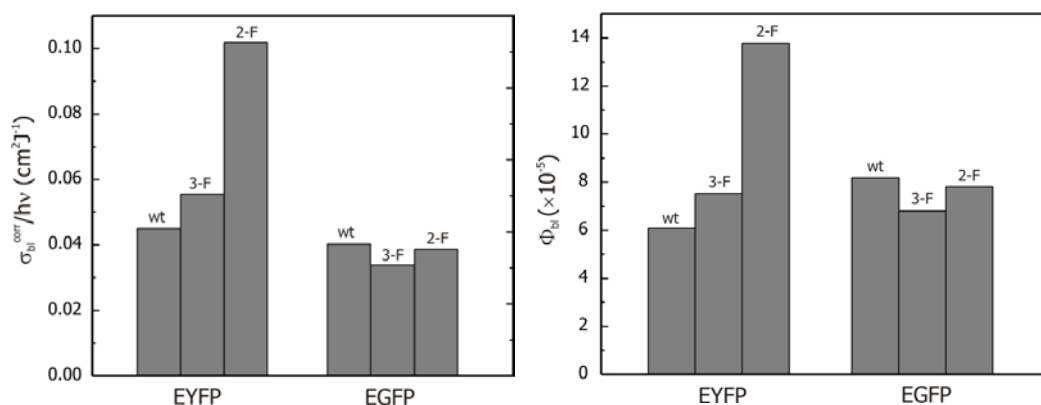


Figure 2.8: (left) Comparison of the different $\sigma_{bl}^{corr}/h\nu$ of EGFPs and EYFPs. $\sigma_{bl}^{corr}/h\nu$ is obtained by dividing $\sigma_{bl}/h\nu$ with relative excitation cross section σ_{exc}^{rel} and bright fraction [B].

Figure 2.9: (right) Quantum yield of photobleaching Φ_{bl} of all the analyzed mutants. Φ_{bl} is obtained by dividing σ_{bl}^{corr} by σ (2 Å² for EGFPs and 3 Å² for EYFPs are taken), see equation 2.4. Φ_{bl} of EGFP (8.2×10^{-5}) and EYFP (6.1×10^{-5}) are in agreement with the previously published results.

After these corrections, the situation is only slightly changed: all EGFPs have similar σ_{bl}^{corr} (within an estimated relative error of < 20% from repeated experiments on some mutants), but still lower σ_{bl}^{corr} than the YFP counterparts. However, in EGFPs the fluorination enhances photobleaching especially in (2-F) Tyr-EYFP. Interestingly, the pH-dependence of its absorbance spectra deviated from the other fluorinated proteins resulting in a pK_A close to the parent protein (Pal et al., 2005). This is noteworthy as the acidity of tyrosine is increased upon fluorination (Brooks et al., 1998). Facilitated access of protons to the chromophore might be the result of structural rearrangements which can also lead to a reduced shielding from molecular oxygen. The same might be true, however, to a lesser extent for (3-F) Tyr-EYFP. Our observations substantiate that some disturbances occur in the chromophore upon fluorination, the rate limiting step is probably not the putative electron transfer to molecular oxygen (Jimenez-Banzo et al., 2008).

2.3.3 Comparison to previously determined values

So far, the relative photostability among the different proteins was discussed and revealed that the bleaching cross section of the investigated EGFP variants is smaller in comparison with the EYFP variants. Assigning the commonly accepted values of σ (~ 2 Å² for EGFP and ~ 3

\AA^2 for EYFP) yields $\Phi_{bl} \sim 6.1 \times 10^{-5} - 8.2 \times 10^{-5}$ according to equation 2.4 for all proteins (Tsien, 1998) except (2-F) Tyr-EYFP (see figure 2.9). These values are only slightly higher than the reported values for EGFP and EYFP, measured by single-molecule fluorescence microscopy (Harms et al., 2001). Note that the fluorescence quantum yield for EYFP is higher than for EGFP making EYFP even more favourable for fluorescence applications (Jung et al., 2006). In addition, the photon detection probability is not uniform across the (inhomogeneous) excitation profile. It is, however, noteworthy that the saturation effects due to triplet population (Gregor et al., 2005) are likely not having impact on the photostability measurements of autofluorescent proteins since here both forward and backward transitions to dark states are light driven.

2.4 Conclusion

Reduced Φ_{bl} strongly suggests that EYFP has the highest photostability among the investigated mutants. In contrast to the stabilization effect of fluorination of fluorescent dyes (Sun et al., 1997), chromophore fluorination did not enhance the photostability advantageously. We assume that fluorination dislocates the protein folding or the molecular structure resulting in a reduced shielding and the formation of reactive oxygen species (Jimenez-Banzo et al., 2008). The absolute quantum yields for photostability, although similar to previously published values, should be interpreted with care as new analytical ways are yet to be developed for taking the detection nonlinearities in FCS into account.

Chapter 3

Comparative analysis of F64L containing GFP mutants and its influence on photostability by fluorescence correlation spectroscopy

3.1 Introduction

The two amino acid substitutions F64L and S65T are responsible for convenient use of EGFP in biological applications. The S65T and F64L mutations result a 35 fold increase in fluorescence over wt-GFP when excited at 488 nm and this proves that the second mutation is critical for the maximal fluorescence (Cormack et al., 1996). EYFP contains substitutions such as S65G, V68L, S72A and T203Y and is the most red shifted *av*GFP.

An improved version of YFP, Venus have been presented recently (Nagai et al., 2000). As a result of well known folding mutations, F64L/M153T/V163A/S175G, the folding of Venus is dramatically increased. Venus also contains a novel mutation F46L which greatly facilitated the maturation of YFP by accelerating the oxidation step of the chromophore formation. Oxidation of chromophore is considered to be a rate limiting step of maturation. Beyond that, the protein became more tolerant to acid-sensitivity and quenching by chloride ion (Nagai et al., 2000). In this aspect, we focus on F64L mutation which is an important constituent of EGFP that gives maximal fluorescence. So we introduced super-EYFP (SEYFP) in fluorescence correlation spectroscopy measurements together with EYFP and EGFP. SEYFP was created with the help of multiple site mutagenesis by the introduction of four folding mutations simultaneously into EYFP (EYFP - F64L/M153T/V163A/S175G) which facilitates the folding of YFP at 37⁰C (Nagai et al., 2000).

3.1.2 Changes in Venus

The following characteristics are observations by Rekas et al., (2002). The crystal structure of Venus shows an 11-strand β -barrel like that of other GFPs. When the β -barrel cross sections of Venus, wt-GFP and EYFP were compared, slight differences between the oval shapes of YFPs were observed. The residues surrounding the Venus chromophore were same as that found in EYFP. There are no significant changes between the chromophore and the residues (Thr62, Leu68, Gln69, Gln94, Arg96, Asn146, Arg168, Gln183, Tyr203 and Ser205) in Venus and EYFP. Electron density

study shows that the angle between the planes of the chromophore and Tyr203 in Venus is 11° which make the chromophore slightly more parallel than that of EYFP (the angle in EYFP is $11.5\text{-}12.3^{\circ}$). This small difference causes a minor change in the absorption spectrum of Venus relative to EYFP. The slightly more parallel orientation of the aromatic rings of Tyr66 and Tyr203 might also help to improve the $\pi\text{-}\pi$ interaction, reducing the excited state energy of the neutral chromophore. A shorter hydrogen bond between the chromophore phenolate and His148 is observed in Venus compared to that of EYFP. Distance between the chromophores in Venus dimer is less (by $\sim 2 \text{ \AA}$) than that of the wt-GFP and EYFP. A comparison of the dimer orientations are shown in figure 3.1.

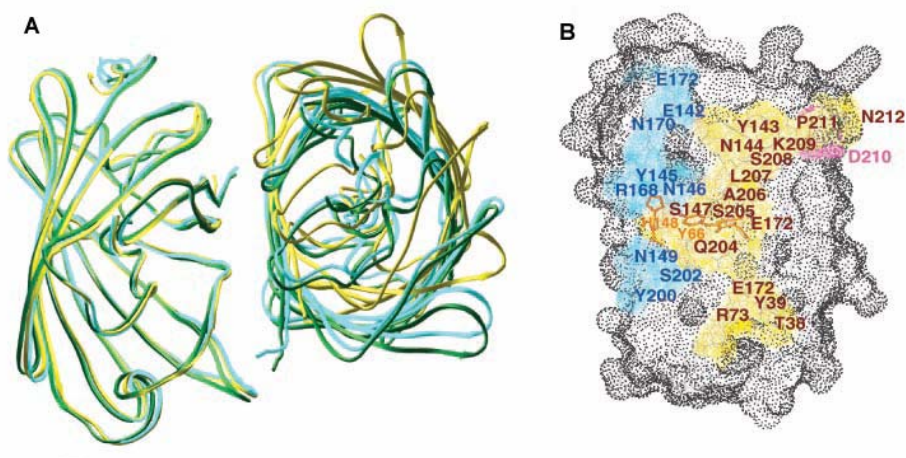


Figure 3.1: A) Ribbon diagram showing relative comparison of Venus (cyan), EYFP (yellow), and wt-GFP (green) dimer orientations. α -Carbons of residues 5-60 and 70-225 from one monomer of each protein are superimposed. B) Surface diagram generated by Insight II, showing differences in dimer interfaces of EYFP and Venus. Yellow, residues forming dimer contacts both in EYFP and Venus; cyan, residues forming dimer contacts only in Venus; pink, residues forming dimer contacts only in EYFP. The positions of the chromophore and His148 are indicated in orange (Adapted from Rekas et al., 2002).

Our aim is to find out whether the mutation F64L has any effect in the photodynamics of the autofluorescent proteins. For that we investigated 3 mutants EGFP, SEYFP and EYFP. We kept EYFP as a control in FCS study as it does not contain the F64L mutation. Excitation intensity dependent FCS measurements are done at $\lambda_{\text{exc}} = 488$

nm. Protein samples for FCS measurements and the experimental setup are discussed in 1.3.1 (chapter 1).

3.2 Analysis of FCS data

All FCS curves were fitted with equation 3.1 by means of commercial software (Origin Pro 7.5, Origin Lab, MA, USA).

A simplified two-dimensional form of autocorrelation function, which is applicable for the pinhole diameter of the experimental setup (Rigler et al., 1993) for freely diffusing molecules having diffusion time, τ_d is given by:

$$g^2(\tau) = 1 + \frac{1}{N} \left(\frac{1}{1 + \left(\frac{\tau}{\tau_d} \right)} \right) \left[1 + \frac{k_{23}^{eff}}{k_{31}} \cdot \exp\left(- (k_{23}^{eff} + k_{31})\tau\right) \right] \quad (3.1)$$

where N is the number of fluorescent molecules in the observation volume, k_{23}^{eff} is the effective intersystem crossing (ISC) rate constant and k_{31} is the rate constant comes from the deexcitation of the triplet state. The contrast C is the decay amplitude of the autocorrelation curves and is given by the ratio of k_{23}^{eff} and k_{31} in equation 3.1. C can be converted to the fraction of molecules in the dark states [D] under photostationary conditions (Jung and Zumbusch, 2006).

The ISC rate constant k_{23} is calculated from the equation 3.2 by using the rate constants of excitation k_{12} and deexcitation k_{21} of the singlet state which is given by (Widengren et al., 1994):

$$k_{23}^{eff} = k_{23} \cdot \frac{k_{12}}{k_{12} + k_{21}} \quad (3.2)$$

Considering the value of k_{12} which is having a minor role at low intensities in the denominator and applying $k_{12} = \sigma_{exc} \cdot I/h\nu$ in the numerator, the above equation takes

the form:

$$k_{23}^{eff} = \frac{k_{23} \cdot \sigma_{exc}}{k_{21} \cdot h\nu} \cdot I \quad (3.3)$$

where σ_{exc} is the absorption cross section of the bright state. In our studies, we plotted intensity dependent k_{23}^{eff} and k_{31} of all the three proteins. One can clearly learn from the plot that there is a strong linear dependency of both rate constants with I (figure 3.5 and figure 3.6), where the contrast is constant upon increasing with I which is typical for light driven cis-trans isomerisation of fluorescent proteins (Schwille et al., 2000). But this persistent contrast is not true in all cases, where one may need an additional rate constant to clarify this irregularity. In our case, we are in need of an additional term in the case of k_{31} , especially in figure 3.6. We called this correction term as thermal relaxation rate constant k_{31}^{therm} . So that the ‘real’ k_{31} , k_{31}^{eff} , will become the sum of k_{31}^{therm} and $k_{31}^{light\ driven}$ which can be written as:

$$k_{31}^{eff} = k_{31}^{therm} + \frac{k_{31} \cdot \sigma_{exc}'}{k_{21} \cdot h\nu} \cdot I \quad (3.4)$$

where σ_{exc}' is the absorption cross section of the dark fraction. A linear fit of the intensity dependent k_{31} will give the thermal relaxation rate constant which is believe to describe the dark state’s dynamics of the protein.

Intensity dependent FCS curves allow us to calculate the photobleaching kinetics of autofluorescent proteins. We focused our observation in evaluating the transition rates between bright states and dark states and rate constant of photobleaching. For determining the quantum yield of photobleaching ϕ_{bl} , we used a model ‘Stern-Volmer-like plot’ for analyzing the FCS data which is described recently (Veettil et al., 2008). Exponential decay fitting of figure 3.4, gives the intrinsic diffusion time τ_0 , which is used for describing a Stern-Volmer plot as shown in the inset of figure 3.4. Decreasing τ_d upon increasing excitation intensity is an indicative of photobleaching. In our

analysis, the photon concentration, c_{photons} is treated as quencher concentration in fluorescence quenching. As described in chapter 2,

$$\frac{\tau_0}{\tau_d(I)} = 1 + \frac{\sigma_{bl} \cdot \tau_0}{h\nu} \cdot I = 1 + \sigma_{bl} \cdot \tau_0 \cdot c_{\text{photons}} \quad (3.5)$$

where I is the excitation intensity, $h\nu$ is the photon energy and the bleaching cross section σ_{bl} is the product of quantum yield of photobleaching ϕ_{bl} and the absorption cross section σ . From the slope of the Stern-Volmer plot, ϕ_{bl} is obtained by several corrections with relative excitation cross section σ_{exc}^{rel} , photon energy $h\nu$ and bright fraction [B] etc (Veettil et al., 2008).

3.3 Results

As shown in the excitation intensity dependent correlation curves in figure 3.2, a distinct reduction of diffusion time is observed. The diminishing of τ_d is a typical character of all the investigated proteins over the whole range of excitation intensity which indicate a negligible flickering at pH 10 and 488 nm, even though a slight flickering is observed in EGFP (figure 3.2). The reduction of τ_d is slightly weaker for EGFP compared to EYFP and SEYFP at similar intensity range. In order to avoid complications due to external protonation, we used a higher pH for FCS measurements (Jung et al., 2001).

In the intensity range between 12 to 259 kW cm⁻², both YFPs showed a constant contrast (figure 3.3) that is characteristic of light driven cis-trans isomerization as explained before (Schwille et al., 2000). But EGFP exhibits an increasing contrast or dark fraction with excitation intensity which indicate a light-driven inter-conversion between the bright and dark state of the chromophore. The dark state population of EGFP (~30%) at higher intensity is different to that of the other two YFPs (~35%) by about only ~5%. This implies most of the EGFP molecules (~70%) are in the bright fraction [B].

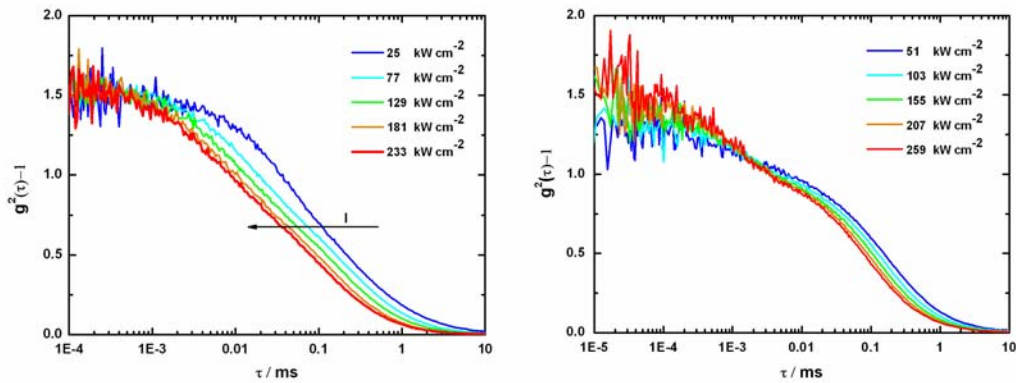


Figure 3.2: Intensity dependent fluorescence correlation curves for SEYFP (left) and EGFP (right) at pH 10. Normalized FCS curves of different excitation intensities are shown with corresponding colors. A strong reduction in the diffusion time is observed with increasing intensity.

FCS studies of some dyes reveal an intersystem crossing from an excited singlet state to the triplet state where an increasing dark fraction with excitation intensity is observed (Widengren et al., 1995).

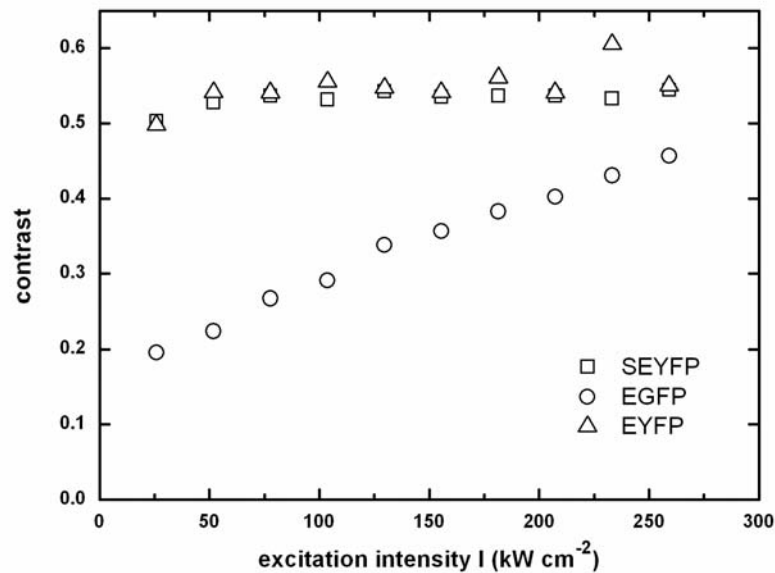


Figure 3.3: A plot of excitation intensity versus contrast of all the investigated proteins EGFP (O), EYFP (Δ) and SEYFP (\square). Both YFPs showed constant contrast upon intensity but EGFP differ. The dark fraction [D] and the bright fraction [B] are calculated from the contrast.

The transition rate constants between the bright state and dark state, i.e. the sum of k_{23} and k_{31} in equation 3.1 increases linearly with excitation intensity. This kind of flickering of yellow fluorescent proteins at low excitation intensity was observed previously (Schwille et al., 2000). We observed the same phenomenon even at higher intensities such as 250 kW cm^{-2} in the case YFPs.

The quantum yield of photobleaching is determined after dividing the slope of the Stern-Volmer plot (figure 3.4, inset) by σ_{exc}^{rel} (the value of EYFP is taken for SEYFP), $[B]$ and σ ($\sim 2 \text{ \AA}^2$ for EGFP and $\sim 3 \text{ \AA}^2$ for EYFPs) then after multiplied with $h\nu$. In our previous study, we obtained the ϕ_{bl} 8.2×10^{-5} and 6.1×10^{-5} for EGFP and EYFP respectively. Unexpectedly, ϕ_{bl} of SEYFP is found to be double the value of EYFP that is 12.3×10^{-5} . This is striking because the SEYFP holds novel folding mutations that may provide an increased environmental resistance. However, this protein has not yet undergone experimental conditions such as extreme laser conditions were used.

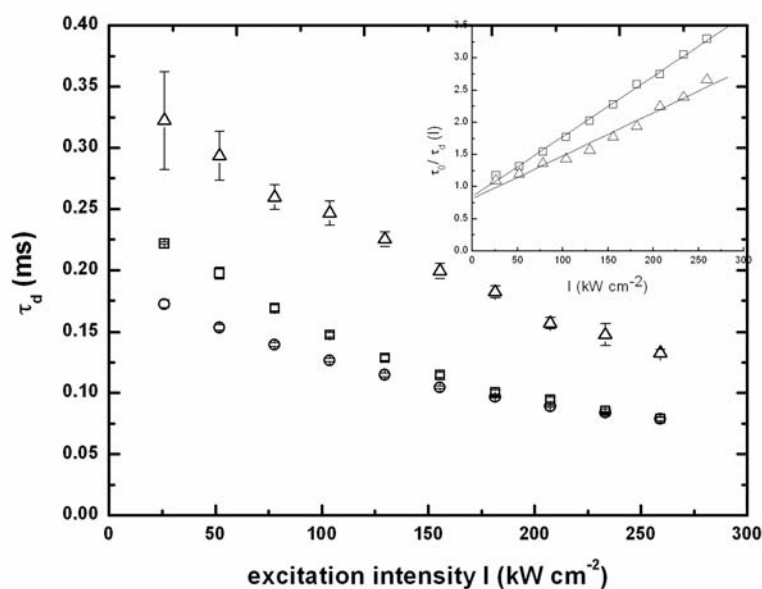


Figure 3.4: Reduction in diffusion time upon excitation intensity is a hallmark of the investigated proteins EGFP (O), EYFP (Δ) and SEYFP (\square). A ‘Stern-Volmer’ like plot of SEYFP and EYFP are shown in the inset from which the photobleaching kinetics can be analysed. A slope of the fitting line (see inset) gives the rate constant of photobleaching.

Next, we examined whether our photobleaching analysis correlates with the rate constants which were related to the triplet state. A similar plot for SEYFP and YFP were obtained when k_{23}^{eff} and k_{31} versus excitation intensity (figure 3.5) were plotted. In the case of k_{23}^{eff} all the plots extrapolate to zero besides EGFP (figure 3.6) shows a y-intercept. As a result, the slope of the k_{23}^{eff} versus I which is given by $k_{23} \cdot \sigma_{\text{exc}} / k_{21} \cdot h\nu$ according to equation 3.3 gives $0.24 \pm 0.01 \text{ cm}^{-2} \text{ kW}^{-1} \text{ ms}^{-1}$ (EYFP), $0.28 \pm 0.01 \text{ cm}^{-2} \text{ kW}^{-1} \text{ ms}^{-1}$ (SEYFP) and $0.92 \pm 0.03 \text{ cm}^{-2} \text{ kW}^{-1} \text{ ms}^{-1}$ (EGFP).

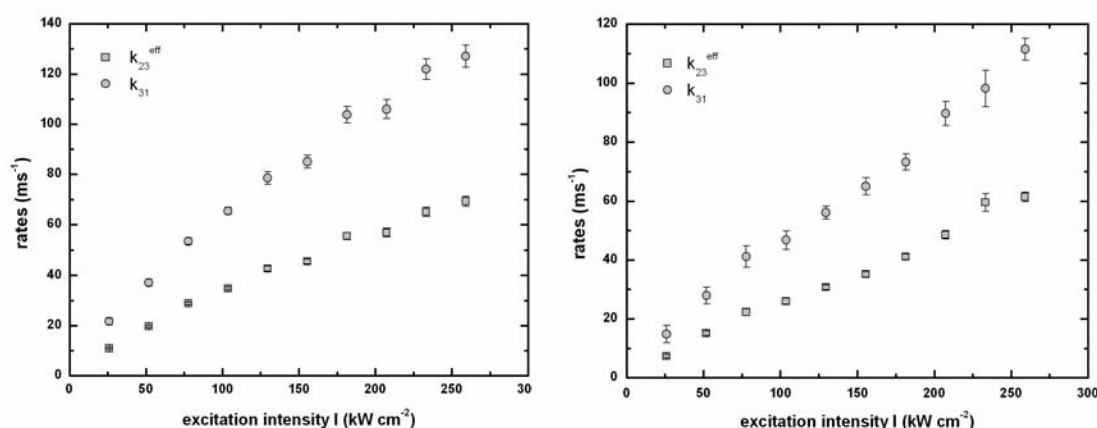


Figure 3.5: Dependence of k_{23}^{eff} and k_{31} with excitation intensity with error bars. SEYFP (left) and EYFP (right) exhibit a linear dependency on intensity. Slope of the line k_{31} is almost same for both YFPs, $0.42 \pm 0.01 \text{ cm}^{-2} \text{ kW}^{-1} \text{ ms}^{-1}$ (EYFP) and $0.45 \pm 0.02 \text{ cm}^{-2} \text{ kW}^{-1} \text{ ms}^{-1}$ (SEYFP).

3.3.1 Thermal relaxation rate constant

An interesting point in our studies is that, we are able to see an extra thermal relaxation component as mentioned in equation 3.4 (figure 3.6). This thermal component is not observed or it is negligible in EYFPs. The slopes of k_{31} versus I of both YFPs (see figure 3.5) are almost the same, i.e. $0.42 \pm 0.01 \text{ cm}^{-2} \text{ kW}^{-1} \text{ ms}^{-1}$ (EYFP) and $0.45 \pm 0.02 \text{ cm}^{-2} \text{ kW}^{-1} \text{ ms}^{-1}$ (SEYFP), however, EGFP (see figure 3.6) having more than double the value ($1.14 \pm 0.11 \text{ cm}^{-2} \text{ kW}^{-1} \text{ ms}^{-1}$). Interestingly, the thermal relaxation rate constant of EGFP is around 200 times higher ($224.88 \pm 18 \text{ ms}^{-1}$) than that of YFPs (from the intercept, see figure 3.6). A plot for thermal relaxation rate constant of other investigated GFP and YFP variants are shown in the figure 3.7. Among them, fluorinated counterparts of GFP show

slightly high thermal rate constant than the other mutants. The values are summarized in the table 3.1. This leads to a question that what will be the cause of such a thermal relaxation rate constant which is considered to be not induced by light or excitation intensity. We assume that this may be strictly in accordance with the chromophore environment and with an additional thermally activated relaxation channel. From the table 3.1, it can be learned that the thermal relaxation rate constant of EGFP decreases up on fluorination.

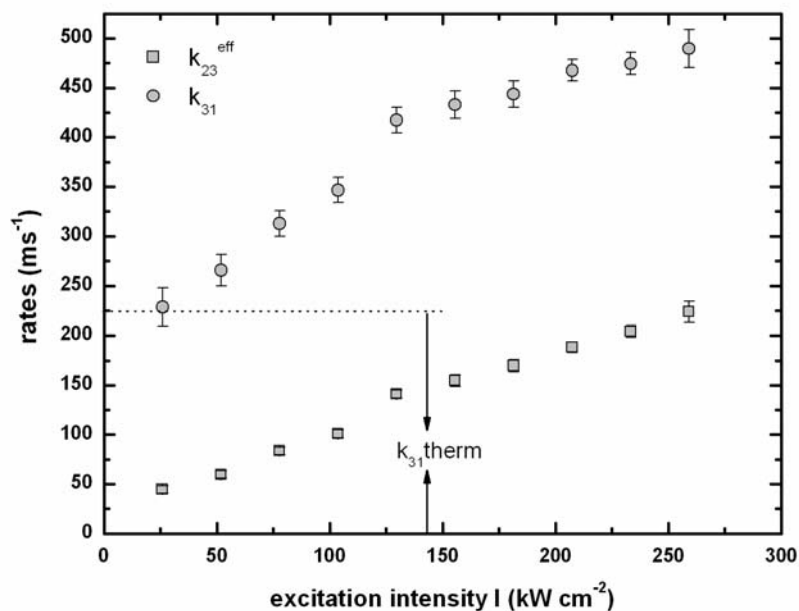


Figure 3.6: Rates (k_{23}^{eff} , k_{31}) of EGFP versus excitation intensity. The line k_{23}^{eff} extrapolates nearly through zero. Slope of the k_{31} line is double than that of YFPs ($1.14 \pm 0.11 \text{ cm}^{-2} \text{ kW}^{-1} \text{ ms}^{-1}$) which is accompanied by a thermal relaxation rate as shown in the graph.

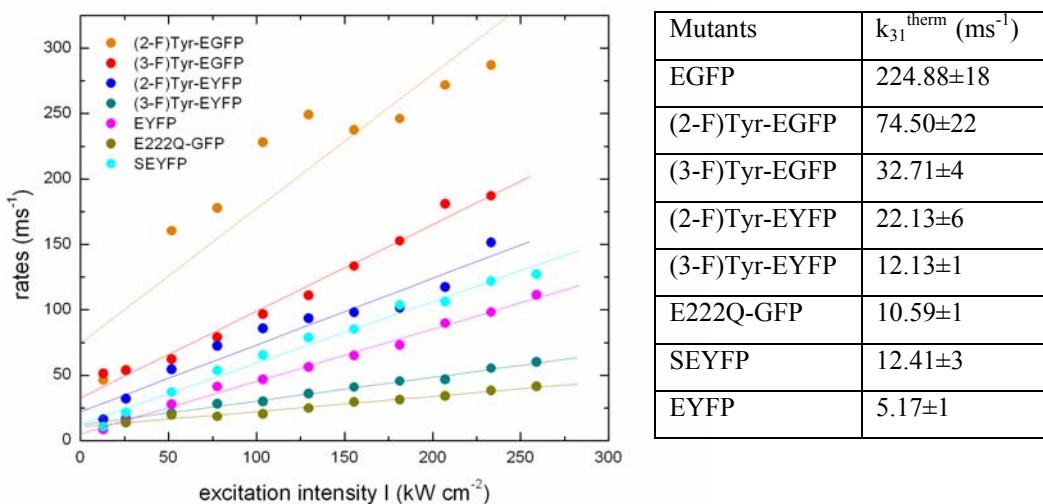


Figure 3.7) A plot of k_{31} of all the investigated GFP mutants versus I . Linear fitting is also shown in the figure. Table 3.1 summarizes the obtained values of k_{31}^{therm} of different GFP mutants.

A schematic representation for the interconversion between the bright state and the dark state is shown in the figure 3.8. S_0 and S_1 in the yellow shaded (bright state) area and grey shaded (dark state) area correspond to the ground state and excited state respectively. Excitation of the bright ground state ($S_0 \rightarrow S_1$) will lead to a high probability of fluorescence emission (green arrow in the figure) via $S_1 \rightarrow S_0$. The unprotonated excited state single exponential fluorescence decay indicates that $S_1 \rightarrow S_0$ transition in the dark state is nonradiative (Schwille et al., 2000). According to Schwille et al. (2000), the vanishing transition rates, as excitation intensity approaches to zero, suggest that the dynamics under study is excitation driven with a high transition barrier between the ground states of the bright and dark states. However, in our study such a disappearance of transition rates is shown in all cases except the k_{31} of EGFP. The dark state and bright state might be the different conformations of the chromophore.

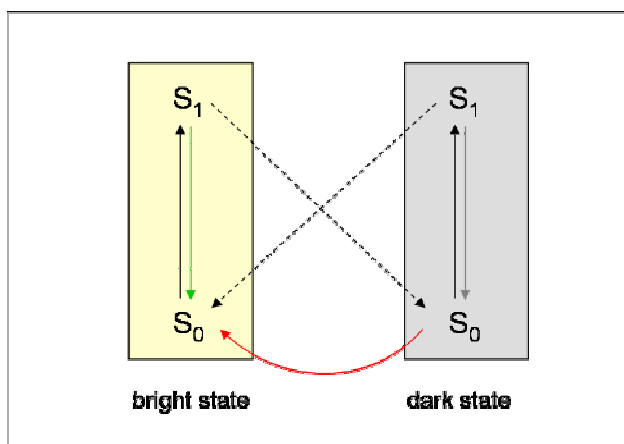


Figure 3.8: A representation of the potential scheme for the interconversion between bright and dark state. The red arrow represents the thermally activated bright state and dark state transition in our study. Yellow shaded area represents the bright state and the grey area represents the dark state.

3.4 Discussion

Photobleaching can be observed from the experimental autocorrelation curves where the translational diffusion decreases upon excitation intensity. The implementation of this strong intensity dependent photobleaching studies opens a quality analysis of the mutations. After all the corrections, we could observe a strong photobleaching behavior of SEYFP. This is not expected as this YFP contains several additional mutations which are favorable for biological applications (Nagai et al., 2000). What is the cause of this mutant's bleaching behavior and is it related to the folding mutations?

X-ray structure analysis of EGFP and E²GFP (T203Y-EGFP), which contains a F64L mutation, shows a shift in the position of the chromophore which is due to the above mutation (Nifosi and Tozzini, 2003). This mutation pulls the chromophore for accommodating the isopropyl group of Leu64 in the place of the phenyl of Phe64 which causes the movement of the surrounding residue for maintaining the hydrogen bond interactions with the chromophore. This can be accounted by the high photobleaching rate constant of SEYFP as it contains this mutation but lacking the S65T characteristics. We believe that some of the characteristics of the folding mutation may prevent the protein to show its photostability under high laser conditions.

Although crystal structure of SEYFP is not available, we take some of the enlightening points from the crystal structure data of Venus (Rekas et al., 2002) which contain only one additional mutation F46L to that of SEYFP which accelerates oxidation of the chromophore. Several local and global structural changes in Venus are due to the occurrence of F46L and F64L. F64L mutation induces structural change inside the β -barrel such as relocation of many β -strand residues at the dimer interface. Some β -bulge residues (Tyr145, Asn149, Arg168) participate in the dimer contacts with Venus and wt-GFP but they are solvent exposed in EYFP. Such results give a key to the influence of the intersubunit interface on chromophore environment which connects the dimerisation mechanism to the fluorescence property of GFP and its variants (Ward and Bokman, 1998).

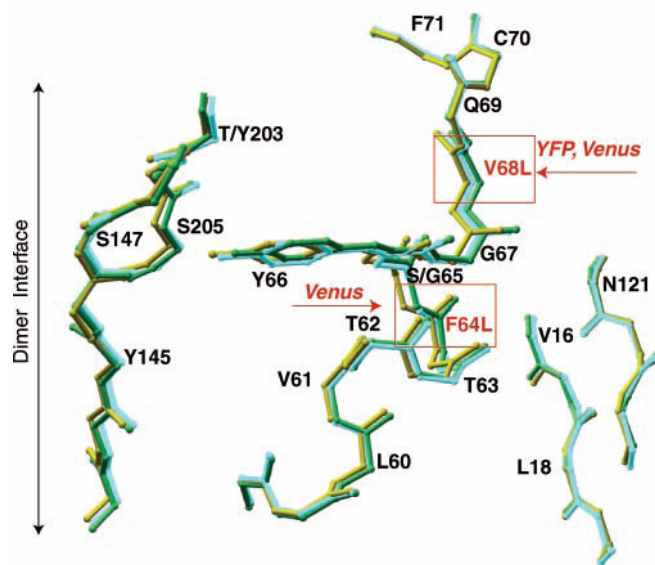


Figure 3.9: Ball and stick diagram showing the effect of F64L (Venus) and V68L (EYFP and Venus) mutations on the position of the chromophore and the central helix within the protein molecule. Backbone representation of the chromophore area in Venus (cyan), EYFP (yellow), and wt-GFP (green) is shown (Adapted from Rekas et al., 2002).

In EYFP, reorientation of the central helix and the chromophore toward the protein surface is caused by the V68L substitution (Ward and Bokman, 1998). But fortunately in Venus, the F64L mutation nullifies any change in orientation caused by V68L so that these changes remain close to their wild type positions (see figure 3.9). In this aspect, one

can speculate that this may be the situation in the case of SEYFP and the higher photobleaching of EGFP and SEYFP account for this. Among the folding mutations, there is no difference in the orientation of the side chains of the residues 153 and 163 were observed in Venus and EYFP. However, the S175G mutation causes 180° rotation of carboxyl side chain of Asp173 resulting a complete exposure to the solvent. At this point it is difficult to interpret such changes in accordance with the photostability data.

During photostability studies, we observed an interesting term called thermal relaxation rate constant with EGFP. From the figure 3.3, it can be learned that both YFPs exhibit light driven cis-trans isomerisation but EGFP shows a divergent behavior.

A linear increase of the relaxation rates with the excitation intensity reveals the photo - induced back and forth transition from the fluorescent state to the non-fluorescent state (dark state). This has been observed in the case of cyanine dyes where the photo-induced isomerisation between cis and trans forms of conjugated hydrocarbon chain of the cyanine dyes (Widengren and Schwille, 2000). A triplet like relaxation is a characteristic of EGFP (figure 3.2), even though it is not as prominent as in rhodamine or fluorescein dyes and the light driven relaxation rate is accompanied by the thermal relaxation component. It has been the same observation which was done previously and this low or triplet like population results from the low intersystem crossing (Widengren et al., 1999). Low triplet state formation and singlet state photosensitization in EGFP was reported earlier (Jimenez-Banzo et al., 2008). This major difference from the other two mutants suggests that mutations in the chromophore bearing residues can introduce considerable difference in the photophysical characteristics of the GFP. It might be that the hydroxyl group of Threonine in EGFP plays an important role in photophysical properties than the Glycine at the position 65 of the EYFPs. The hydrophobic character in the 65th position can add up several local conformational dynamics of the protein, nevertheless the chromophore is still shielded to avoid photobleaching.

Moreover, the prominent mutation T203Y in YFPs, destabilizes the anion because it lacks the hydroxyl group which is a hydrogen bond donor to the phenolate of the chromophore. Simulation studies shows that the hydrogen bond close to the Tyr145 is not stable and involves a distortion of chromophore planarity (Nifosi and Tozzini, 2003). The

Tyr203 mutation is absent in EGFP and this makes a difference compared to YFPs in our study. Thr203 makes a hydrogen bond to the chromophore of the B states of the EGFP but not in E²GFP (Nifosi and Tozzini, 2003) and this may be the same situation for YFPs. This absence has a relevant role in the absorption energy. Suitable mutations of GFP at positions 203 and 222 can be used to selectively influence the potential energy surface of its chromophore states (Wiehler et al., 2003). We assume that the thermal relaxation component in EGFP is an additional reversible process that can be observed in the exponential part of the FCS curve. From the other mutant's photostability data, it is also interesting to note that this relaxation is not altering the photostability of the protein.

3.5 Conclusion

Intensity dependent FCS analysis opens up a way to characterize the autofluorescent proteins for biological applications. In comparison with the EYFP and EGFP, the most pronounced character of the SEYFP is the increased photobleaching with a quantum yield of bleaching 12.3×10^{-5} which is double the value of EYFP and EGFP. This may reduce the applications of SEYFP and related mutants in single molecule applications. We believe that the structural changes inside the β -barrel induced by the F64L mutation are responsible for the increased photobleaching. Extremely high thermal relaxation rate constant ($224.88 \pm 18 \text{ ms}^{-1}$) of EGFP at higher intensity is another remarkable point of discussion in our study.

Chapter 4

Wavelength dependent FCS measurements of Tyr203 and Gln222 containing GFP mutants

4.1 Introduction

Tsien (1998) classified the known GFP variants based on distinct components of their chromophores. Yellow fluorescent proteins are under the category named class 4, where the phenolate anion is stacked with a π -electron system. A mutation to an aromatic ring close to the chromophore results proteins having longest wavelength. The replacement of Thr203 to tyrosine and the replacement of Ser65 to glycine or threonine will cause the ionization of the chromophore. Mutation of Thr203 to aromatic residues like histidine, tyrosine, tryptophan lower the excited state of the adjacent chromophore due to the additional polarizability of their π systems (Ormö et al., 1996). This mutation results an increase in the excitation and emission wavelength by up to 20 nm. The most dramatic red shift was shown by the mutation T203Y/S65G/V68L/S72A (EYFP) with an emission maximum of 527 nm, an extinction coefficient of $83400 \text{ M}^{-1} \text{ cm}^{-1}$ and a quantum yield (0.63) which is higher than that of S65T. Mutations other than T203Y have shown to improve the brightness of YFP in live cells (Cormack et al., 1996).

The crystal structure of EYFP had been reported (Wachter et al., 1998). An interesting feature of the phenolic tail of the chromophore is that it is connected to the bulk solvent through hydrogen bonding and therefore not tightly embedded in the protein like that of wild-type GFP and S65T mutants. Extended π systems due to Tyr203 can easily respond to any change in the chromophore polarity by shifting the π electron cloud and with a larger dipole moment. If the excited state has a larger dipole moment than the ground state, a spectral shift to longer wavelength is observed (Creed, 1984). The chromophore of the mutant is entirely planar which is consistent with all the other GFP structures (Wachter et al., 1998). Also a main difference in hydrogen bond between EYFP and S65T is the hydrogen bond between Glu222 and the heterocyclic ring nitrogen, suggesting a neutral chromophore ring nitrogen.

In this study, fluorescent proteins with mutations S65G/T203Y/E222Q (T203YE222Q) and S65G/V68L/S72A/T203Y (EYFP) were used for investigating the photophysics of GFPs under different λ_{exc} .

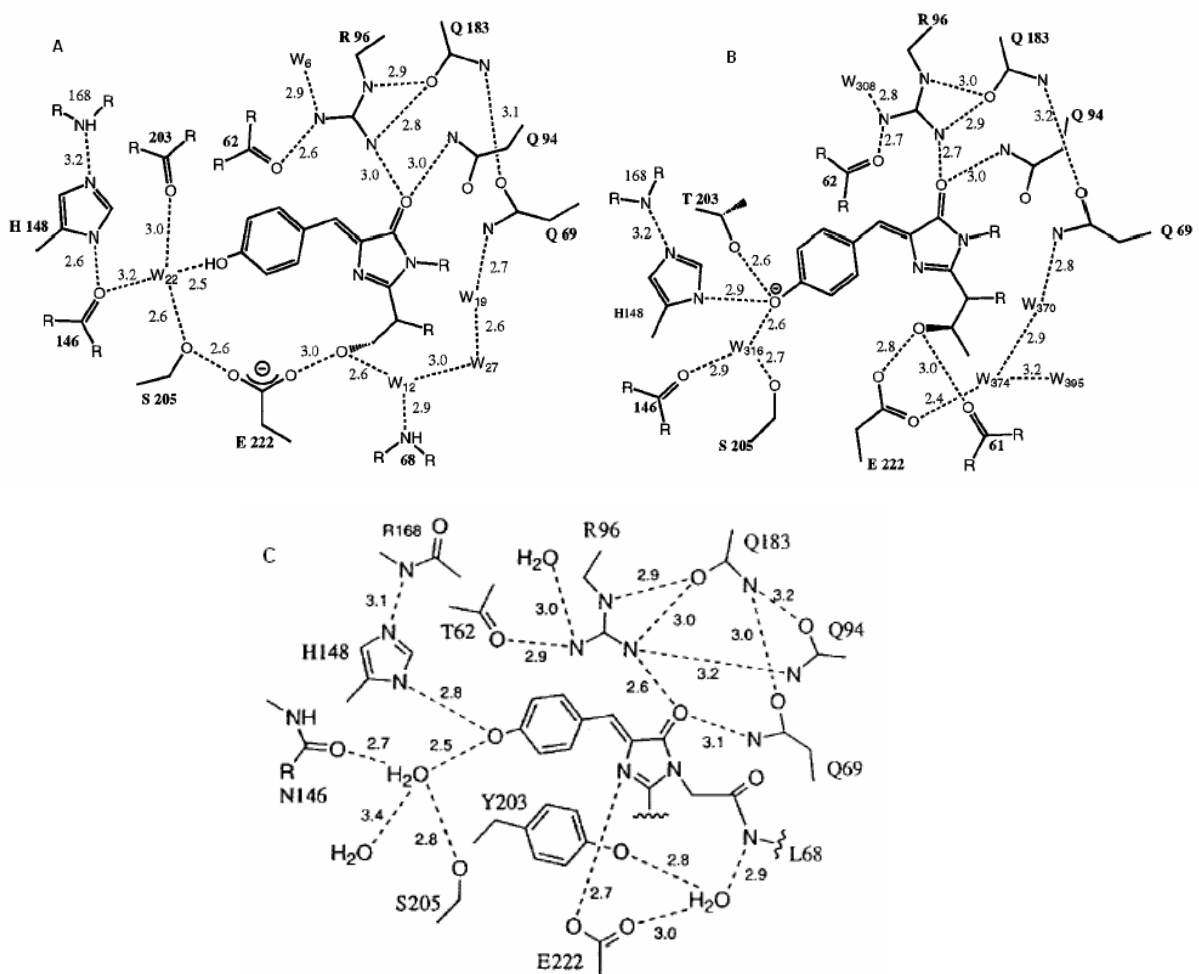


Figure 4.1: Schematic diagram of the interactions between the chromophore and the surrounding residues and water molecules in (A) wt-GFP, (B) S65T mutant and (C) EYFP. Hydrogen bonds are shown as dashed lines and have the indicated lengths in Å. (Adapted from Brejc et al., 1997; and Wahter et al., 1998)

4.1.2 Characteristics of the amino acid at position Thr203 and Glu222

Some of the mutagenesis studies and the atomic model of GFP show that residues close to the chromophore are having substantial effects on the spectra. Thr203 and Glu222 are critical points of such mutation. For example, the mutations T203I and E222G have opposite effects on the absorption spectrum. Instead of showing 475 nm absorption peak which is attributed to the anionic chromophore, T203I shows only 395 nm absorption peak which reflects the neutral chromophore and is due to the obstruction of ionization of

the phenolic oxygen by Isoleucine (Ehrig et al., 1995). However, the mutation E222G arrest the 395 nm peak in favor of a peak at 470 to 490 nm and this is the same effect of replacement of Ser65 to glycine, alanine, cysteine, valine or threonine (Delagrave et al., 1995; Heim et al., 1995). Moreover the mutation E222G withdraws hydrogen bonding between Glu222 and Thr65.

The amino acids Ser65, Thr203, Glu222, His148 and Leu205 are essential for determining the photophysical behavior of GFPs. Introduction of Tyrosine at the position 203 is unable to make a hydrogen bond with the hydroxyl group of Tyr66 and there by destabilizes the deprotonated B state (Kummer et al., 2000; Wahter et al., 1998). Replacement of glutamic acid at position 222 reduces the acidity and destabilizes the neutral chromophore by shifting the equilibrium up to 14 kJ/mol towards the deprotonated chromophore form. For the stabilization of the neutral chromophore RH form at neutral pH, it is necessary to have an acidic group at position 222 with a hydrogen-bonding network to the position 66. Furthermore, the amino acid at position 66 is responsible for the conformation of amino acid at the position 222 so that it can participate in the hydrogen bonding network (Jung et al., 2005). On the other hand, hydrogen bonding between the amino acid at position 203 to the oxygen of Y66 determines the deprotonated form of the chromophore, B- or I- state nature.

4.3 Experimental setup and analysis method

All FCS curves were taken by using a home-built confocal setup based on an inverted microscope (Axiovert 200, Zeiss) and Ar-ion laser , operating at $\lambda_{exc}= 457\text{-}514$ nm (Innova I-304 C, Coherent) was coupled into an optical fibre and outcoupled by a 40x objective lens resulting in a parallel laser beam with a diameter of 0.8 mm. A detailed description of the experimental setup and samples were described in 1.3.1 (chapter 1). FCS curves were taken at different wavelengths ranging from 457 to 514 nm also at different excitation intensity under these wavelengths.

Wavelength dependent and intensity dependent FCS data were analysed according to the equation 3.1 (chapter 3) by using Origin Pro 7.5. From the above equation, k_{23}^{eff}

and k_{31} are taken and plotted versus excitation intensity which is shown in the figure 4.7. Derivation of k_{31}^{eff} and k_{23}^{eff} are according to 3.2 in chapter 3. k_{23}^{eff} and k_{31} versus excitation intensity I were plotted and fitted linearly. Taking the slope of both graphs and multiplying with $h\nu$ will give σ_{forward} and σ_{backward} respectively. So these parameters will take the form:

$$\sigma_{\text{forward}} = \frac{k_{23}}{k_{21}} \cdot \sigma_{\text{exc}} \quad (4.1)$$

$$\sigma_{\text{backward}} = \frac{k_{31}}{k_{21}} \cdot \sigma_{\text{exc}} \quad (4.2)$$

where k_{21} and σ_{exc} in the equation 4.1 and 4.2 are related to the bright state and dark state respectively. σ_{forward} is related to the rate constant of the transition from S_1 of bright state into the S_0 of dark state. On the other hand σ_{backward} is related to the transition from S_1 of dark state into the S_0 of the bright state. Such a potential scheme is shown in the figure 3.8.

4.4 Results and discussion

Fluorescence excitation and emission spectra of EYFP and T203YE222Q were taken at pH 10 and this is in accordance with the previous reports. Excitation and emission maxima were found at 509 nm and 523 nm for EYFP and 507 nm and 521 nm for T203YE222Q respectively. These are depicted in figure 4.2.

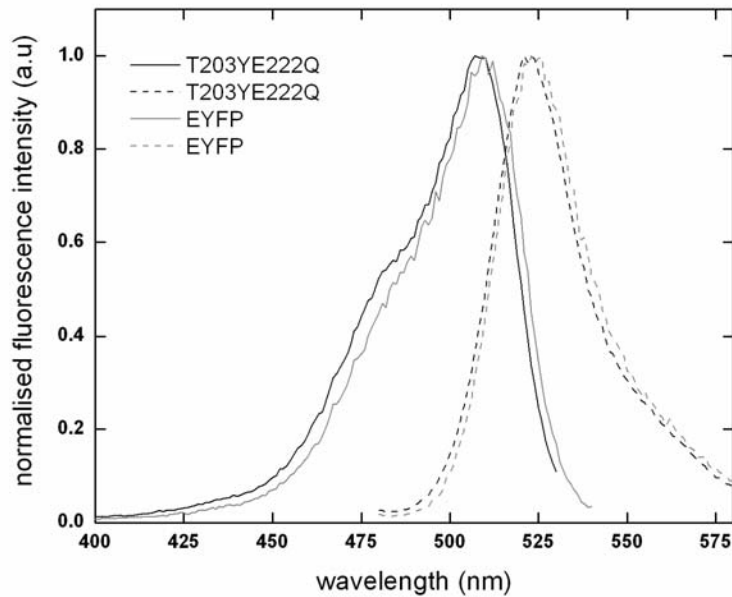


Figure 4.2: Fluorescence excitation and emission spectra of the investigated mutants T203YE222Q and EYFP. Solid line and dotted line corresponds to the excitation and emission spectra for T203YE222Q (black) and EYFP (grey).

Diffusion time decreases upon intensity in all investigated mutants and this is true in all the excitation wavelengths starting from 457 nm to 514 nm. However, reduction in diffusion time is strongest at wavelengths $\lambda_{exc} = 502$ nm and $\lambda_{exc} = 514$ nm which strictly obeys the absorption properties. This behavior can be seen in figure 4.3 and figure 4.4 where the decay of diffusion time is maximum at higher wavelength. According to the equation $k_{12} = \sigma_{exc} \cdot I/h\nu$, when λ_{exc} increases, the value of $h\nu$ becomes approximately same as that of I . The more distinct reduction of diffusion time is due to the higher σ_{exc} which means there will be more photocycles within the same lag time. Hence reduction of diffusion time up on increasing excitation wavelength is expected as seen in the figure 4.3 and 4.4. This also explains the accuracy of the wavelength dependent FCS measurements.

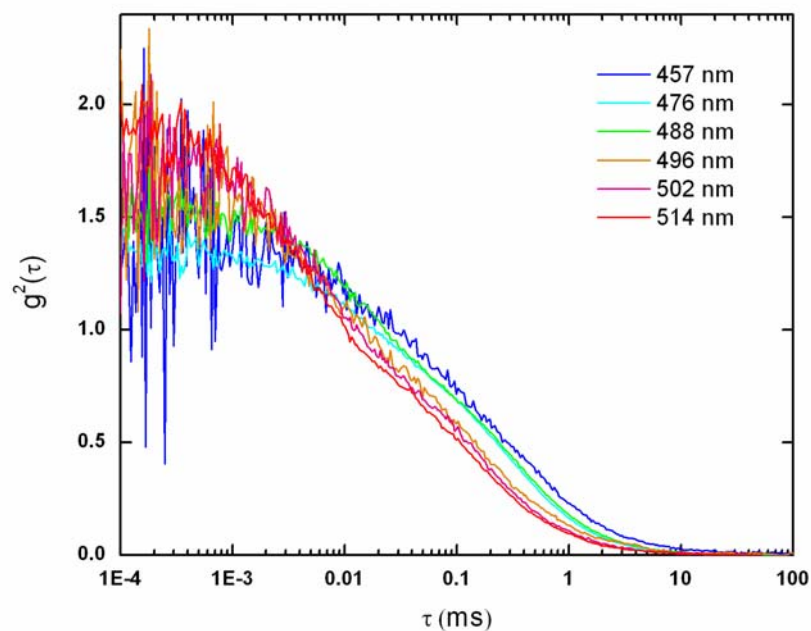


Figure 4.3: Normalized autocorrelation curves for EYFP. Reduction of diffusion time up on increasing excitation wavelength can be directly observed from the graph. All curves were taken at $400 \mu\text{W}$ laser power and were normalized to the number of fluorescent molecules.

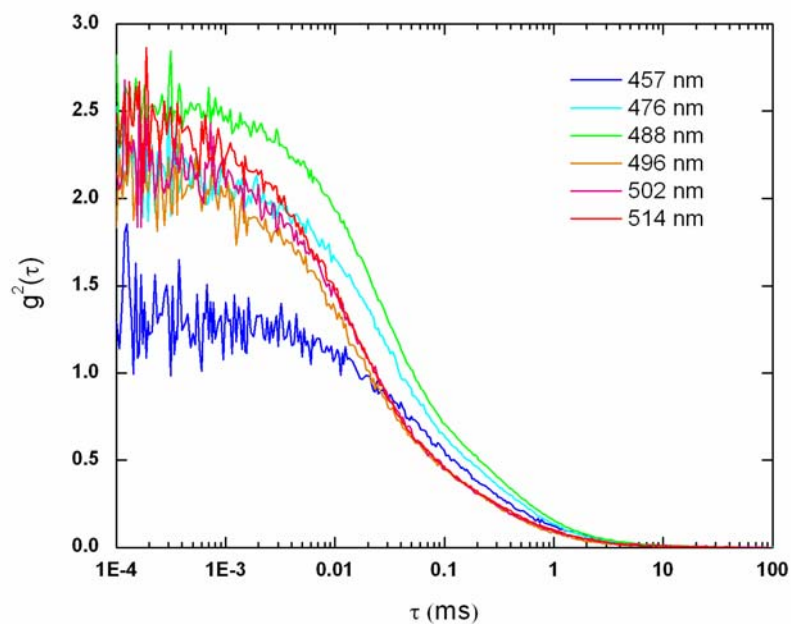


Figure 4.4: Autocorrelation curves for T203YE222Q mutant which were normalized to the number of fluorescent molecules. All curves were taken at $400 \mu\text{W}$ laser power.

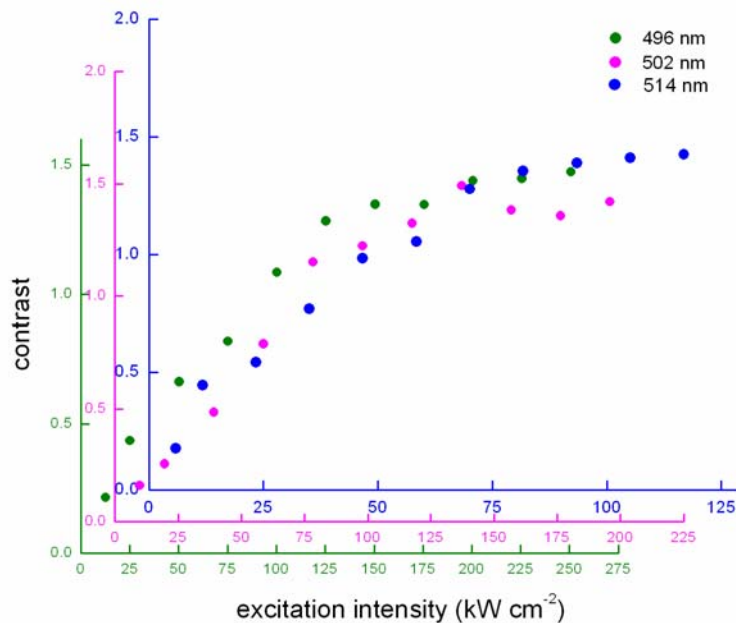


Figure 4.5: Saturating contrast observed by the mutant T203YE222Q at wavelengths 496, 502 and 514 nm are shown with corresponding colors. Different scale in x-axis is due to the different σ_{exc} .

In T203YE222Q mutant, a saturating contrast is observed in the excitation wavelength of 496-514 nm. At all other wavelengths, the mutants show the same behavior that is a constant contrast through out the whole intensity range (figure 4.6). Interestingly, an increasing contrast upon increasing intensity is observed at 457 nm with a thermal relaxation rate constant which might be attributed by the excitation of some other state of the protein which is still suspicious. An increasing contrast is an indicative of light driven inter conversion between bright and a dark states as observed previously (Schwille et al., 2000). Constant contrast is a measure of the light driven cis-trans isomerisation as explained before.

EYFP shows constant contrast in all wavelengths. Some of the plots are shown in the figure 4.6. Table 4.1 depicts the average values of contrast and dark fraction at different wavelengths of investigation. The dark fraction [D] linearly increases with the wavelength reaching 50% at 514 nm. However a slight deviation is observed at 476 nm. It has been shown that at high pH, yellow shifted GFP mutants and EGFP activates the

dark state with a quantum efficiency of $\sim 10^{-3}$. This average dark fraction is independent of excitation intensity and this suggests a coexisting activation of reverse transition from the dark state to the anionic bright state (Schwille et al., 2000). In our case, this average dark fraction is slightly dependent of wavelength of excitation and which is maximum at highest wavelength. Also there is an equilibrium between the dark state to the bright state is established at higher or at suitable wavelength.

Table 4.1: Contrast and dark fraction [D] of EYFP at different wavelengths.

λ (nm)	457	476	488	496	502	514
C	0.44	0.41	0.54	0.59	0.84	1.04
[D]	0.30	0.29	0.35	0.37	0.45	0.50

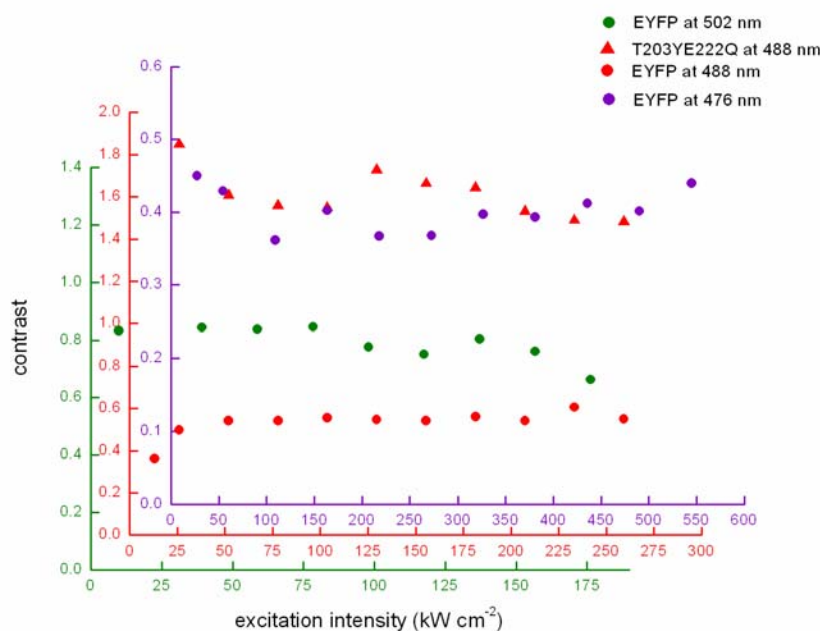


Figure 4.6: A plot of contrast versus excitation intensity. EYFP shows constant contrast irrespective of all excitation wavelengths.

After linear fitting of the plot using equation 3.3 (for k_{23}^{eff} vs. intensity plot) and equation 3.4 (for k_{31} vs. intensity plot) in figure 4.7 (only few plots are shown), the slopes

were extracted. The slopes were multiplied by $h\nu$ ($19.36 \times 10^{-17} / \lambda$) will give $\sigma_{forward}$ and $\sigma_{backward}$ respectively. This has been done for all proteins at different excitation wavelength. Values of $\sigma_{forward}$ and $\sigma_{backward}$ are plotted against the excitation spectrum of each mutant as shown in the figure 4.8 and 4.9. Most of the intensity dependent k_{31} plots are showing a y-intercept and that gives a thermal relaxation rate constant k_{31}^{therm} as explained in 3.4.1 (chapter 3). The value ($\sim 5 \text{ ms}^{-1}$ for EYFP) was negligible as this mutant shows a constant contrast in all wavelengths. As shown in the figure 4.5, saturating contrast is observed at higher wavelength for T203YE222Q mutant and the k_{31}^{therm} is $\sim 10 \text{ ms}^{-1}$.

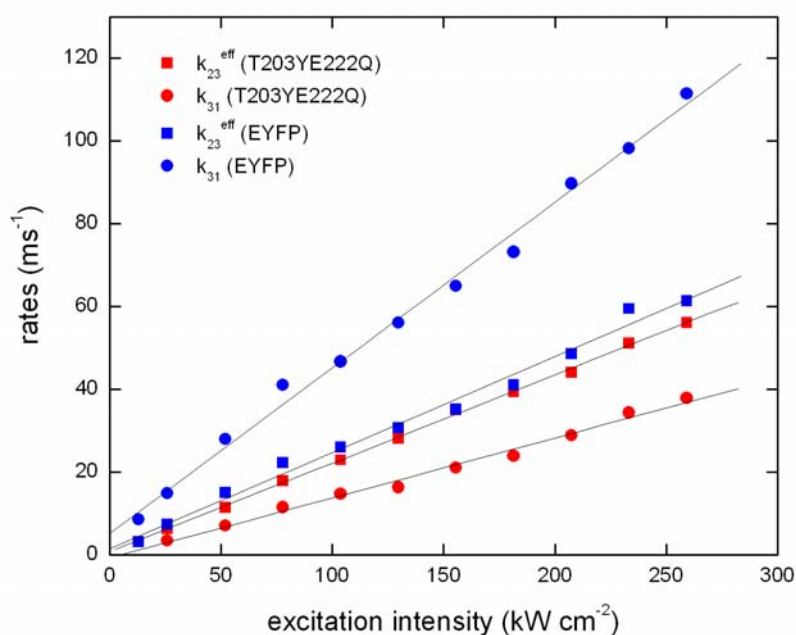


Figure 4.7: Plot of rate constants k_{23}^{eff} and k_{31} versus the excitation intensity at 488 nm. Slope of the linear fitting using the equation 3.3 and 3.4 will give $\sigma_{forward}$ and $\sigma_{backward}$.

Fluorescent pathway of bright state and dark state is sometimes accompanied by a thermal relaxation rate constant. In such a model, $\sigma_{backward}$ is related to the conversion of the excited nonfluorescent dark state to the ground bright state and $\sigma_{forward}$ is for the

excited bright state to the ground dark state. Both these process are light induced. Two-photon excitation action cross section values of commercially available fluorescent proteins were determined previously (Blab et al., 2001) and they found that two-photon absorption spectra are similar to that of one-photon absorption spectra. However, they exhibit a significant blue shift which is attributed from the vibrational mode of the two-photon absorption process. However, in our case the situation is more complicated as the effect of mutations has to be considered.

For the mutant T203YE222Q (see figure 4.9), it is obvious that the cross sections almost follow the excitation spectrum even though there is a negligible deviation is observed. However, the situation is different for the EYFP. As seen from the figure 4.8, there is a blue shifting ($\sigma_{backward}$) and red shifting ($\sigma_{forward}$) are observed.

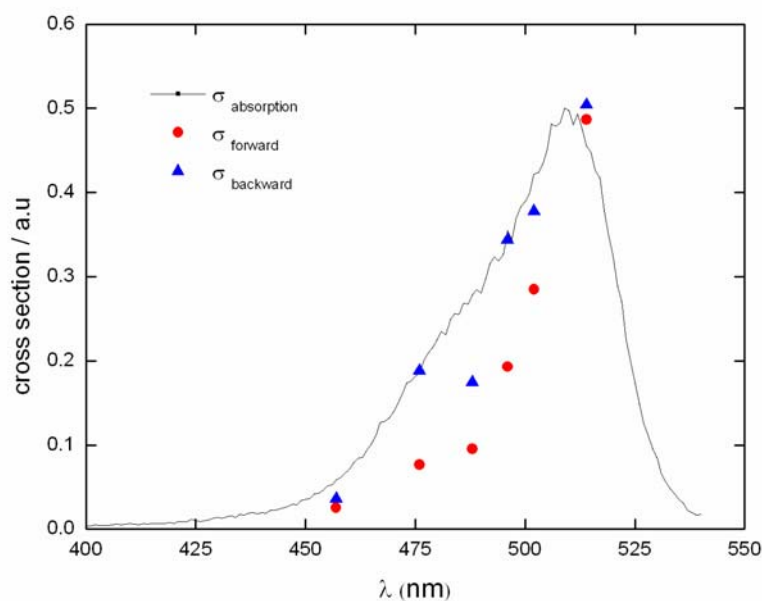


Figure 4.8: $\sigma_{forward}$ and $\sigma_{backward}$ of EYFP is plotted against excitation spectrum. Wavelength scale is shown in the x-axis.

We believe that this is due to the combination of two effects, one is attributed by the zwitterionic state and the other is due to the decarboxylation effect. Both these processes are described as follows.

The zwitterionic form of the chromophore (Brejc et al., 1997) is formed from the anionic form through a proton transfer from the nearby Glu222. The zwitterionic state is presumed to undergo radiationless decay through nonadiabatic crossing, through a rotational motion around two ring-bridging bonds in the chromophore, and will appear dark or weakly fluorescent (Weber et al., 1999). Also it has been suggested that the slow blinking (Dickson et al., 1997) might be due to the conversions between the anionic and the dark zwitterionic form (Weber et al., 1998). Such a reversible anionic-zwitterionic transformation may be favorable for the fast optically driven fluorescence flicker at high pH (Schwille et al., 2000). This state absorbs comparable wavelength to the anionic state. In figure 4.8, the $\sigma_{backward}$ follows the excitation spectrum of this dark state and might therefore be blue shifted. Such behavior might be due to the above mentioned characteristics of the zwitterionic state (dark) of the EYFP. $\sigma_{backward}$ is accompanied by the transfer of excited dark state to the ground bright state.

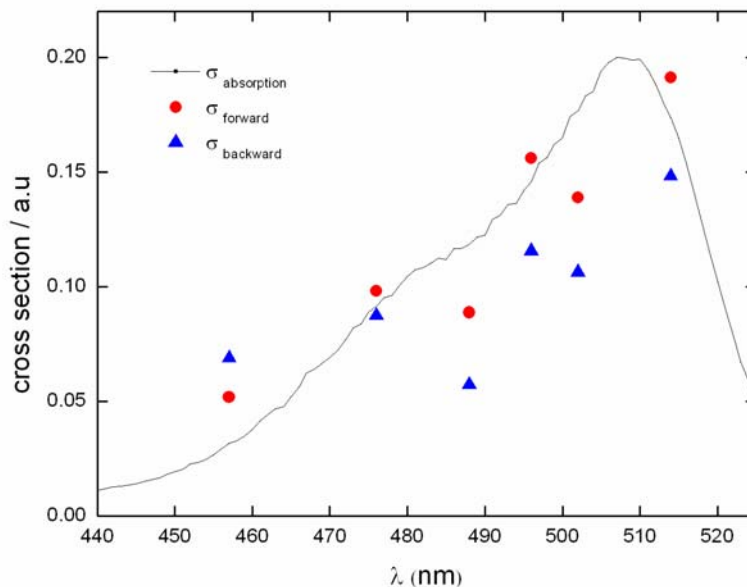


Figure 4.9: $\sigma_{forward}$ and $\sigma_{backward}$ of T203YE222Q mutant against excitation spectrum. Wavelength scale is shown in the x-axis.

As reported earlier, irradiation of GFP results decarboxylation of glutamic acid at the position 222 which is explained by Kolbe-type mechanism (van Thor et al., 2002). The phenolic hydroxyl group of the chromophore is hydrogen bonded via a water molecule to Ser205 and γ -carboxylate of Glu222. In this network, electrostatic repulsion between γ -carboxylate of Glu222 and the phenolic chromophore has been proposed to stabilize the protonated state of the chromophore (Brejč et al., 1997; Palm et al., 1997). Crystal structure of S65T mutant shows that Glu222 is not hydrogen bonded with phenolate oxygen of the chromophore (Ormö et al., 1996). Van Thor et al (2002) proposed that, upon excitation of the GFP chromophore, transfer of charge between the phenolic and imidazolidinone rings of the chromophore will compete with electron transfer from Glu222 to the chromophore. Transfer of an electron results the decarboxylation of Glu222 from the γ -carboxyl radical. This results in the formation of an unstable radical at Glu222. This then leads to retro-transfer of electron and proton (or a hydrogen radical) from the chromophore, which becomes protonated. All these mechanisms are shown in the figure 4.10.

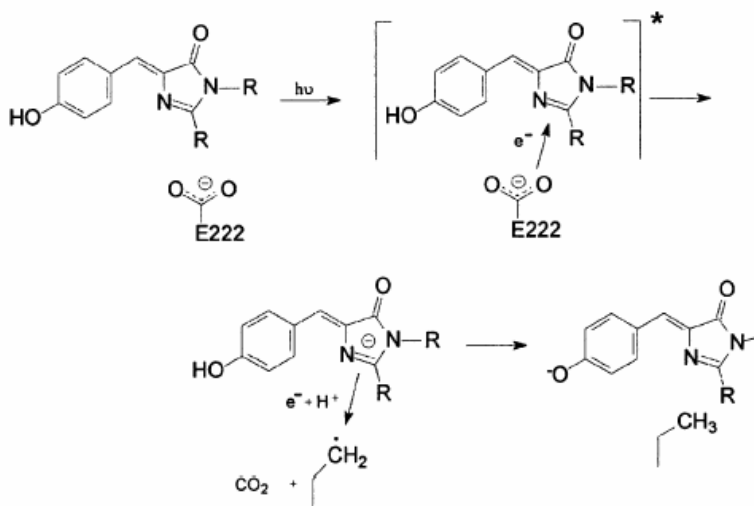


Figure 4.10: Proposed mechanism for light-induced decarboxylation of wt-GFP. The two R substituents represent the covalent links to the remainder of the protein. (Adapted from van Thor et al., 2002)

In an alternative expression, we could imagine that the red shift in the cross section ($\sigma_{forward}$) in the case of EYFP (figure 4.8) is due to this mechanism. The intermediate, the unstable radical or the concomitant rearrangement of other neighboring residues are responsible for such a shift in the cross section. Light driven decarboxylation leads to a new excitation spectrum and this might be a minor population. It has been reported earlier that the light driven decarboxylation reaction strongly depends on the excitation wavelength (Bell et al., 2003). The different oxidizing power of the excited states populated by the distinct wavelengths is proposed to be responsible for the observed wavelength dependence. From the figure 4.8 it is obvious that the shift is more prominent at lower wavelength as proposed by Bell et al. (2003). Interestingly, this shift is not observed in T203YE222Q mutant as Glu at 222 is replaced by Gln. Such a light induced decarboxylation is not possible in this mutant and all the cross section follows the real excitation spectrum.

Chapter 5

Effect of membrane potential on the diffusion time of $K^+(Na^+)/H^+$ exchanger in red blood cell membrane using fluorescence correlation spectroscopy

The experiments presented on this chapter were made in collaboration with Prof. Dr. Ingolf Bernhardt, Central Isotope Laboratory/ Laboratory of Biophysics, Saarland University.

5.1 Introduction

In FCS, the fluorescence fluctuation arises due to the movement of fluorophore in and out of the small confocal volume. This technique has been used in many *in vitro* studies due to its high sensitivity. Confocal detection for reducing the background fluorescence and processing the data at high spatial resolution permit to study the dynamics of fluorescent molecules in the intracellular compartments. FCS allows the determination of cell-to-cell and position-to-position variability. FCS has been applied to study the cell membrane dynamics, determining intracellular concentration, localization of molecules in the cytoplasm, cellular membranes and nuclei in cells. A more detailed application on cells is provided in chapter 1. Recently, diffusion of rhodamine (Rh) labeled A-beta peptide in the red blood cell (RBC) membrane has been investigated by FCS (Takahashi et al., 2003), which showed that the inserted Rh-A-beta into the cell membrane diffused heterogeneously. We followed some experiments from this publication and found that the data is in accordance with the previous results.

5.1.1 Red blood cell membrane transport and the $K^+(Na^+)/H^+$ exchanger

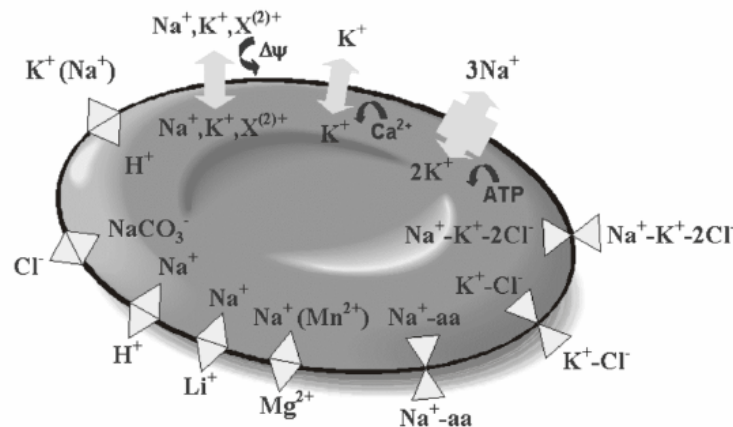


Figure 5.1: Principal transport pathways for Na^+ and K^+ in the human RBC membrane (Adapted from Bernhardt and Weiss, 2003).

The presence of a cotransport system for Na^+ and K^+ , which is sensitive to diuretic drugs such as furosemide but insensitive to ouabain was first discussed in the seventies (Wiley and Cooper, 1975). Several other ion transport pathways have also been reported in the RBC membrane. This includes $Na^+-K^+-2Cl^-$ symporter, K^+-Cl^- symporter, Na^+ -dependent amino acid (aa) transport (several discrete transporters), $Na^+(Mn^{2+})/Mg^{2+}$ antiporter, Na^+/Li^+ antiporter, Na^+/H^+ antiporter, $NaCO_3^-/Cl^-$ exchange (via band 3), $K^+(Na^+)/H^+$ antiporter, Ca^{2+} -activated K^+ channel and non-selective voltage-activated cation channel as shown in figure 5.1. The $K^+(Na^+)/H^+$ exchanger was identified in the human RBC membrane (Kummerow et al., 2000; Richter et al., 1997) and cloned in humans (Numata and Orlowski, 2001). It explains at least partially the leak for Na^+ and K^+ in the human RBC.

Na^+ transport systems are abundant in the RBC compared to the K^+ transport. Finding out the residual fluxes, i.e. the fluxes after the inhibition of the existing specific transport pathways, of each ion are much complicated. One of the best methods to determine the residual K^+ fluxes is to arrest the Na^+/K^+ pump, $Na^+-K^+-2Cl^-$ cotransport, Ca^{2+} -activated K^+ channel and K^+ flux mediated by the Cl^- -dependent K^+-Cl^- cotransport system by using ouabain, bumetanide (or furosemide), EGTA and replacement of chloride in the cell suspending solution by nitrate (or methylsulphate) respectively (Dunham et al., 1980; Ellory et al., 1982; Payne et al., 1990). Two transport pathways, the voltage-dependent, non-specific cation channel (Kaestner et al., 2000) and the $K^+(Na^+)/H^+$ exchanger (Kummerow et al., 2000; Richter et al., 1997) are still not disturbed under these conditions. However, the non-specific cation channel is activated only at positive transmembrane potential and therefore it should not play a substantial role at physiological conditions, i.e. at negative transmembrane potential. Contribution of the $K^+(Na^+)/H^+$ exchanger is more complicated to analyze, since no suitable inhibitor is presently available for the study. First studies have been done to find inhibitors for $K^+(Na^+)/H^+$ exchanger (Weiss et al., 2004).

Several attempts have been demonstrated to prove the H^+ influx and K^+ efflux through the $K^+(Na^+)/H^+$ exchanger. For this, RBCs were suspended in physiological (HIS) NaCl solution, LIS solution (NaCl replaced by sucrose) and in solution where Cl^-

was replaced by the impermeable anion tartrate. Under physiological conditions (pH outside the cell $pH_o = 7.4$), the pH inside the cell (pH_i) is ~ 7.19 and remains constant for 30 min. However, in LIS solution an immediate alkalization ($pH_i \sim 7.70$) followed by a slower cell acidification was observed (Kummerow et al., 2000). Replacing the Cl^- for tartrate causes very positive transmembrane potential which were used to decide whether the H^+ flux is depending on the transmembrane potential. By this method, nearly the same alkaline shift is observed as that in LIS solution. A similar transmembrane potential was observed after the alkalization in LIS and tartrate solutions. From this, one can conclude that the observed H^+ influx was not due to the altered transmembrane potential. Kummerow et al. (2000) also showed the effect of immediate alkalization in LIS which occurs via anion transport system (band 3). Further evidence for the existence of the $K^+(Na^+)/H^+$ exchanger is given by the effect of three anion transport inhibitors (DIDS, DNDS, niflumic acid) on the K^+ efflux and H^+ influx (Kummerow et al., 2000).

5.1.2 The red blood cell membrane potential profile

The value of transmembrane potential of human RBCs has been reported earlier and is about -5 to -10 mV by several experimental techniques like microelectrodes (Jay and Burton, 1969), fluorescent dyes (Freedman and Hoffman, 1979) and by measuring distribution of chloride ions and radioactive lipophilic ions (Beauge, 1975; Deutsch et al., 1979). Variation of the ionic strength of the solution surrounding the RBCs causes several changes in the electric potential profile of the cell and can lead to structural changes in the glycoproteins and glycolipids. When the RBCs are treated with non steady-state conditions like LIS media, the transmembrane potential changes with time until a new steady-state situation is reached. $K^+(Na^+)/H^+$ exchanger and some non-specific voltage activated cation channel are activated in LIS media. By checking the external and internal concentration of K^+ , Na^+ and Cl^- , the transmembrane potential can be calculated. An increase in transmembrane potential causes a change in K^+ efflux. A tri-phasic increase is noted by Donlon and Rothstein (1969). A schematic representation of membrane potential profile is shown in the figure 5.2.

The membrane electric field is another important parameter which influences the membrane constituents. The electric field inside a biological cell membrane is determined by the gradient of the electric potential in all three dimensions. The electric field strength in a RBC membrane under physiological conditions can be assumed to be in the order of 10^6 V/m. The transmembrane potential, the outer and inner surface potential and the electric field strength inside the biological membrane are of fundamental importance in influencing and regulating specific ion transport pathways (pumps, channels, carriers).

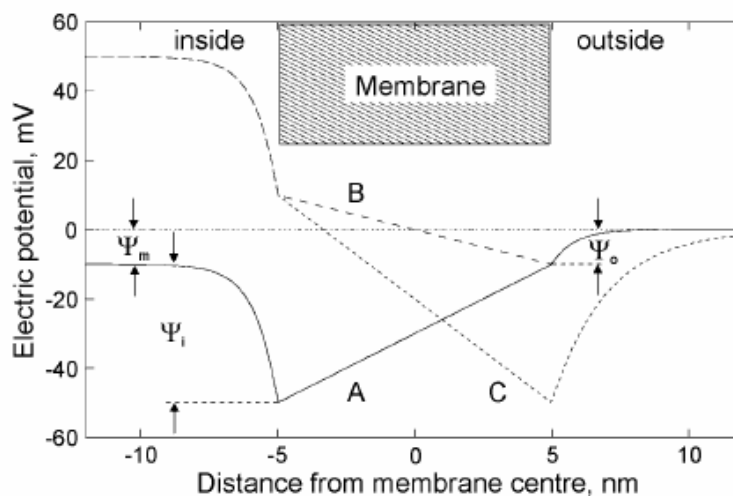


Figure 5.2: Membrane potential profile across the RBC membrane. Ψ_m - the transmembrane (diffusion) potential, Ψ_0 - outer surface potential, Ψ_i - inner surface potential, A - physiological ionic strength solution, e.g. sodium chloride containing solution, B - solution of reduced Cl^- concentration but constant ionic strength (compared to A), e.g. sodium tartrate containing solution, C - solution of low ionic strength (LIS), e.g. sucrose solution (Adapted from Bernhardt and Weiss, 2003).

5.2 Experimental considerations

A detailed view of FCS set up is described in chapter 1, section 1.3.1.1. Imaging of RBC was done by using a piezoscanner (Piezosystem Jena GmbH, Germany) attached to the microscope body; images were obtained by TimeHarp 200 PC-board (PicoQuant GmbH, Germany) and the images were viewed by PicoQuant SCX View software (PicoQuant GmbH, Germany). The power of the laser beam entering the microscope was set to 10 -

15 μ W. For better adhesion of RBC, the glass coverslips have been pre-treated with poly-lysine (0.001%). The laser beam was either focused on the cell membrane after scanning with the piezo scanner and moving the coverslip by using TimeHarp 200 software or by positioning it manually (a schematic diagram is shown in the figure 5.3). Dual-autocorrelation curves were taken immediately after positioning the laser beam on the membrane using a hardware correlator (FLEX 02 D, www.correlator.com).

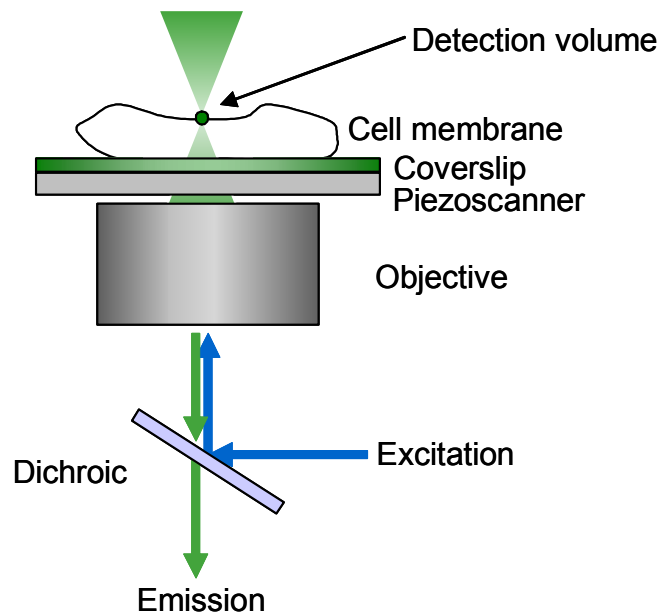


Figure 5.3: Focussing the laser beam on the cell membrane.

5.2.1 Data analysis

The measured fluorescence autocorrelation function $g^2(\tau)$ were fitted with a two-component model (equation 5.1) by means of commercial software (Origin Pro 7.5, Origin Lab, MA, USA).

$$g^2(\tau) = 1 + \frac{f}{N} \left(\frac{1}{1 + \frac{\tau}{\tau_{d1}}} \right) + \frac{(1-f)}{N} \left(\frac{1}{1 + \frac{\tau}{\tau_{d2}}} \right) \quad (5.1)$$

N denotes the number of fluorescent molecules within the detection volume, τ_{d1} is the diffusion time of the fraction f and τ_{d2} is the diffusion time of the remaining fraction of labelled molecules. The two component model was used speculating that there will be an unbound dye and a dye bound to the exchanger or the movement of bound exchanger will be hindered by the other membrane components. The diffusion time τ_d is the average time it takes for a molecule to diffuse through the radial part of the observation volume of the microscope. However, the diffusion time changes with the size of the observation volume, wavelength of excitation laser and the optical properties of the instrument. The diffusion coefficient (constant) D is a property of a molecule in a given solvent and better suited to characterize experimental data than the diffusion time. The diffusion coefficient D can be calculated from the corresponding diffusion time according to:

$$\tau_d = \frac{\omega_0^2}{4D} \quad (5.2)$$

Here ω_0 is the beam waist of the detection volume, which is formed from the Gaussian beam profile convolved with the pinhole profile (see 1.3.2).

5.2.2 Preparation of red blood cells for FCS measurements

Heparin stabilized blood samples of healthy donors were obtained from the Universitaetsklinikum, Homburg and Sports Centre, Saarbruecken, Germany. The human RBCs were obtained after washing the blood sample by centrifuging three times at 2000g for 5 min in physiological (high) ionic strength (HIS) solution containing 145 mM NaCl, 7.5 mM KCl, 10 mM glucose and 10 mM HEPES titrated with NaOH to pH 7.4. After each wash the supernatant containing plasma and buffy coat were aspirated. Washed RBCs (1% haematocrit) were incubated for 30-40 min at 37°C in the dark with BODIPY FL amiloride (400 nM) for labelling the $K^+(Na^+)/H^+$ exchanger. Cells were then washed in physiological solution by centrifuging at 2000g for 5 min to remove the unbound fluorescent dye and were re-suspended (0.01% haematocrit).

Nonpolar β -BODIPY (R) FL-C12-HPC (1 μ M) was incubated with washed RBCs (1% heamatocrit) for 30 min at 37°C. The low ionic strength (LIS) solution (pH 7.4) used for the experiments contains 250 mM or 200 mM sucrose instead of NaCl to maintain a constant osmolarity and cell volume respectively. We have also used a solution where NaCl has been replaced by 107 mM sodium tartrate. Futhermore, we have used two slightly changed physiological solutions (145 mM NaCl, HIS), one with reduced concentration of NaCl (120 mM) and the other with added 30 mM sucrose (HIS Sucrose). In these solutions, the surface potential of RBCs remains similar to HIS solution but the volume is affected (Bernhardt and Weiss, 2003).

For the measurements in LIS or sodium tartrate solutions the last washing procedure has been carried out in the corresponding solution, the incubation time remained the same as stated above. RBCs (1% haematocrit) were incubated with Octadecyl rhodamine B chloride (R18) (1 nM) for 30 min (Takahashi et al., 2003). After incubation, the unbound dye has been washed out. BODIPY FL amiloride, β -BODIPY (R) FL-C12-HPC and Octadecyl rhodamine B chloride were purchased from Molecular Probes, Inc. All the other chemicals were of the highest purity grade available.

5.3 Results and discussion

FCS measurements in the RBC membrane allow us to investigate the diffusion time of the $K^+(Na^+)/H^+$ exchanger in different ionic strength solutions. All FCS curves were fitted by using the two component model (equation 5.1) and by using equation 5.2, the diffusion constant D was calculated. In the whole experiment the beam waist ω_0 (at $\lambda_{exc}=488$ nm) of the laser was calculated as ~ 450 nm and this indicates that the area of the cell in which the diffusion studied was $\sim 0.6 \mu m^2$. The resolution in the z -direction for these measurements was $\sim 7 \mu m$. In the beginning, several measurements were done to optimize the proper illumination intensity, right z -position and to improve the quality of the data. We could also observe some photo damage of RBCs under long term laser irradiation which were studied in detail elsewhere (Bloom and Webb, 1984; Wong et al., 2007). To test whether the obtained diffusion constant could be attributed by the low stability of the

measurement system or errors in the data processing, control experiments were carried out. For the control experiments, FCS was done with the RBC membrane labeled with R18. The diffusion constant obtained ($3.8 \times 10^{-10} \text{ cm}^2/\text{s}$) was in agreement with the results published by Takahashi et al., (2003).

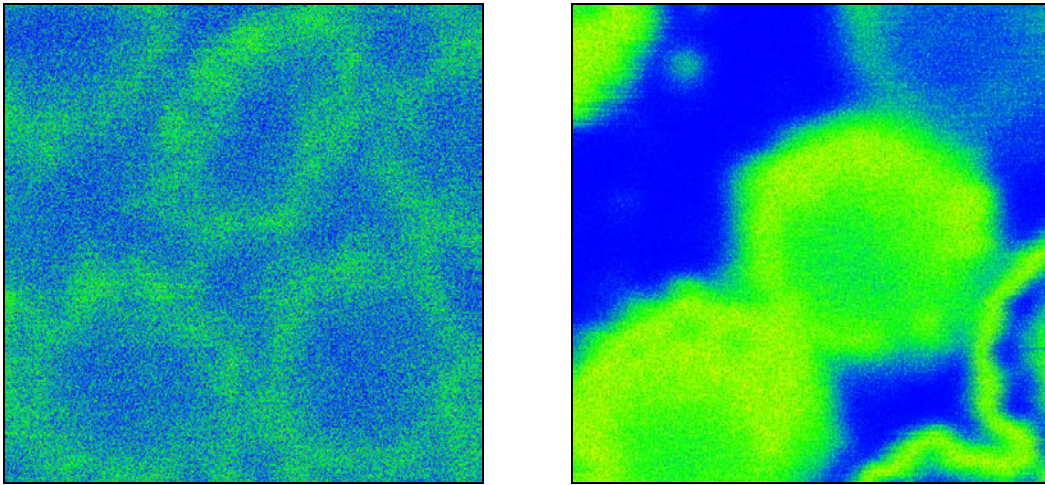


Figure 5.4: A confocal image of RBCs labeled with BODIPY FL amiloride (at equatorial layer) (left) and R18 (at upper cell surface) (right) in HIS solution.

5.3.1 Autocorrelation curve for the experiment

The autocorrelation functions obtained from the membrane measurements were typical for living cells as observed in several studies before (Politz et al., 1998; Schwille et al., 1999a; Takahashi et al., 2003). Autocorrelation curves taken in various solutions are shown in figure 5.5. From the curves, clearly more than one diffusion time were observed. The advantage of FCS studies is to get an impression about the mobility of the $K^+(Na^+)/H^+$ exchanger under conditions with different transmembrane potential of the RBCs.

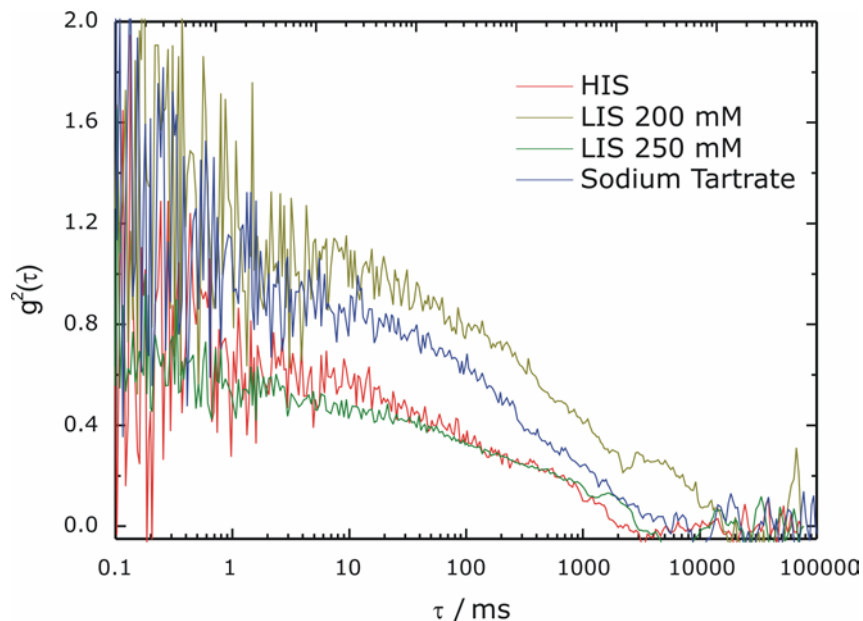


Figure 5.5: Fluorescence autocorrelation curves taken with RBC membranes in different ionic strength solutions (BODIPY FL amiloride labeled exchanger).

5.3.2 Diffusion of the $K^+(Na^+)/H^+$ exchanger labeled with BODIPY FL amiloride

After fitting with the two component model, we could extract two diffusion constants for corresponding experimental solutions. From the correlation curves, it is clearly evident that these are fast moving fluorescent species and slow moving fluorescent species. First, we assumed that the fast moving species (with higher diffusion constant) corresponds to the free dye and the slow moving species (with slower diffusion constant) corresponds to the labeled exchanger. If it is so, one should observe approximately a constant diffusion time for the free dye through out the solutions, but this was not the case. The above assumption will become wrong if there is $\sim 100\%$ labeling of the dye molecules. During the cell preparation, the washing procedures will remove all the unlabeled dyes otherwise it may also be present in the experimental solution and that can hinder single molecule experiments with FCS. In this aspect, we assume that the fast moving species (particles with higher diffusion constant) reflect the non-hindered (free) diffusion of the $K^+(Na^+)/H^+$ exchanger in the membrane and the slow moving species (particles with low diffusion constant) reflect the hindered diffusion. This hindered diffusion can be due to

the aggregation of two or more exchangers (i.e. bigger particles), or more general due to protein-protein and protein-lipid interaction. However, it seems more likely that the obtained variation of the diffusion constants reflect the interaction of the $K^+(Na^+)/H^+$ exchanger with the cytoskeleton, which is affected in a different way in the solutions used which is described below.

Accordingly, from the figure 5.6 A, diffusion constant 'a' corresponds to the free diffusion of the $K^+(Na^+)/H^+$ exchanger and the diffusion constant 'b' corresponds to the hindered diffusion. The standard deviation was also calculated from the measured values and is shown as error bars. Diffusion constant for the $K^+(Na^+)/H^+$ exchanger is found to be maximum in HIS containing sucrose solution ($432 \times 10^{-10} \text{ cm}^2/\text{s}$) where the fraction rate was only 23%. However, the diffusion constant in solutions such as HIS 120 mM ($213 \times 10^{-10} \text{ cm}^2/\text{s}$) and LIS 200 mM ($177 \times 10^{-10} \text{ cm}^2/\text{s}$) are more or less similar and having the fraction rates 38% and 73%, respectively. The diffusion constant obtained in other solutions are as follows: HIS ($143 \times 10^{-10} \text{ cm}^2/\text{s}$), LIS 250 mM ($78 \times 10^{-10} \text{ cm}^2/\text{s}$), sodium tartrate ($59 \times 10^{-10} \text{ cm}^2/\text{s}$). The fraction of the labeled molecule remains almost same in these solutions i. e., ~40%.

Among the different HIS solutions used, the cell volume changes but the surface potential remains similar. When the RBCs are treated with solutions HIS sucrose, HIS 120 and HIS; the RBC attain lowest cell volume (cell shrinks) in sucrose containing HIS solution. However, in our experiments the highest diffusion constant can be seen in sucrose containing HIS solution. The reason is still unknown as when the cell shrinks, the exchanger may be tightly packed in the membrane and such a fast movement may not be possible. Sodium tartrate solution is accompanied by the high ionic strength and alkalization of the cell and in which lowest diffusion constant of the exchanger is observed. Such alkalization is also seen in LIS solutions and those are having smaller diffusion constant.

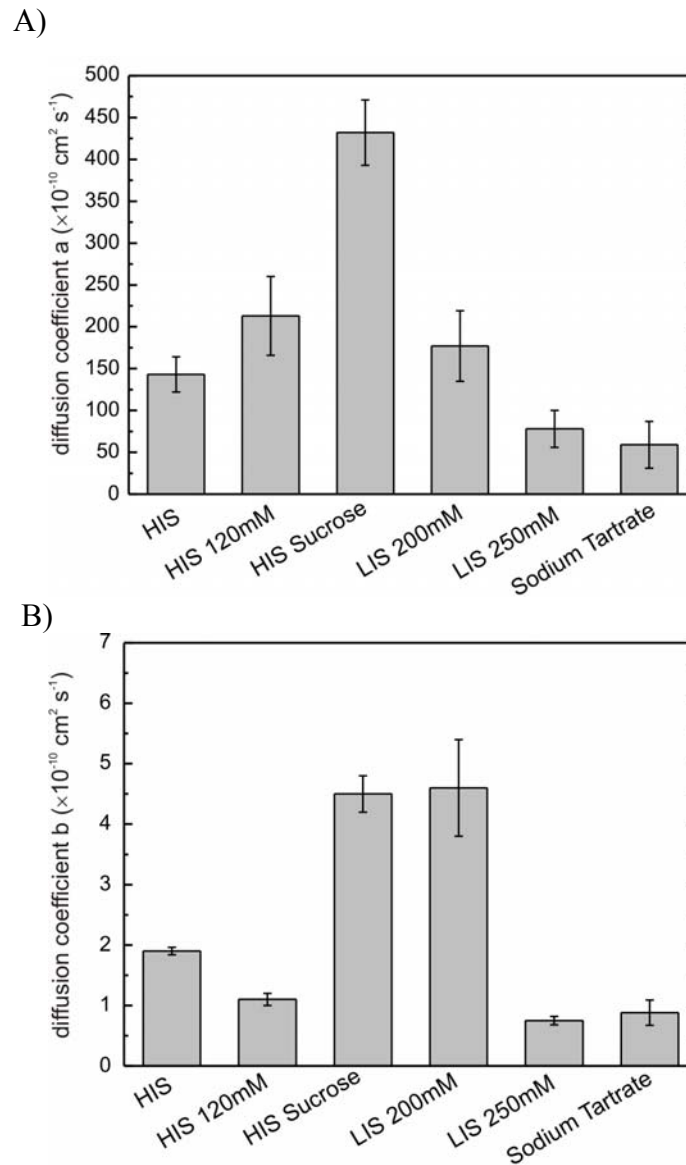


Figure 5.6 : Diffusion constants (A: constants a, B: constants b, below) of BODIPY FL amiloride labeled $K^+(Na^+)/H^+$ exchanger in different solutions.

The diffusion constant 'b' (see figure 5.6 B) for the hindered diffusion is found to be almost the same value in LIS 200 mM solution ($4.65 \times 10^{-10} \text{ cm}^2/\text{s}$, fraction rate-30%) and sucrose containing HIS ($4.59 \times 10^{-10} \text{ cm}^2/\text{s}$, fraction rate-70%) solution. The diffusion constant in other solutions are: HIS ($1.95 \times 10^{-10} \text{ cm}^2/\text{s}$), HIS 120 mM ($1.06 \times 10^{-10} \text{ cm}^2/\text{s}$), LIS 250 mM ($0.74 \times 10^{-10} \text{ cm}^2/\text{s}$) and sodium tartrate ($0.87 \times 10^{-10} \text{ cm}^2/\text{s}$) where the fraction of the labeled exchanger molecules remains almost the same i. e., ~60%. There are no big

differences in the diffusion constant of hindered diffusion in different solutions which makes it difficult to interpret the data.

5.3.4 Diffusion of β -BODIPY (R) FL-C12-HPC labeled lipids

Lipid labeled membrane is useful for monitoring the change of membrane stability under any environmental conditions. It will be much interesting to know the changes in the lipid membrane by applying different membrane potentials. It has been reported that the electric field inside a biological membrane influences the mobility and the position of the hydrocarbon chains of the phospholipids as well as the phase transition temperature (Forsyth et al., 1977; Jähnig, 1976; Träuble and Eibl, 1974). FCS measurements were done after labeling the RBC membrane by lipid specific β -BODIPY (R) FL-C12-HPC. The calculated diffusion constant 'a' (figure 5. 7) in all the experimental solutions were found to be almost similar ($\sim 250 \times 10^{-10} \text{ cm}^2/\text{s}$) and this is much higher than the expected value for β -BODIPY (R) FL-C12-HPC. This may be due to the hindered diffusion of the dye in the membrane and a description of such a diffusion process is given in 1.4.

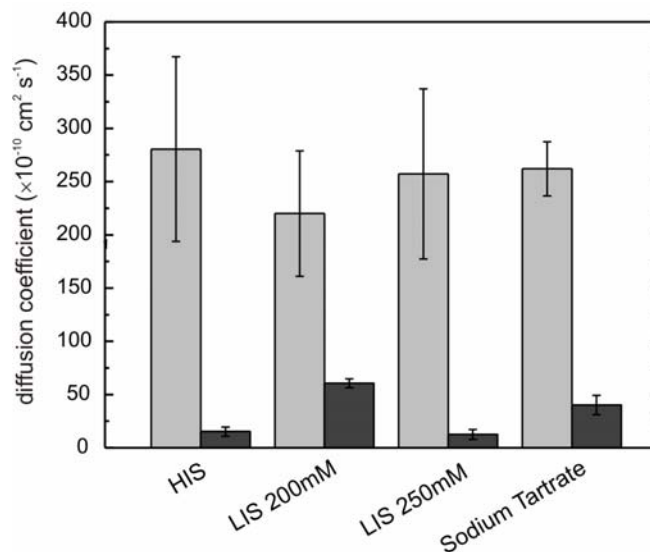


Figure 5.7: Diffusion constants of β -BODIPY (R) FL-C12-HPC labeled lipids in the RBC membrane. Grey bars and black bars indicate the diffusion constant 'a' and diffusion constant 'b', respectively.

The values of diffusion constant 'b' (figure 5. 7) are in agreement with the previously published results (Korlach et al., 1999) where the phase behavior of phospholipids/cholesterol bilayers was studied by FCS. Recently, the diffusion constant of fluorescent phosphatidylinositol 4, 5-bisphosphate in the plasma membrane of cells have been studied (Golebiewska et al., 2008). Diffusion constant for HIS and LIS 250 mM solutions (15×10^{-10} cm²/s and 12×10^{-10} cm²/s) were found to be almost similar but different from the diffusion constants observed in LIS 200 mM and sodium tartrate solutions (60×10^{-10} cm²/s and 40×10^{-10} cm²/s respectively). These obtained results make it complicated to decide which parameter (transmembrane potential, surface potential, and/or cell volume) have a significant effect on the lipid diffusion in the RBC membrane.

Chapter 6

Characterization of nanoparticles tagged with oligonucleotides using fluorescence correlation spectroscopy

The experiments presented on this chapter were made in collaboration with Dr. Marc Schneider, Department of Biopharmaceutics and Pharmaceutical Technology, Saarland University

6.1 Introduction

Nanoparticles are microscopic particles and particulate dispersions or solid colloidal particles with a size in the range of 10-1000 nm. They are prepared by methods using dispersion, polymerization or ionic gelation. Depending on the method of preparation, there are nanoparticles, nanospheres or nanocapsules. They are used as particulate carriers in various pharmaceutical applications. The drug is incorporated into the nanoparticles in many ways like dissolving, entrapping, encapsulating or attaching to the nanoparticle matrix. Recently, biodegradable polymeric nanoparticles which are coated with hydrophobic polymer such as polyethylene glycol (PEG) known as long-circulating particles, have been used as potential drug delivery devices.

DNA/RNA drug delivery is gaining potential applications in pharmaceuticals. Antisense-oligonucleotides are short single stranded DNA or RNA molecules (12-25 nucleotides) and are effective blocking agents of protein expression with a high sequence specificity (Stephenson and Zamecnik, 1978; Zamecnik and Stephenson, 1978). However, degradation by nuclease and weak permeability through biological cell membranes make them less accessible for biological applications (Fattal et al., 1998; Lebedeva et al., 2000). Here comes the most demanding delivery system, cationic nanoparticles, for better delivery of oligonucleotides. Chitosan-coated poly (lactic-co-glycolic acid) (PLGA) nanoparticles have been used as efficient carriers for the delivery of plasmid DNA into A549 lung cancer cells *in vitro* and lungs of mice after intranasal administration *in vivo* (Ravi Kumar et al., 2004). PLGA nanoparticles have been used as drug delivery vehicles for blood–brain barrier (Costantino et al., 2006), gastrointestinal mucosa (Lamprecht et al., 2001), nasal mucosa (Csaba et al., 2006) and ocular tissue (Dillen et al., 2004). Suitability of these nanoparticles as gene carriers was confirmed by studying their binding with the antisense oligonucleotides 2'-O-methyl-RNA (OMR) (a 13mer directed against the template region of human telomerase RNA) for the treatment of lung cancer through telomerase inhibition (Pitts and Corey, 1998). In this study, we characterized the nanoparticles using FCS for determining the diffusion time and the size of the particle.

6.2 Materials and Methods

6.2.1 Preparation and purification of nanoparticles

Chitosan-coated PLGA nanoparticles were prepared by emulsification-diffusion-evaporation technique (Ravi Kumar et al., 2004; Taetz et al., 2008). Briefly, a solution of PLGA (5 ml) and ethyl acetate (20 mg/ml) was added dropwise to 5 ml of an aqueous chitosan solution containing 2.5% w/v polyvinyl alcohol (PVA) under magnetic stirring (1000 rpm, 1 hour). The homogenized (13,500 rpm, 15 min) emulsion was diluted to a volume of 50 ml under constant stirring with MilliQ-water and the remaining ethyl acetate was evaporated by continuous stirring (over night at room temperature). The concentrations of chitosan in the aqueous phase were varied to obtain nanoparticles with different surface charges (Nafee et al., 2007). This chitosan-coated PLGA nanoparticles were purified from excess PVA by preparative size exclusion chromatography using an FPLC[®] system (Amersham Biosciences; Uppsala, Sweden) as described by Taetz et al., (2008).

6.2.2 Preparation of Fluoresceinamin (FA) labeled PLGA nanoparticles

5-Fluoresceinamin (FA) bound PLGA (FA-PLGA) was prepared using the method described by Horisawa et al., (2002). In brief, PLGA (3.07 g) and FA (0.0583 g) were dissolved in 30 ml of acetonitrile with 0.0408 g of DMAP and incubated at room temperature for 24 h with gentle stirring (under light protected conditions). Obtained FA-PLGA was precipitated by adding water and later separated by centrifugation. FA-PLGA nanoparticles were prepared by interfacial polymer deposition. FA-PLGA (3100 mg) was dissolved in 16 ml of acetone at room temperature. 3 ml of ethanol was added to the polymer solution (final concentration 5.3 mg/ml), pumped into 25 ml of a 0.5% PVA solution in purified water and gently stirred with a magnetic stirrer. Using rotary evaporator, the residual organic solvent was removed and lyophilized.

6.2.3 Formation of nanoplexes

Chitosan-coated PLGA nanoparticles were mixed with a solution of carboxyfluoresceinamine (FAM) labeled oligonucleotides, vortexed for 30 seconds and incubated in orbital shaker at room temperature (Nafee et al., 2007).

The details of purchased chemicals were described elsewhere (Nafee et al., 2007).

6.2.4 Fluorescence correlation spectroscopy with nanoparticles

All measurements were carried out in a custom made laser scanning confocal microscope as described in 1.3.1.1. Diffusion time of FAM-oligonucleotides, FA-PLGA nanoparticles and nanoplexes were determined by taking autocorrelation curves. Obtained autocorrelation curves were fitted by using two component model as shown in the equation 5.1, chapter 2. The diameter of the nanoparticles was characterized using the equation: $R = \frac{kT}{6\pi\eta D}$ where k denotes the Boltzmann constant (1.38×10^{-23} J/K), T is the absolute temperature (300 K) and η is the viscosity of the solvent (for water 8.9×10^{-4} kg.m.s). Samples were prepared in Millipore water with a concentration of 10 nM and power of the laser beam was set to 10-30 μ W at $\lambda_{exc} = 488$ nm.

6.3 Results and Discussion

FCS is a well-suited screening tool in the pharmaceutical industry (Medina and Schwille, 2002; Winkler et al., 1999). Here we have shown that the effective utilization of FCS in characterizing the nanoparticles and their interaction with oligonucleotides.

Autocorrelation curve for FAM labeled oligonucleotide is shown in the figure 6. 1. Fitting with two component model reveals two different diffusion times, one corresponds to the fast moving species (0.17 ms) and the other corresponds to the slow moving species (1.16 ms). Calculated diffusion constant (2.8×10^{-6} cm²/s) of the fast moving

species which is approximately equal to the diffusion constant of carboxyfluorescein ($3.2 \times 10^{-6} \text{ cm}^2/\text{s}$). The higher diffusion time (1.16 ms) corresponds to the FAM labeled oligonucleotide which is in accordance with the previous results (Politz et al., 1998) where the molecular movement of Fluorescein labeled oligonucleotides were studied in the culture. From the fraction rate, it is known that in this experimental solution 95% of the oligonucleotides are labeled with FAM and the fraction of FAM is only 5%.

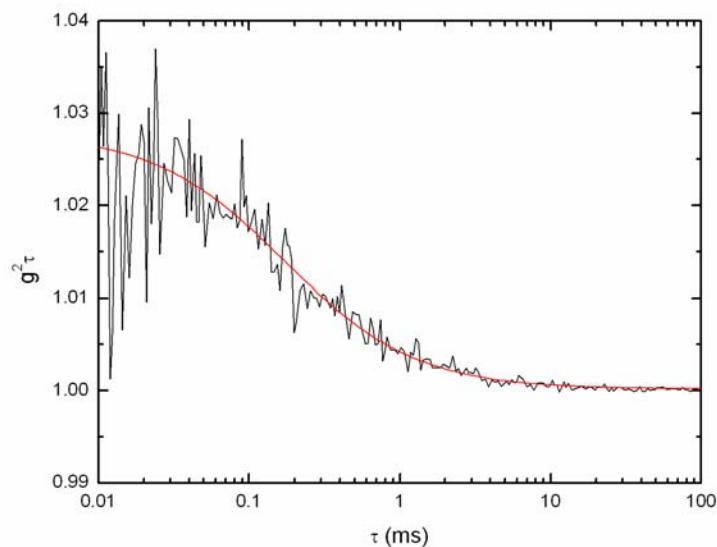


Figure 6.1: Autocorrelation curve for FAM labeled oligonucleotide. A fit (red curve) with two component equation is also shown.

When the FA-PLGA nanoparticles are introduced in to the FCS, high fluorescence fluctuations can be seen from the fluorescence fluctuation profile and the diffusion time increases to 17.7 ms (figure 6. 2). With two component fitting, one can observe same diffusion time for both the species which means there is almost complete labeling of the FA.

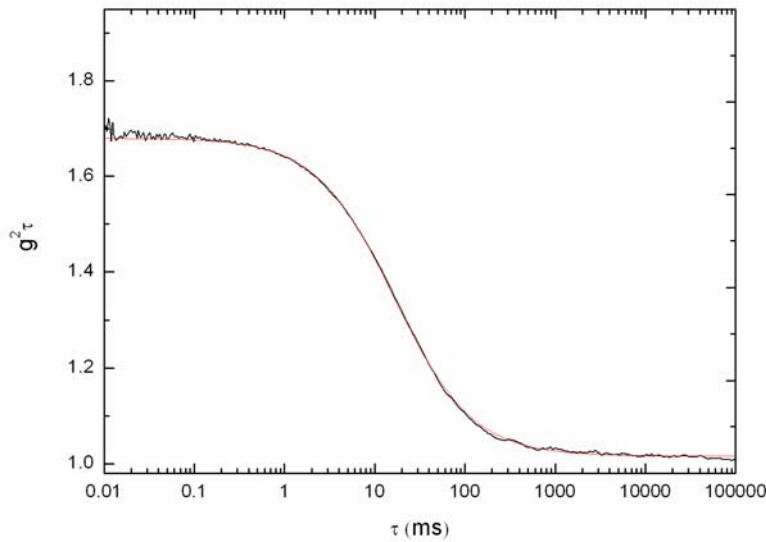


Figure 6.2: Autocorrelation curve (black) for FA-PLGA nanoparticles with two component fitting (red curve).

Hydrodynamic radius of the PLGA nanoparticle is obtained by calculating the diffusion constant ($D = \frac{\omega_0}{4\tau_d}$). Applying the values of k , T , π and η in $R = \frac{kT}{6\pi\eta D}$, we get a new solution for hydrodynamic radius: $R = 0.2469 \times 10^{-18} / D$. For the diffusion time 17.7 ms, the diffusion constant is $0.27 \times 10^{-7} \text{ cm}^2/\text{s}$ and the hydrodynamic radius is 91.4 nm. This value is approximately the same value of hydrodynamic radius obtained by our particle size measurements. This proves the accuracy of FCS.

The diffusion time is very high when the PLGA nanoparticles are complexed with FAM-oligonucleotides i.e. 54.7 ms (fraction rate is 89%) (figure 6. 3). A fast moving component is also observed with a fraction rate of 11% with a diffusion time of 4 ms which is slightly higher than that of FAM labeled oligonucleotide.

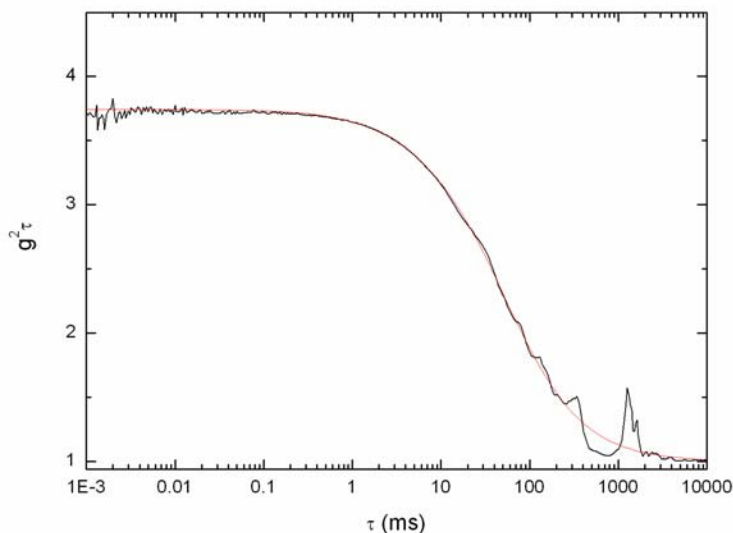


Figure 6.3: Autocorrelation curve (black) for PLGA nanoparticles with two component fit (red curve).

From the above experiments it is obvious that the diffusion of oligonucleotides becoming slower by the complexation with nanoparticles. This slow movement of the carrier may hinder the drug delivery experiments. Using this method, one could also evaluate the speed of the carrier molecule in different biological solutions for optimizing the experimental conditions. This method is also well suited for the association and dissociation of carriers.

By fluorescence lifetime measurements, we also observed an interesting point about the lifetime of the Fluorescein (figure 6. 4). The FAM-labeled oligonucleotide is having only a lifetime of 2.8 ns compared to that of Fluorescein in Millipore water (~ 3.8 ns). Such a quenching is unexpected by the addition of oligonucleotide. It might be due to the complex formation of the FAM-labeled oligonucleotides in Millipore water.

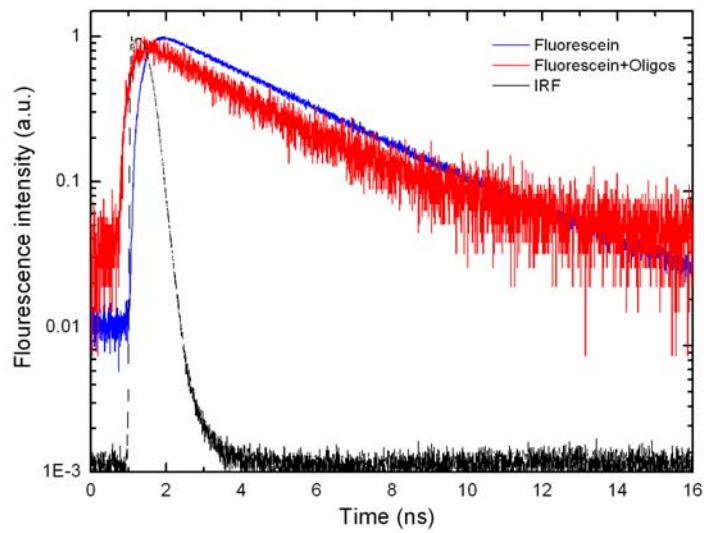


Figure 6.4: Fluorescence lifetime measurements with Fluorescein (blue) and FAM labeled oligonucleotides (red). Black line indicates the instrument response function (IRF).

Chapter 7: Appendices

Table 1: Standard aminoacid abbreviations.

One letter code	Three letter code	Name
A	Ala	Alanine
C	Cys	Cysteine
D	Asp	Aspartic Acid
E	Glu	Glutamic Acid
F	Phe	Phenylalanine
G	Gly	Glycine
H	His	Histidine
I	Ile	Isoleucine
K	Lys	Lysine
L	Leu	Leucine
M	Met	Methionine
N	Asn	Asparagine
P	Pro	Proline
Q	Gln	Glutamine
R	Arg	Arginine
S	Ser	Serine
T	Thr	Threonine
V	Val	Valine
W	Trp	Tryptophan
Y	Tyr	Tyrosine

Table 2: Diffusion constant D, diffusion time τ and fraction rate F of BODIPY FL amiloride labeled $K^+(Na^+)H^+$ exchanger in different solutions.

Solutions	τ_{d1} (ms)	$Da (\times 10^{-10})$ (cm^2/s)	F1 (%)	τ_{d2} (ms)	$Db (\times 10^{-10})$ (cm^2/s)	F2 (%)
HIS	34	143	32	2446	1.9	69
HIS 120 mM	23	213	38	4540	1.1	62
HIS Sucrose	11	432	23	1049	4.5	77
LIS 200 mM	28	177	73	1044	4.6	30
LIS 250 mM	65	78	42	6458	0.75	58
Sod.Tartrate	97	59	46	5692	0.88	54

Table 3: Diffusion constant D, diffusion time τ and fraction rate F of β -BODIPY (R) FL-C12-HPC labeled lipid in the RBC membrane.

Solutions	τ_{d1} (ms)	$Da (\times 10^{-10})$ (cm^2/s)	F1 (%)	τ_{d2} (ms)	$Db (\times 10^{-10})$ (cm^2/s)	F2 (%)
HIS	18	280	46	334	15	54
LIS 200 mM	23	220	31	79	60	68
LIS 250 mM	20	257	29	442	12	71
Sod.Tartrate	18	262	54	124	40	45

References

- 1 Aragon, S. R., and Pecora, R. (1975). Fluorescence correlation spectroscopy and Brownian rotational diffusion. *Biopolymers* 14, 119-137.
- 2 Aubin, J. E. (1979). Autofluorescence of viable cultured mammalian cells. *J Histochem Cytochem* 27, 36-43.
- 3 Bae, J. H., Paramita Pal, P., Moroder, L., Huber, R., and Budisa, N. (2004). Crystallographic evidence for isomeric chromophores in 3-fluorotyrosyl-green fluorescent protein. *ChemBiochem* 5, 720-722.
- 4 Beauge, L. (1975). Non-pumped sodium fluxes in human red blood cells. Evidence for facilitated diffusion. *Biochim Biophys Acta* 401, 95-108.
- 5 Bell, A. F., Stoner-Ma, D., Wachter, R. M., and Tonge, P. J. (2003). Light-driven decarboxylation of wild-type green fluorescent protein. *J Am Chem Soc* 125, 6919-6926.
- 6 Benson, R. C., Meyer, R. A., Zaruba, M. E., and McKhann, G. M. (1979). Cellular autofluorescence-is it due to flavins?. *J Histochem Cytochem* 27, 44-48.
- 7 Berne, B. J., and Pecora, P. (1975). *Dynamic light scattering, with applications to chemistry, biology and physics*. Wiley, New York.
- 8 Bernhardt, I., Weiss, E. (2003). Passive membrane permeability for ions and the membrane potential. *Red cell membrane transport in health and disease* (I. Bernhardt, J.C. Ellory, eds.). Springer-Verlag, Berlin, 83-109.
- 9 Bizzarri, R., Nifosi, R., Abbruzzetti, S., Rocchia, W., Guidi, S., Arosio, D., Garau, G., Campanini, B., Grandi, E., and Ricci, F. (2007). Green fluorescent protein ground states: the influence of a second protonation site near the chromophore. *Biochemistry* 46, 5494-5504.
- 10 Blab, A., Lommerse, P. H. M., Cognet, L., Harms, G. S., and Schmidt, T. (2001). Two-photon excitation action cross-sections of the autofluorescent proteins. *Chem Phys Lett* 350, 71-77.
- 11 Bloom, J. A., and Webb, W. W. (1984). Photodamage to intact erythrocyte membranes at high laser intensities: methods of assay and suppression. *J Histochem Cytochem* 32, 608-616.

- 12 Bokman, S. H., and Ward, W. W. (1981). Renaturation of *Aequorea* green-fluorescent protein. *Biochem Biophys Res Commun* *101*, 1372-1380.
- 13 Bonnet, G., Krichevsky, O., and Libchaber, A. (1998). Kinetics of conformational fluctuations in DNA hairpin-loops. *Proc Natl Acad Sci USA* *95*, 8602-8606.
- 14 Borsch, M., Turina, P., Eggeling, C., Fries, J. R., Seidel, C. A., Labahn, A., and Graber, P. (1998). Conformational changes of the H⁺-ATPase from *Escherichia coli* upon nucleotide binding detected by single molecule fluorescence. *FEBS Lett* *437*, 251-254.
- 15 Bouchaud, J. P., and Antoine, G. (1990). Anomalous diffusion in disordered media: Statistical mechanisms, models and physical applications. *Physics Reports* *195*, 127-293.
- 16 Brejc, K., Sixma, T. K., Kitts, P. A., Kain, S. R., Tsien, R. Y., Ormoe, M., and Remington, S. J. (1997). Structural basis for dual excitation and photoisomerization of the *Aequorea victoria* green fluorescent protein. *Proc Natl Acad Sci USA* *94*, 2306-2311.
- 17 Briandet, R., Lacroix-Gueu, P., Renault, M., Lecart, S., Meylheuc, T., Bidnenko, E., Steenkeste, K., Bellon-Fontaine, M. N., and Fontaine-Aupart, M. P. (2008). Fluorescence correlation spectroscopy to study diffusion and reaction of bacteriophages inside biofilms. *Appl Environ Microbiol* *74*, 2135-2143.
- 18 Briddon, S. J., Middleton, R. J., Cordeaux, Y., Flavin, F. M., Weinstein, J. A., George, M. W., Kellam, B., and Hill, S. J. (2004). Quantitative analysis of the formation and diffusion of A1-adenosine receptor-antagonist complexes in single living cells. *Proc Natl Acad Sci USA* *101*, 4673-4678.
- 19 Brock, R., Hink, M. A., and Jovin, T. M. (1998). Fluorescence correlation microscopy of cells in the presence of autofluorescence. *Biophys J* *75*, 2547-2557.
- 20 Brooks, B., Phillips, R. S., and Benisek, W. F. (1998). High-efficiency incorporation in vivo of tyrosine analogues with altered hydroxyl acidity in place of the catalytic tyrosine-14 of Delta 5-3-ketosteroid isomerase of *Comamonas (Pseudomonas) testosteroni*: effects of the modifications on isomerase kinetics. *Biochemistry* *37*, 9738-9742.
- 21 Budisa, N., Pal, P. P., Alefelder, S., Birle, P., Krywcun, T., Rubini, M., Wenger, W., Bae, J. H., and Steiner, T. (2004). Probing the role of tryptophans in *Aequorea victoria* green fluorescent proteins with an expanded genetic code. *Biol Chem* *385*, 191-202.

- 22 Chalfie, M., Tu, Y., Euskirchen, G., Ward, W. W., and Prasher, D. C. (1994). Green fluorescent protein as a marker for gene expression. *Science* 263, 802-805.
- 23 Chen, Y., Muller, J. D., Ruan, Q., and Gratton, E. (2002). Molecular brightness characterization of EGFP in vivo by fluorescence fluctuation spectroscopy. *Biophys J* 82, 133-144.
- 24 Chen, Y., Muller, J. D., Tetin, S. Y., Tyner, J. D., and Gratton, E. (2000). Probing ligand protein binding equilibria with fluorescence fluctuation spectroscopy. *Biophys J* 79, 1074-1084.
- 25 Cluzel, P., Surette, M., and Leibler, S. (2000). An ultrasensitive bacterial motor revealed by monitoring signaling proteins in single cells. *Science* 287, 1652-1655.
- 26 Cody, C. W., Prasher, D. C., Westler, W. M., Prendergast, F. G., and Ward, W. W. (1993). Chemical structure of the hexapeptide chromophore of the *Aequorea* green-fluorescent protein. *Biochemistry* 32, 1212-1218.
- 27 Cormack, B. P., Valdivia, R. H., and Falkow, S. (1996). FACS-optimized mutants of the green fluorescent protein (GFP). *Gene* 173, 33-38.
- 28 Costantino, L., Gandolfi, F., Bossy-Nobs, L., Tosi, G., Gurny, R., Rivasi, F., Vandelli, M. A., and Forni, F. (2006). Nanoparticulate drug carriers based on hybrid poly (D, L-lactide-co-glycolide)- dendron structures. *Biomaterials* 27, 4635-4645.
- 29 Cramer, A., Whitehorn, E. A., Tate, E., and Stemmer, W. P. (1996). Improved green fluorescent protein by molecular evolution using DNA shuffling. *Nat Biotechnol* 14, 315-319.
- 30 Creed, D. (1984). The photophysics and photochemistry of the near UV absorbing amino-acids. *J Photochem Photobiol B* 63, 114-125.
- 31 Csaba, N., Sanchez, A., and Alonso, M. J. (2006). PLGA: poloxamer and PLGA: poloxamine blend nanostructures as carriers for nasal gene delivery. *J Control Release* 113, 164-172.
- 32 Cubitt, A. B., Heim, R., Adams, S. R., Boyd, A. E., Gross, L. A., and Tsien, R. Y. (1995). Understanding, improving and using green fluorescent proteins. *Trends Biochem Sci* 20, 448-455.
- 33 Cubitt, A. B., Woollenweber, L. A., and Heim, R. (1999). Understanding structure-function relationships in the *Aequorea victoria* green fluorescent protein. *Methods Cell Biol* 58, 19-30.

- 34 Delagrave, S., Hawtin, R. E., Silva, C. M., Yang, M. M., and Youvan, D. C. (1995). Red-shifted excitation mutants of the green fluorescent protein. *Biotechnology (N Y)* *13*, 151-154.
- 35 Delie, F., Gurny, R., and Zimmer, A. (2001). Fluorescence correlation spectroscopy for the characterisation of drug delivery systems. *Biol Chem* *382*, 487-490.
- 36 Denk, W., Strickler, J. H., and Webb, W. W. (1990). Two-photon laser scanning fluorescence microscopy. *Science* *248*, 73-76.
- 37 Deutsch, C. J., Holian, A., Holian, S. K., Daniele, R. P., and Wilson, D. F. (1979). Transmembrane electrical and pH gradients across human erythrocytes and human peripheral lymphocytes. *J Cell Physiol* *99*, 79-93.
- 38 Dickson, R. M., Cubitt, A. B., Tsien, R. Y., and Moerner, W. E. (1997). On/off blinking and switching behaviour of single molecules of green fluorescent protein. *Nature* *388*, 355-358.
- 39 Dillen, K., Weyenberg, W., Vandervoort, J., and Ludwig, A. (2004). The influence of the use of viscosifying agents as dispersion media on the drug release properties from PLGA nanoparticles. *Eur J Pharm Biopharm* *58*, 539-549.
- 40 Dittrich, P., and Schwille, P. (2001). Photobleaching and stabilization of fluorophores used for single-molecule analysis with one- and two-photon excitation. *Appl Phys B* *73*, 829-837.
- 41 Donlon, J. A., and Rothstein, A. (1969). The cation permeability of erythrocytes in low ionic strength media of various tonicities. *J Membrane Biol* *1*, 37-52.
- 42 Dunham, P. B., Stewart, G. W., and Ellory, J. C. (1980). Chloride-activated passive potassium transport in human erythrocytes. *Proc Natl Acad Sci U S A* *77*, 1711-1715.
- 43 Edman, L., Mets, U., and Rigler, R. (1996). Conformational transitions monitored for single molecules in solution. *Proc Natl Acad Sci U S A* *93*, 6710-6715.
- 44 Eggeling, C., Volkmer, A., and Seidel, C. A. (2005). Molecular photobleaching kinetics of Rhodamine 6G by one- and two-photon induced confocal fluorescence microscopy. *Chemphyschem* *6*, 791-804.
- 45 Eggeling, C., Widegren, J., and Rigler, R., and Seidel, C. A. M. (1998). Photobleaching of fluorescent dyes under conditions used for single-molecule detection: evidence of two-step photolysis. *Anal Chem* *70*, 2651-2659.
- 46 Ehrenberg, M., and Rigler, R. (1974). Rotational Brownian motion and fluorescence intensity fluctuations. *Phys Chem* *4*, 390-401.

-
- 47 Ehrig, T., O'Kane, D. J., and Prendergast, F. G. (1995). Green-fluorescent protein mutants with altered fluorescence excitation spectra. *FEBS Lett* *367*, 163-166.
 - 48 Eid, J. S., Mueller, J. D., and Gratton, E. (2000). Data acquisition card for fluctuation correlation spectroscopy allowing full access to the detected photon sequence. *Rev Sci Instrum* *71*, 361-368.
 - 49 Eigen, M., and Rigler, R. (1994). Sorting single molecules: application to diagnostics and evolutionary biotechnology. *Proc Natl Acad Sci U S A* *91*, 5740-5747.
 - 50 Ellory, J. C., Dunham, P. B., Logue, P. J., and Stewart, G. W. (1982). Anion-dependent cation transport in erythrocytes. *Philos Trans R Soc Lond B Biol Sci* *299*, 483-495.
 - 51 Elson, E. L., and Magde, D. (1974). Fluorescence correlation spectroscopy. I. Conceptual basis and theory. *Biopolymers* *13*, 1-27.
 - 52 Enderlein, J., Gregor, I., Patra, D., and Fitter, J. (2005). Statistical analysis of diffusion coefficient determination by fluorescence correlation spectroscopy. *J Fluoresc* *15*, 415-422.
 - 53 Fattal, E., Vauthier, C., Aynie, I., Nakada, Y., Lambert, G., Malvy, C., and Couvreur, P. (1998). Biodegradable polyalkylcyanoacrylate nanoparticles for the delivery of oligonucleotides. *J Control Release* *53*, 137-143.
 - 54 Feher, G., and Weissman, M. (1973). Fluctuation Spectroscopy: Determination of Chemical reaction kinetics from the frequency spectrum of fluctuations. *Proc Natl Acad Sci USA* *70*, 870-875.
 - 55 Forsyth, P. A., Jr., Marcelja, S., Mitchell, D. J., and Ninham, B. W. (1977). Phase transition in charged lipid membranes. *Biochim Biophys Acta* *469*, 335-344.
 - 56 Freedman, J. C., and Hoffman, J. F. (1979). The relation between dicarbocyanine dye fluorescence and the membrane potential of human red blood cells set at varying Donnan equilibria. *J Gen Physiol* *74*, 187-212.
 - 57 Fukuda, H., Arai, M., and Kuwajima, K. (2000). Folding of green fluorescent protein and the cycle3 mutant. *Biochemistry* *39*, 12025-12032.
 - 58 Golebiewska, U., Nyako, M., Woturski, W., Zaitseva, I., and McLaughlin, S. (2008). Diffusion coefficient of fluorescent phosphatidylinositol 4,5-bisphosphate in the plasma membrane of cells. *Mol Biol Cell* *19*, 1663-1669.

-
- 59 Gregor, I., Patra, D., and Enderlein, J. (2005). Optical saturation in fluorescence correlation spectroscopy under continuous-wave and pulsed excitation. *Chemphyschem* 6, 164-170.
- 60 Guigas, G., Kalla, C., and Weiss, M. (2007). Probing the nanoscale viscoelasticity of intracellular fluids in living cells. *Biophys J* 93, 316-323.
- 61 Harms, G. S., Cognet, L., Lommerse, P. H., Blab, G. A., and Schmidt, T. (2001). Autofluorescent proteins in single-molecule research: applications to live cell imaging microscopy. *Biophys J* 80, 2396-2408.
- 62 Harms, G. S., Cognet, L., Lommerse, P. H., Blab, G. A., Kahr, H., Gamsjager, R., Spaink, H. P., Soldatov, N. M., Romanin, C., and Schmidt, T. (2001). Single-molecule imaging of l-type Ca^{2+} channels in live cells. *Biophys J* 81, 2639-2646.
- 63 Hasler, K., Panke, O., and Junge, W. (1999). On the stator of rotary ATP synthase: the binding strength of subunit delta to (alpha beta)₃ as determined by fluorescence correlation spectroscopy. *Biochemistry* 38, 13759-13765.
- 64 Haupts, U., Maiti, S., Schwille, P., and Webb, W. W. (1998). Dynamics of fluorescence fluctuations in green fluorescent protein observed by fluorescence correlation spectroscopy. *Proc Natl Acad Sci USA* 95, 13573-13578.
- 65 Heim, R., and Tsien, R. Y. (1996). Engineering green fluorescent protein for improved brightness, longer wavelengths and fluorescence resonance energy transfer. *Curr Biol* 6, 178-182.
- 66 Heim, R., Cubitt, A. B., and Tsien, R. Y. (1995). Improved green fluorescence. *Nature* 373, 663-664.
- 67 Heim, R., Prasher, D. C., and Tsien, R. Y. (1994). Wavelength mutations and posttranslational autooxidation of green fluorescent protein. *Proc Natl Acad Sci U S A* 91, 12501-12504.
- 68 Hodgkin, A. L., and Katz, B. (1949). The effect of sodium ions on the electrical activity of the giant axon of the squid. *J Physiol* 108, 37-77.
- 69 Horisawa, E., Kubota, K., Tuboi, I., Sato, K., Yamamoto, H., Takeuchi, H., and Kawashima, Y. (2002). Size-dependency of DL-lactide/glycolide copolymer particulates for intra-articular delivery system on phagocytosis in rat synovium. *Pharm Res* 19, 132-139.

- 70 Hossain, S., Grande, M., Ahmadkhanov, G., and Pramanik, A. (2007). Binding of the Alzheimer amyloid beta-peptide to neuronal cell membranes by fluorescence correlation spectroscopy. *Exp Mol Pathol* 82, 169-174.
- 71 Jähnig, F. (1976). Electrostatic free energy and shift of the phase transition for charged lipid membranes. *Biophys Chem* 4, 309-318.
- 72 Jay, A. W., and Burton, A. C. (1969). Direct measurement of potential difference across the human red blood cell membrane. *Biophys J* 9, 115-121.
- 73 Jimenez-Banzo, A., Nonell, S., Hofkens, J., and Flors, C. (2008). Singlet oxygen photosensitization by EGFP and its chromophore HBDI. *Biophys J* 94, 168-172.
- 74 Jung, G., and Zumbusch, A. (2006). Improving autofluorescent proteins: Comparative studies of the effective brightness of green fluorescent protein (GFP) mutants. *Micros Res Techn* 69, 175-185.
- 75 Jung, G., Bräuchle, C., and Zumbusch, A. (2001). Two-color fluorescence correlation spectroscopy of one chromophore: Application to the E222Q mutant of the green fluorescent protein. *J Chem Phys* 114, 3149–3156.
- 76 Jung, G., Wiehler, J., and Zumbusch, A. (2005). The photophysics of green fluorescent protein: influence of the key amino acids at positions 65, 203, and 222. *Biophys J* 88, 1932-1947.
- 77 Jung, G., Wiehler, J., Göhde, W., Tittel, J., Basché, T., Steipe, B., and Bräuchle, C. (1998). Confocal microscopy of single molecules of the green fluorescent protein. *Bioimaging* 6, 54-61.
- 78 Kaestner, L., Christophersen, P., Bernhardt, I., and Bennekou, P. (2000). The non-selective voltage-activated cation channel in the human red blood cell membrane: reconciliation between two conflicting reports and further characterisation. *Bioelectrochemistry* 52, 117-125.
- 79 Kane, J. F., and Hartley, D. L. (1988). Formation of recombinant protein inclusion bodies in *Escherichia coli*. *Trends Biotechnol* 14, 95-101.
- 80 Khoroshilova, E. V., and Nikogosyan, D. N. (1990). Photochemistry of uridine on high intensity laser UV irradiation. *J Photochem Photobiol B* 5, 413-27.
- 81 Koppel, D. E., Axelrod, D., Schlessinger, J., Elson, E. L., and Webb, W. W. (1976). Dynamics of fluorescence marker concentration as a probe of mobility. *Biophys J* 16, 1315-1329.

-
- 82 Korlach, J., Schwille, P., Webb, W. W., and Feigenson, G. W. (1999). Characterization of lipid bilayer phases by confocal microscopy and fluorescence correlation spectroscopy. *Proc Natl Acad Sci U S A* *96*, 8461-8466.
- 83 Krichevsky, O., and Bonnet, G. (2002). Fluorescence correlation spectroscopy: the technique and its applications. *Rep Prog Phys* *65*, 251-297.
- 84 Kubitscheck, U., Kuckmann, O., Kues, T., and Peters, R. (2000). Imaging and tracking of single GFP molecules in solution. *Biophys J* *78*, 2170-2179.
- 85 Kummer, A. D., Kompa, C., Lossau, H., Dammer, F. P., Michel-Beyerle, M. E., Silva, C. M., Bylina, B. J., Coleman, W. J., Yang, M. M., and Youva, D. C. (1998). Dramatic reduction in fluorescence quantum yield in mutants of green fluorescent protein due to fast internal conversion. *Chemical Physics* *237*, 183-193.
- 86 Kummer, A., Wiehler, H., Rehaber, H., Kompa, C., Steipe, B., and Michel-Beyerle, M. E. (2000). Effect of threonine 203 replacements on excited-state dynamics and fluorescence properties of green fluorescent protein (GFP). *J Phys Chem B* *104*, 4791-4798.
- 87 Kummerow, D., Hamann, J., Browning, J. A., Wilkins, R., Ellory, J. C., and Bernhardt, I. (2000). Variations of intracellular pH in human erythrocytes via K^+ (Na^+)/ H^+ exchange under low ionic strength conditions. *J Membr Biol* *176*, 207-216.
- 88 Lamb, D. C., Schenk, A., Rocker, C., Scalfi-Happ, C., and Nienhaus, G. U. (2000). Sensitivity enhancement in fluorescence correlation spectroscopy of multiple species using time-gated detection. *Biophys J* *79*, 1129-1138.
- 89 Lamprecht, A., Ubrich, N., Yamamoto, H., Schafer, U., Takeuchi, H., Maincent, P., Kawashima, Y., and Lehr, C. M. (2001). Biodegradable nanoparticles for targeted drug delivery in treatment of inflammatory bowel disease. *J Pharmacol Exp Ther* *299*, 775-781.
- 90 Lebedeva, I., Benimetskaya, L., Stein, C. A., and Vilenchik, M. (2000). Cellular delivery of antisense oligonucleotides. *Eur J Pharm Biopharm* *50*, 101-119.
- 91 Leutenegger, M., Blom, H., Widengren, J., Eggeling, C., Gosch, M., Leitgeb, R. A., and Lasser, T. (2006). Dual-color total internal reflection fluorescence cross-correlation spectroscopy. *J Biomed Opt* *11*, 040502.1-040502.3.
- 92 Magde, D., Elson, E. L., and Webb, W. W. (1974). Fluorescence correlation spectroscopy. II. An experimental realization. *Biopolymers* *13*, 29-61.

-
- 93 Magde, D., Elson, E. L., and Webb, W. W. (1972). Thermodynamic fluctuations in a reacting system: Measurement by fluorescence correlation spectroscopy. *Phys Rev Lett* *29*, 705.
- 94 Maiti, S., Haupts, U., and Webb, W. W. (1997). Fluorescence correlation spectroscopy: diagnostics for sparse molecules. *Proc Natl Acad Sci USA* *94*, 11753-11757.
- 95 Margeat, E., Poujol, N., Boulahtouf, A., Chen, Y., Muller, J. D., Gratton, E., Cavailles, V., and Royer, C. A. (2001). The human estrogen receptor alpha dimer binds a single SRC-1 coactivator molecule with an affinity dictated by agonist structure. *J Mol Biol* *306*, 433-442.
- 96 Medina, M. A., and Schwille, P. (2002). Fluorescence correlation spectroscopy for the detection and study of single molecules in biology. *Bioessays* *24*, 758-764.
- 97 Meissner, O., and Haberlein, H. (2003). Lateral mobility and specific binding to GABA_A receptors on hippocampal neurons monitored by fluorescence correlation spectroscopy. *Biochemistry* *42*, 1667-1672.
- 98 Meseth, U., Wohland, T., Rigler, R., and Vogel, H. (1999). Resolution of fluorescence correlation measurements. *Biophys J* *76*, 1619-1631.
- 99 Meyer-Almes, F. J., Wyzgol, K., and Powell, M. J. (1998). Mechanism of the alpha-complementation reaction of *E. coli* beta-galactosidase deduced from fluorescence correlation spectroscopy measurements. *Biophys Chem* *75*, 151-160.
- 100 Morise, H., Shimomura, O., Johnson, F. H., and Winant, J. (1974). Intermolecular energy transfer in the bioluminescent system of *Aequorea*. *Biochemistry* *13*, 2656-2662.
- 101 Müller, J. D., Chen, Y., and Gratton, E. (2003). Fluorescence correlation spectroscopy. *Methods Enzymol* *361*, 69-92.
- 102 Nafee, N., Taetz, S., Schneider, M., Schaefer, U. F., and Lehr, C. M. (2007). Chitosan-coated PLGA nanoparticles for DNA/RNA delivery: effect of the formulation parameters on complexation and transfection of antisense oligonucleotides. *Nanomedicine* *3*, 173-183.
- 103 Nagai, Y., Miyazaki, M., Aoki, R., Zama, T., Inouye, S., Hirose, K., Ino, M., and Hagiwara, M. (2000). A fluorescent indicator for visualizing cAMP-induced phosphorylation in vivo. *Nat Biotechnol* *18*, 313-316.
- 104 Neher, E., and Sakmann, B. (1976). Single-channel currents recorded from membrane of denervated frog muscle fibres. *Nature* *260*, 799-802.

-
- 105 Nifosi, R., and Tozzini, V. (2003). Molecular dynamics simulations of enhanced green fluorescent proteins: effects of F64L, S65T and T203Y mutations on the ground-state proton equilibria. *Proteins* 51, 378-389.
- 106 Nikogosyan, D. N. (1987). Definition of photoreaction quantum yield at two-quantum excitation of molecules in solution. *Laser Chem* 7, 29-34.
- 107 Numata, M., and Orłowski, J. (2001). Molecular cloning and characterization of a novel (Na⁺, K⁺)/H⁺ exchanger localized to the trans-golgi network. *J Biol Chem* 276, 17387-17394.
- 108 Ohsugi, Y., Saito, K., Tamura, M., and Kinjo, M. (2006). Lateral mobility of membrane-binding proteins in living cells measured by total internal reflection fluorescence correlation spectroscopy. *Biophys J* 91, 3456-3464.
- 109 Ormö, M., Cubitt, A. B., Kallio, K., Gross, L. A., Tsien, R. Y., and Remington, S. J. (1996). Crystal structure of the *Aequorea victoria* green fluorescent protein. *Science* 273, 1392-1395.
- 110 Pack, C. G., Nishimura, G., Tamura, M., Aoki, K., Taguchi, H., Yoshida, M., and Kinjo, M. (1999). Analysis of interaction between chaperonin GroEL and its substrate using fluorescence correlation spectroscopy. *Cytometry* 36, 247-253.
- 111 Palm, G. J., Zdanov, A., Gaitanaris, G. A., Stauber, R., Pavlakis, G. N., and Wlodawer, A. (1997). The structural basis for spectral variations in green fluorescent protein. *Nat Struct Biol* 4, 361-365.
- 112 Pal, P. P., Bae, J. H., Azim, M. K., Hess, P., Friedrich, R., Huber, R., Moroder, L., and Budisa, N. (2005). Structural and spectral response of *Aequorea victoria* green fluorescent proteins to chromophore fluorination. *Biochemistry* 44, 3663-3672.
- 113 Patterson, G. H., Knobel, S. M., Sharif, W. D., Kain, S. R., and Piston, D. W. (1997). Use of the green fluorescent protein and its mutants in quantitative fluorescence microscopy. *Biophys J* 73, 2782-2790.
- 114 Payne, J. A., Lytle, C., and McManus, T. J. (1990). Foreign anion substitution for chloride in human red blood cells: effect on ionic and osmotic equilibria. *Am J Physiol* 259, 819-827.
- 115 Petersen, N. O., Hoddellius, P. L., Wiseman, P. W., Seger, O., and Magnusson, K. E. (1993). Quantitation of membrane receptor distributions by image correlation spectroscopy: concept and application. *Biophys J* 65, 1135-1146.

-
- 116 Pick, H., Preuss, A. K., Mayer, M., Wohland, T., Hovius, R., and Vogel, H. (2003). Monitoring expression and clustering of the ionotropic 5HT₃ receptor in plasma membranes of live biological cells. *Biochemistry* *42*, 877-884.
- 117 Pitschke, M., Prior, R., Haupt, M., and Riesner, D. (1998). Detection of single amyloid beta-protein aggregates in the cerebrospinal fluid of Alzheimer's patients by fluorescence correlation spectroscopy. *Nat Med* *4*, 832-834.
- 118 Pitts, A. E., and Corey, D. R. (1998). Inhibition of human telomerase by 2'-O-methyl-RNA. *Proc Natl Acad Sci USA* *95*, 11549-11554.
- 119 Politz, J. C., Browne, E. S., Wolf, D. E., and Pederson, T. (1998). Intranuclear diffusion and hybridization state of oligonucleotides measured by fluorescence correlation spectroscopy in living cells. *Proc Natl Acad Sci U S A* *95*, 6043-6048.
- 120 Post, K., Pitschke, M., Schafer, O., Wille, H., Appel, T. R., Kirsch, D., Mehlhorn, I., Serban, H., Prusiner, S. B., and Riesner, D. (1998). Rapid acquisition of beta-sheet structure in the prion protein prior to multimer formation. *Biol Chem* *379*, 1307-1317.
- 121 Pramanik, A., and Rigler, R. (2001). Ligand-receptor interactions in the membrane of cultured cells monitored by fluorescence correlation spectroscopy. *Biol Chem* *382*, 371-378.
- 122 Pramanik, A., Olsson, M., Langel, U., Bartfai, T., and Rigler, R. (2001). Fluorescence correlation spectroscopy detects galanin receptor diversity on insulinoma cells. *Biochemistry* *40*, 10839-10845.
- 123 Pramanik, A., Thyberg, P., and Rigler, R. (2000). Molecular interactions of peptides with phospholipid vesicle membranes as studied by fluorescence correlation spectroscopy. *Chem Phys Lipids* *104*, 35-47.
- 124 Prasher, D. C., Eckenrode, V. K., Ward, W. W., Prendergast, F. G., and Cormier, M. J. (1992). Primary structure of the *Aequorea victoria* green-fluorescent protein. *Gene* *111*, 229-233.
- 125 Qian, H., and Elson, E. L. (1991). Analysis of confocal laser-microscope optics for 3-D fluorescence correlation spectroscopy. *Appl Opt* *30*, 1185-1195.
- 126 Rao, B., Kemple, M., and Prendergast, F. (1980). Proton nuclear magnetic resonance and fluorescence spectroscopic studies of segmental mobility in aequorin and a green fluorescent protein from *Aequorea forskalea*. *Biophys J* *32*, 630-632.

-
- 127 Ravi Kumar, M. N., Bakowsky, U., and Lehr, C. M. (2004). Preparation and characterization of cationic PLGA nanospheres as DNA carriers. *Biomaterials* 25, 1771-1777.
- 128 Reid, B. G., and Flynn, G. C. (1997). Chromophore formation in green fluorescent protein. *Biochemistry* 36, 6786-6791.
- 129 Rekas, A., Alattia, J. R., Nagai, T., Miyawaki, A., and Ikura, M. (2002). Crystal structure of venus, a yellow fluorescent protein with improved maturation and reduced environmental sensitivity. *J Biol Chem* 277, 50573-50578.
- 130 Richter, S., Hamann, J., Kummerow, D., and Bernhardt, I. (1997). The monovalent cation "leak" transport in human erythrocytes: an electroneutral exchange process. *Biophys J* 73, 733-745.
- 131 Rigler, R. (1995). Fluorescence correlations, single molecule detection and large number screening. Applications in biotechnology. *J Biotechnol* 41, 177-186.
- 132 Rigler, R., Mets, Ü., Widengren, J., and Kask, P. (1993). Fluorescence correlation spectroscopy with high count rate at low background: analysis of translational diffusion. *Eur Biophys J* 22, 169-175.
- 133 Rigler, R., Pramanik, A., Jonasson, P., Kratz, G., Jansson, O. T., Nygren, P., Stahl, S., Ekberg, K., Johansson, B., and Uhlen, S. (1999). Specific binding of proinsulin C-peptide to human cell membranes. *Proc Natl Acad Sci USA* 96, 13318-13323.
- 134 Rigler, R., Widengren, J., and Mets, U. (1992). Fluorescence Spectroscopy: New methods and applications. Wolfbeis O S., editor. Berlin: Springer 13-24.
- 135 Sacchetti, A., Cappetti, V., Marra, P., Dell'Arciprete, R., El Sewedy, T., Crescenzi, C., and Alberti, S. (2001). Green fluorescent protein variants fold differentially in prokaryotic and eukaryotic cells. *J Cell Biochem* 36, 117-128.
- 136 Sakikawa, C., Taguchi, H., Makino, Y., and Yoshida, M. (1999). On the maximum size of proteins to stay and fold in the cavity of GroEL underneath GroES. *J Biol Chem* 274, 21251-21256.
- 137 Satsoura, D., Leber, B., Andrews, D. W., and Fradin, C. (2007). Circumvention of fluorophore photobleaching in fluorescence fluctuation experiments: a beam scanning approach. *Chemphyschem* 8, 834-848.
- 138 Schaefer, D. W. (1973). Dynamics of number fluctuations: motile microorganisms, *Science* 180, 1293-1295.

-
- 139 Schuler, J., Frank, J., Trier, U., Schafer-Korting, M., and Saenger, W. (1999). Interaction kinetics of tetramethylrhodamine transferrin with human transferrin receptor studied by fluorescence correlation spectroscopy. *Biochemistry* 38, 8402-8408.
- 140 Schurer, H., Buchynskyy, A., Korn, K., Famulok, M., Welzei, P., and Hahn, U. (2001). Fluorescence correlation spectroscopy as a new method for the investigation of aptamer/target interactions. *Biol Chem* 382, 479-481.
- 141 Schwille, P., Haupts, U., Maiti, S., and Webb, W. W. (1999a). Molecular dynamics in living cells observed by fluorescence correlation spectroscopy with one- and two-photon excitation. *Biophys J* 77, 2251-2265.
- 142 Schwille, P., Korfach, J., and Webb, W. W. (1999b). Fluorescence correlation spectroscopy with single-molecule sensitivity on cell and model membranes. *Cytometry* 36, 176-182.
- 143 Schwille, P., Kummer, S., Heikal, A. A., Moerner, W. E., and Webb, W. W. (2000). Fluorescence correlation spectroscopy reveals fast optical excitation-driven intramolecular dynamics of yellow fluorescent proteins. *Proc Natl Acad Sci U S A* 97, 151-156.
- 144 Schwille, P., Meyer-Almes, F. J., and Rigler, R. (1997). Dual-color fluorescence cross-correlation spectroscopy for multicomponent diffusional analysis in solution. *Biophys J* 72, 1878-1886.
- 145 Seyedsayamdost, M. R., Reece, S. Y., Nocera, D. G., and Stubbe, J. (2006). Mono-, di-, tri-, and tetra-substituted fluorotyrosines: new probes for enzymes that use tyrosyl radicals in catalysis. *J Am Chem Soc* 128, 1569-1579.
- 146 Siemering, K. R., Golbik, R., Sever, R., and Haseloff, J. (1996). Mutations that suppress the thermosensitivity of green fluorescent protein. *Curr Biol* 6, 1653-1663.
- 147 Song, L., Hennink, E. J., Young, I. T., and Tanke, H. J. (1995). Photobleaching kinetics of fluorescein in quantitative fluorescence microscopy. *Biophys J* 68, 2588-2600.
- 148 Srivastava, M., and Petersen, N. O. (1998). Diffusion of transferrin receptor clusters. *Biophys Chem* 75, 201-211.
- 149 Stephenson, M. L., and Zamecnik, P. C. (1978). Inhibition of Rous sarcoma viral RNA translation by a specific oligodeoxyribonucleotide. *Proc Natl Acad Sci U S A* 75, 285-288.

-
- 150 Sterrer, S., and Henco, K. (1997). Fluorescence correlation spectroscopy (FCS)-a highly sensitive method to analyze drug/target interactions. *J Recept Signal Transduct Res* 17, 511-520.
- 151 Sullivan, K. F., and Kay, S. A. (1999). Green fluorescent proteins (eds). *Methods Cell Biol* 58, 1-369.
- 152 Sun, W. C., Gee, K. R., Klaubert, D. H., and Haugland, R. P.(1997). Synthesis of fluorinated fluoresceins. *J Org Chem* 62, 6469-6475.
- 153 Svedberg, T., and Inouye, K. (1911). Eine neue Methode zur Prufung der Gultigkeit des Boyle-Gay-Lussacschen Gesetzes fuer Kolloide Loesungen. *Z physik Chemie* 77, 145-191.
- 154 Taetz, S., Nafee, N., Beisner, J., Piotrowska, K., Baldes, C., Murdter, T. E., Huwer, H., Schneider, M., Schaefer, U. F., Klotz, U., and Lehr, C. M. (2008). The influence of chitosan content in cationic chitosan/PLGA nanoparticles on the delivery efficiency of antisense 2'-O-methyl-RNA directed against telomerase in lung cancer cells. *Eur J Pharm Biopharm.* (Article in Press).
- 155 Takahashi, Y., Bark, N., Kinjo, M., and Rigler, R. (2003). Fluorescence correlation spectroscopy (FCS) analysis of human red blood cell system. *Opt Rev* 10, 596-599.
- 156 Thompson, N. L., Burghardt, T. P., and Axelrod, D. (1981). Measuring surface dynamics of biomolecules by total internal reflection fluorescence with photobleaching recovery or correlation spectroscopy. *Biophys J* 33, 435-454.
- 157 Thompson, N. (1991). Fluorescence correlation spectroscopy in topics in fluorescence spectroscopy (Lakowicz, J.R.,Ed.). Vol. I Plenum Press New York.
- 158 Träuble, H., and Eibl, H. (1974). Electrostatic effects on lipid phase transitions: membrane structure and ionic environment. *Proc Natl Acad Sci USA* 71, 214-219.
- 159 Tsien, R. Y. (1998). The green fluorescent protein. *Annu Rev Biochem* 67, 509-544.
- 160 Tyagi, S., and Kramer, F. R. (1996). Molecular beacons: probes that fluoresce upon hybridization. *Nat Biotechnol* 14, 303-308.
- 161 Van Craenenbroeck, E., and Engelborghs, Y. (2000). Fluorescence correlation spectroscopy: molecular recognition at the single molecule level. *J Mol Recognit* 13, 93-100.

-
- 162 van Thor, J. J., Gensch, T., Hellingwerf, K. J., and Johnson, L. N. (2002). Phototransformation of green fluorescent protein with UV and visible light leads to decarboxylation of glutamate 222. *Nat Struct Biol* 9, 37-41.
- 163 Veettil, S., Budisa, N., and Jung, G. (2008). Photostability of green and yellow fluorescent proteins with fluorinated chromophores, investigated by fluorescence correlation spectroscopy. *Biophys Chem* 136, 38-43.
- 164 Verkhusha, V. V., and Lukyanov, K. A. (2004). The molecular properties and applications of Anthozoa fluorescent proteins and chromoproteins. *Nat Biotechnol* 22, 289-296.
- 165 Von Smoluchowski, M. (1914). Studien ueber Molekularstatistik von Emulsionen und deren Zusammenhang mit der Brownschen Bewegung. *Wien Berichte* 123, 2381-2405.
- 166 Wachsmuth, M., Waldeck, W., and Langowski, J. (2000). Anomalous diffusion of fluorescent probes inside living cell nuclei investigated by spatially-resolved fluorescence correlation spectroscopy. *J Mol Biol* 298, 677-689.
- 167 Wachter, R. M., Elsliger, M. A., Kallio, K., Hanson, G. T., and Remington, S. J. (1998). Structural basis of spectral shifts in the yellow-emission variants of green fluorescent protein. *Structure* 6, 1267-1277.
- 168 Ward, W. W., and Bokman, S. H. (1982). Reversible denaturation of *Aequorea* green-fluorescent protein: physical separation and characterization of the renatured protein. *Biochemistry* 21, 4535-4540.
- 169 Weber-Ban, E. U., Reid, B. G., Miranker, A. D., and Horwich, A. L. (1999). Global unfolding of a substrate protein by the Hsp100 chaperone ClpA. *Nature* 401, 90-93.
- 170 Weber, W., Helms, V., McCammon, J. A., and Langhoff, P. W. (1999). Shedding light on the dark and weakly fluorescent states of green fluorescent proteins. *Proc Natl Acad Sci USA* 96, 6177-82.
- 171 Weiss, E., Lang, H. J., and Bernhardt, I. (2004). Inhibitors of the $K^+(Na^+)/H^+$ exchanger of human red blood cells. *Bioelectrochemistry* 62, 135-140.
- 172 Weiss, M., and Nilsson, T. (2004). In a mirror dimly: tracing the movements of molecules in living cells. *Trends Cell Biol* 14, 267-273.
- 173 White, J., and Stelzer, E. (1999). Photobleaching GFP reveals protein dynamics inside live cells. *Trends Cell Biol* 9, 61-65.

-
- 174 Widengren, J., and Schwille, P. (2000). Characterisation of photo induced isomerisation and back isomerisation of the cyanine dye Cy5 by fluorescence correlation spectroscopy. *J Phys Chem A* *104*, 6416-6428.
- 175 Widengren, J., Chmyrov, A., Eggeling, C., Lofdahl, P. A., and Seidel, C. A. (2007). Strategies to improve photostabilities in ultrasensitive fluorescence spectroscopy. *J Phys Chem A* *111*, 429-440.
- 176 Widengren, J., Dapprich, J., and Rigler, R. (1997). Fast interactions between Rh6G and dGTP in water studied by fluorescence correlation spectroscopy. *Chem Phys* *216*, 417-426
- 177 Widengren, J., Mets, U., and Rigler, R. (1995). Fluorescence correlation spectroscopy of triplet states in solution: a theoretical and experimental study. *J Phys Chem* *99*, 13368-13379.
- 178 Widengren, J., Kudryavtsev, V., Antonik, M., Berger, S., Gerken, M., and Seidel, C. A. (2006). Single-molecule detection and identification of multiple species by multiparameter fluorescence detection. *Anal Chem* *78*, 2039-2050.
- 179 Widengren, J., Rigler, R., and Mets, U. (1994). Triplet-state monitoring by fluorescence correlation spectroscopy. *J Fluoresc* *4*, 255-258.
- 180 Widengren, J., Terry, B., and Rigler, R. (1999). Protonation kinetics of GFP and FITC investigated by FCS- aspects of the use of fluorescent indicators for measuring pH. *Chem Phys* *249*, 259-271.
- 181 Wiehler, J., Jung, G., Seebacher, C., Zumbusch, A., and Steipe, B. (2003). Mutagenic stabilization of the photocycle intermediate of green fluorescent protein (GFP). *ChemBioChem* *11*, 1164 - 1171.
- 182 Wiley, J. S., and Cooper, R. A. (1975). Inhibition of cation cotransport by cholesterol enrichment of human red cell membranes. *Biochim Biophys Acta* *413*, 425-431.
- 183 Winkler, T., Kettling, U., Koltermann, A., and Eigen, M. (1999). Confocal fluorescence coincidence analysis: an approach to ultra high-throughput screening. *Proc Natl Acad Sci USA* *96*, 1375-1378.
- 184 Wiseman, P. W., and Petersen, N. O. (1999). Image correlation spectroscopy. II. Optimization for ultrasensitive detection of preexisting platelet-derived growth factor-beta receptor oligomers on intact cells. *Biophys J* *76*, 963-977.
- 185 Wiseman, P. W., Capani, F., Squier, J. A., and Martone, M. E. (2002). Counting dendritic spines in brain tissue slices by image correlation spectroscopy analysis. *J Microsc* *205*, 177-186.

- 186 Wohland, T., Friedrich, K., Hovius, R., and Vogel, H. (1999). Study of ligand-receptor interactions by fluorescence correlation spectroscopy with different fluorophores: evidence that the homopentameric 5-hydroxytryptamine type 3A_s receptor binds only one ligand. *Biochemistry* *38*, 8671-8681.
- 187 Wohland, T., Rigler, R., and Vogel, H. (2001). The standard deviation in fluorescence correlation spectroscopy. *Biophys J* *80*, 2987-2999.
- 188 Wong, F. H., Ng-Kamstra, J. S., Chen, N. L., and Fradin, C. (2007). Localized photodamage of the human erythrocyte membrane causes an invagination as a precursor of photohaemolysis. *J Microsc* *226*, 6-17.
- 189 Xie, X. S., Yu, J., and Yang, W. Y. (2006). Living cells as test tubes. *Science* *312*, 228-230.
- 190 Yang, F., Moss, L. G., and Phillips, G. N., Jr. (1996). The molecular structure of green fluorescent protein. *Nat Biotechnol* *14*, 1246-1251.
- 191 Yguerabide, J. Fast and accurate method for measuring photon flux in the range 2500-6000 Å. *Rev Sci Instr* *39*, 1048-1052.
- 192 Zamecnik, P. C., and Stephenson, M. L. (1978). Inhibition of Rous sarcoma virus replication and cell transformation by a specific oligodeoxynucleotide. *Proc Natl Acad Sci USA* *75*, 280-284.
- 193 Zhong, Z. H., Pramanik, A., Ekberg, K., Jansson, O. T., Jornvall, H., Wahren, J., and Rigler, R. (2001). Insulin binding monitored by fluorescence correlation spectroscopy. *Diabetologia* *44*, 1184-1188.

List of Figures

Figure 1.1: Simplified Jablonski diagram for the electronic state model of Rhodamine 6G with rate constants.....	9
Figure 1.2: Autocorrelation curve for Fluorescein at $\lambda_{exc} = 488$ nm.....	13
Figure 1.3: A schematic diagram of FCS setup.....	15
Figure 1.4: A schematic view of the observation volume.....	18
Figure 1.5: A schematic autocorrelation curve with various time scales of different process.....	20
Figure 1.6: Proposed biosynthetic mechanism for the formation of GFP.....	24
Figure 1.7: Ribbon diagram of the wt-GFP structure.....	26
Figure 2.1: Intensity dependent fluorescence correlation curves for EYFP.....	38
Figure 2.2: Normalised fluorescence excitation and emission spectra of GFP variants...	40
Figure 2.3: Normalised fluorescence excitation and emission spectra of YFP variants...	41
Figure 2.4: Intensity dependent τ_d of (3-F) Tyr-EGFP and (2-F) Tyr-EGFP with phenomenological fitting for the determination of $\tau_{d,0}$	41
Figure 2.5: Linear plot of τ_0 / τ_d (I) vs. intensity I of (3-F) Tyr-EGFP and (2-F) Tyr-EGFP.....	42
Figure 2.6: Photostability profile of investigated GFP and YFP variants.....	45
Figure 2.7: The bright fraction [B] of all the investigated mutants.....	45
Figure 2.8: Comparison of the different $\sigma_{bl}^{corr} / h\nu$ of EGFPs and EYFPs.....	46
Figure 2.9: Quantum yield of photobleaching Φ_{bl} of all the analyzed mutants.....	46
Figure 3.1: A) ribbon diagram showing relative comparison of Venus, EYFP and wt-GFP dimer orientations.....	50
B) Surface diagram showing differences in dimer interfaces of EYFP and Venus.....	50
Figure 3.2: Intensity dependent fluorescence correlation curves for SEYFP and EGFP..	54

Figure 3.3: Plot of excitation intensity verses contrast of all the investigated proteins EGFP, EYFP and SEYFP.....	54
Figure 3.4: Reduction in diffusion time upon excitation intensity of the investigated proteins EGFP, EYFP and SEYFP.....	55
Figure 3.5: Dependence of k_{23}^{eff} and k_{31} (SEYFP and EYFP) with excitation intensity...	56
Figure 3.6: Rates (k_{23}^{eff} , k_{31}) of EGFP verses excitation intensity.....	57
Figure 3.7: Plot of k_{31} of all the investigated GFP mutants verses I.....	58
Figure 3.8: A representation of the potential scheme for the interconversion between bright and dark state.....	59
Figure 3.9: Ball and stick diagram showing the effect of F64L (Venus) and V68L (EYFP and Venus) mutations.....	60
Figure 4.1: Schematic diagram of the interactions between the chromophore and the surrounding residues and water molecules in wt-GFP, S65T mutant and EYFP.....	65
Figure 4.2: Fluorescence excitation and emission spectra of investigated mutants T203YE222Q and EYFP.....	68
Figure 4.3: Normalized autocorrelation curves for EYFP at different wavelengths.....	69
Figure 4.4: Autocorrelation curves for T203YE222Q at different wavelengths.....	69
Figure 4.5: Saturating contrast observed by the mutant T203YE222Q.....	70
Figure 4.6: A plot of contrast verses excitation intensity (EYFP).....	71
Figure 4.7: Plot of rate constants k_{23}^{eff} and k_{31} verses intensity at 488 nm.....	72
Figure 4.8: σ_{forward} and σ_{backward} of EYFP is plotted against excitation spectrum.....	73
Figure 4.9: σ_{forward} and σ_{backward} of T203YE222Q mutant against excitation spectrum...	74
Figure 4.10: Proposed mechanism for light-induced decarboxylation of wt-GFP.....	75
Figure 5.1: Principal transport pathways for Na^+ and K^+ in the human RBC membrane.	78
Figure 5.2: Membrane potential profile across the RBC membrane.....	81
Figure 5.3: Focussing the laser beam on the cell membrane.....	82
Figure 5.4: A confocal image of RBCs labeled with BODIPY FL amiloride and R18 in	

HIS solution.....	85
Figure 5.5: Normalized fluorescence correlation curves taken with RBC membranes in different ionic strength solutions.....	86
Figure 5.6: Diffusion constants of BODIPY FL amiloride labeled $K^+(Na^+)/H^+$ exchanger in different solutions.....	88
Figure 5.7: Diffusion constants of β -BODIPY (R) FL-C12-HPC labeled lipids.....	89
Figure 6.1: Autocorrelation curve for FAM labeled oligonucleotide.....	95
Figure 6.2: Autocorrelation curve for FA-PLGA nanoparticles with fitting.....	96
Figure 6.3: Autocorrelation curve for PLGA nanoparticles with two component fit.....	97
Figure 6.4: Fluorescence lifetime measurements with Fluorescein and FAM labeled oligonucleotides.....	98

List of Tables

Table 2.1: Spectral data for EGFP, EYFP and their variants.....	42
Table 3.1: The obtained values of k_{31}^{therm} of different GFP mutants.....	58
Table 4.1: Contrast and dark fraction [D] of EYFP at different wavelengths.....	71

CURRICULUM VITAE
